

Radiation gradient assessment at the CERN CHARM irradiation facility: FLUKA simulations and experimental measurements

Melanie Krawina

April, 2018



Die approbierte Originalversion dieser Diplom-/
Masterarbeit ist in der Hauptbibliothek der Tech-
nischen Universität Wien aufgestellt und zugänglich.

<http://www.ub.tuwien.ac.at>



The approved original version of this diploma or
master thesis is available at the main library of the
Vienna University of Technology.

<http://www.ub.tuwien.ac.at/eng>



TECHNISCHE
UNIVERSITÄT
WIEN
Vienna | Austria

Diplomarbeit

Radiation gradient assessment at the CERN CHARM irradiation facility: FLUKA simulations and experimental measurements

ausgeführt am

CERN und Atominstitut
der Technischen Universität Wien

unter Anleitung von

Univ. Prof.i.R Dipl.-Ing. Dr. techn. Norbert Vana
Dr. Ing. Angelo Infantino (CERN)

durch

Melanie Krawina, BSc

Matr.-Nr. 1126047, 066 461

April, 2018

Melanie Krawina

Radiation gradient assessment at the CERN CHARM irradiation facility: FLUKA simulations and experimental measurements

Master Thesis, April, 2018

Reviewers: Univ.Prof.i.R. Dipl.-Ing. Dr.techn. Norbert Vana and Dr. Ing. Angelo Infantino

Vienna University of Technology

Institute of Atomic and Subatomic Physics

Vienna

European Organization for Nuclear Research - CERN

EN/STI-BMI Department

Geneva

Declaration

I declare that this thesis has been composed solely by myself and that it has not been submitted, in whole or in part, in any previous application for a degree. Except where stated otherwise by reference or acknowledgment, the work presented is entirely my own.

The data presented in this thesis was obtained in an experiment campaign carried out by the R2E group at CERN. I played a major role in the preparation and execution of the experiment, and the data analysis and interpretation are entirely by own work. Any contributions from colleagues in the collaboration, such as plots or calibrations, are explicitly referenced in the text.

Vienna and Geneva, April, 2018

Melanie Krawina

Acknowledgements

This work has been carried out as a collaboration between the Vienna University of Technology and the European Organization for Nuclear Research - CERN.

First of all, I want to thank Dr. Angelo Infantino for supporting and promoting this work and being a strong help during the whole process. Within this year, I could not only profit from his scientific expertise but always felt encouraged to go the extra mile to develop new skills. He provided me a unique awareness of critical scientific thinking and attention to detail. Without this motivation and his help, the thesis would have never been possible. I also want to thank Univ.Prof.i.R. Dipl.-Ing. Dr.techn. Norbert Vana for supporting this work in many aspects through his valuable input, his expertise in dosimetry and supervision. In addition, I want to thank Dr. Rubén García Alía and Dr. Markus Brugger from whom I've learned a lot this year, both from a scientific but also personal point of view.

Many thanks to all of my colleagues within the EN-STI BMI and EN-STI TCD section at CERN, that accompanied and supported me over this time. Namely, I want to thank Maris Tali, with whom I've not only found the best office mate and fellow Python enthusiast, but a dear friend. You're one of the strongest people I know. Cristina Bahamonde, someone who always listened and gave support, whenever needed. I look up to you. Romy Welschen, one of the most ambitious and motivated women I've met. You've always brightened my day. Tobias Polzin, for all those office visits and long conversations about life. Thanks for clearing my mind a lot. Francesc Salvat Pujol, for always reminding me to that humor is the most amazing quality someone can bring to the table. You're a true Viennese in my book. Additionally, I want to thank my peers and friends from the Vienna University of Technology. Thank you for joining me on this path.

Above all, I want to thank my family for being the strongest support in my private and professional life. Amanda, you've always been there and believed in me. My parents, with whom I would have never reached my goals and who encouraged and enabled my career and all of the other choices I've ever made.

Thank you.

List of Abbreviations

CERN – *European Organization for Nuclear Research* (originally *Conseil Européen pour la Recherche Nucléaire*), Geneva, Switzerland.

CHARM – *CERN High Accelerator Mixed field/facility* Irradiation facility, located at CERN, with the main purpose of testing electronic equipment in a radiation field similar to the one occurring at CERN accelerators.

COTS – *Commercial off-the-shelf* Components that can be bought off-the-shelf and do not need to be custom made.

DD – *Displacement Damage* Radiation induced damage: Incident particles displace atoms from lattice sites. It is roughly proportional to non-ionizing energy loss.

FLUKA – *Monte Carlo* particle transport and interaction code, named after *FLUktuerende KAskaden*, a legacy german acronym for “fluctuating cascade”.

FWHM – *Full Width at Half Maximum* The difference between the two extreme values of the independent variable at which the dependent variable is equal to half of its maximum value.

H-Factor – *hardness factor* Energy at which a specific share of the total HEH flux lies above

HEH – *High Energy Hadrons* hadrons (charged and neutral) with energies greater than 20 MeV

HEHeq – *High Energy Hadron equivalent* FLUKA quantity, describes the High Energy Hadron fluence, and additionally includes the contribution from the intermediate neutrons (0.2 - 20 MeV). The Weibull response of the Toshiba SRAM memories is taken into account

IRRAD – Proton irradiation facility, located at CERN.

LET – *Linear Energy Transfer* The amount of energy that an ionizing particle transfers to the material traversed per distance and measured in $\text{MeV cm}^{-2} \text{mg}^{-1}$

LHC – *Large Hadron Collider* A particle accelerator at the CERN complex and the largest single machine in the world.

N_{SEU} – *Number of Single Event Upsets* The count of Single Event Upsets

P-I-N diode – a diode with a wide, undoped intrinsic semiconductor region between a p-type semiconductor and an n-type semiconductor region. The p-type and n-type regions are typically heavily doped because they are used for ohmic contacts.

POT – *Protons On Target* CHARM quantity, measured by the SEC. The number of primary protons interacting with the CHARM target.

PS – *Proton Synchrotron* a particle accelerator at the CERN complex. Particles are accelerated up to 25 GeV.

R-Factor – Factor that defines the contribution from the thermal neutrons from the overall HEH fluence

R2E – *Radiation to Electronics* project at CERN, with the aim to mitigate the radiation induced errors in electronic devices

RadFET – RADFET dosimeters are a discrete p-channel MOSFET optimized for radiation sensitivity to detect the dose.

RadMON – *Radiation Monitoring System* Radiation detector system, that includes the RadFET dosimeter, SRAM memories to detect the HEH fluence and p-i-n diodes for the 1 MeV eq fluence.

RPL – *Radio-photo-luminescence dosimeter*. Passive dosimeter, made from Silver activated metaphosphate glass.

SC – *Super-Cycle* The beam extracted from the PS is divided into spills or pulses of ~ 400 ms, ordered in a so-called Super Cycle.

SEC – *Secondary Emission Chamber* A gas-filled secondary emission detector, used at CHARM to count the primary protons interacting with the target

SEE – *Single Event Effect* Category of radiation induced effects in materials. SEE are caused by the interaction of a highly-energetic single particle with the sensitive region of a component.

SEL – *Single Event Latchup* A potentially destructive triggering of a parasitic p-n-p-n thyristor structure in a device.

SEU – *Single Event Upset* A single bit-flip induced by a traversing particle or recoiling nucleus.

SRAM memory – *Static random-access memory* A semiconductor memory that uses bistable latching circuitry (flip-flop) to store each bit.

Thneq – *Thermal Neutron equivalent fluence* Neutron flux weighted by the $^{10}\text{B}(n,\alpha)^7\text{Li}$ cross section normalized to the value at thermal energy.

TID – *Total Ionizing Dose*. The cumulative damage of a lattice caused by ionizing radiation over the exposition time

1 MeV neq – *1 MeV neutron equivalent fluence* Radiation damage of various particles and energies are normalized to a 1 MeV neutron equivalent flux.

Contents

1	Introduction	1
2	Interaction between Radiation and Electronics	7
2.1	Introduction	7
2.2	Radiation induced defects in a mixed field	9
2.2.1	Total Ionizing Dose (TID)	10
2.2.2	Displacement Damage (DD)	11
2.2.3	Single Event Effects (SEE)	12
3	Detectors	17
3.1	Radio-photo-luminescence dosimeter (RPL)	17
3.2	RadMON	22
3.2.1	Overview	23
3.2.2	RadFET dosimeters	23
3.2.3	SRAM Memories	28
3.2.4	P-I-N diodes	30
4	CHARM facility	31
4.1	Facility description	31
4.1.1	Irradiation room	32
4.1.2	Radiation Field	34
4.2	Challenges	43
5	FLUKA	45
5.1	Introduction to FLUKA	45
5.2	FLUKA model of the CHARM facility	50
5.3	Challenges	54
6	Experimental Setup	57
6.1	Facility and test positions	57
6.1.1	Test setup	59
6.1.2	Test conditions	60
7	Results	61
7.1	Dose Gradient Assessment	62

7.1.1	Results T0	62
7.1.2	Results R11	66
7.1.3	Results R13	69
7.1.4	Results R1	70
7.1.5	Additional tests at the CERN ⁶⁰ Co calibration facility	76
7.2	HEH Fluence Gradient Assessment	81
7.2.1	Results R11	81
7.2.2	Results R13	85
7.2.3	Results R1	86
7.3	1 MeV Neutron Equivalent Fluence Assessment	92
7.3.1	R11	92
7.3.2	R13	93
7.3.3	R1	95
8	Conclusion and Outlook	101
	Bibliography	107
	List of Figures	111
	List of Tables	116
A	Appendix	121
A.1	CHARM irradiation room	121
A.2	CHARM radiation gradient assessment setup	122

Introduction

The European Organization for Nuclear Research, known as CERN¹ is the biggest research center for particle physics in the world, working with scientists from different countries to investigate and study the fundamental laws of this universe. CERN was established in 1954 and is based in Geneva, on the Franco-Swiss border, with buildings, facilities, and experiments in both countries. At the time of this thesis, CERN has 22 member states, resulting in $\sim 2,600$ scientific, technical, and administrative staff members, and additionally $\sim 12,000$ users, that contribute to this project (CERN, 2016). The CERN complex is based on six accelerators, various detectors and many experiments. A few of them can be seen in the Fig. 1.1.

The accelerator chain is formed by the LINAC, Booster, LEIR, PS, SPS and the Large Hadron Collider (LHC), which has a circumference of 27 km and is located 100m underground. Each machine in this chain increases the energy of the particle beams, before delivering them to various experiments, that have different research interests and goals in mind. The LHC itself is the most powerful particle collider, with the main research domain of high energy physics, more specifically the discovery and study of new particles and their properties. The most famous achievement so far is the discovery of the Higgs boson, as the missing piece of the Standard Model puzzle. Scientists from all over the world are working together at CERN in fields ranging from physics, electronics, mechanics, chemistry, medicine and software engineering, to study fundamental laws, solve challenges or create new inventions.

One project within those numerous examples, is the Radiation to Electronics (R2E) one at CERN, which is part of the Engineering Department, that studies and analyses the impact of radiation on electronic devices and systems. Radiation environments affect the operation of electronic components, that can reach from small disturbances to the total destruction of the equipment. However, the reliability of those systems for mid and long-term operation is crucial, therefore the goal is to reduce and minimize the drop-out quota of them. Radiation environments that are challenging for electronics reach from accelerator conditions, to ground and avionics applications, up to space equipment. Most of the time the radiation field present is composed of a variety of particles and energies, which makes the characterization and the prediction of the behavior of the systems in them even more complicated. To research the radiation-induced defects in electronics and to propose suitable mitigation solutions, the R2E

¹ derived from the name *Conseil Européen pour la Recherche Nucléaire*

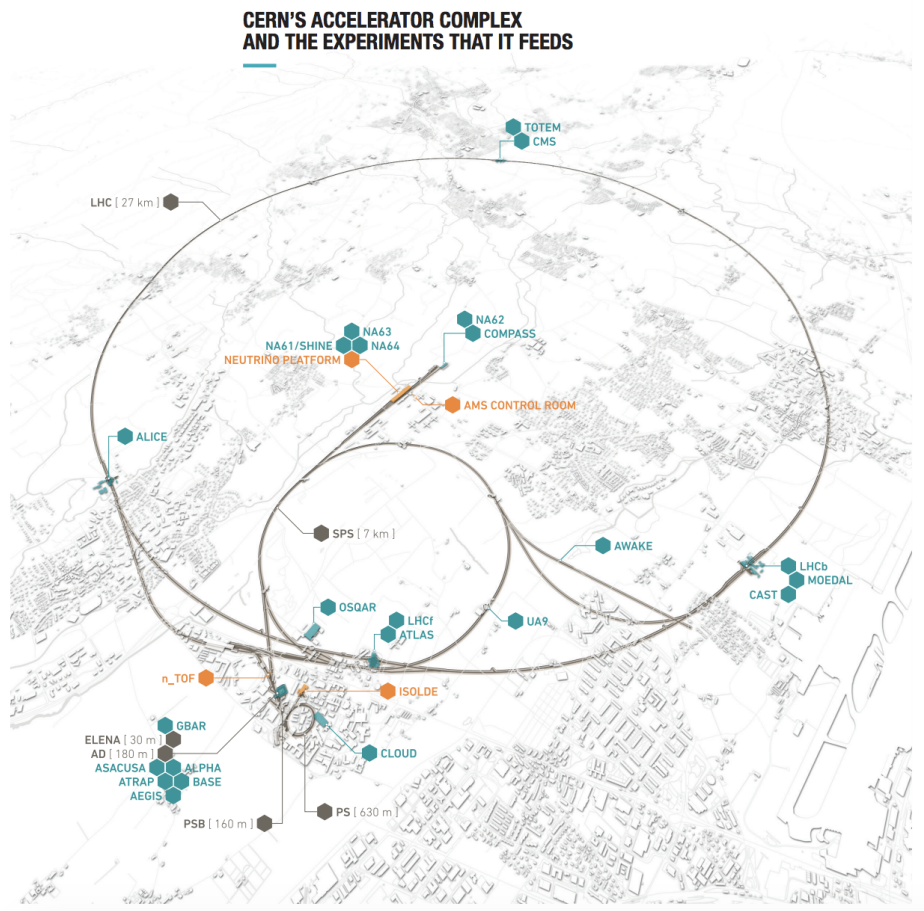


Fig. 1.1.: Overview of the CERN complex, including the the chain of the six accelerators, experiments and dimensions. The accelerators and beamlines are marked in grey, the detectors and experiments in blue. Orange symbolizes stand alone projects and facilities. (CERN, 2016).

project relies on experimental measurements with various detectors, that measure the quantities of interest, and simulation methods, that predict, estimate and calculate various quantities.

The importance of the R2E project and the achievements so far, can be excellently explained within the CERN context. The operation cycle of the LHC consists of a phase, where protons are injected in the vacuum pipes, the so-called file, then accelerated until reaching their maximum energy, up to 7 TeV, resulting in two beams, circulating in opposite directions, only crossing each other at the collision points, generating data for the experiments. This phase is the so-called "stable beam" and the duration of it is around 10 to 15 hours, if no interruptions happen. However, often the beam is prematurely terminated by a fault, yielding an average stable beam duration of ~ 6 hours García Alía, 2014. As soon as this happens, certain actions need to take place, before the beam is again injected and accelerated, which leads to big efforts both from time and manpower. A significant number of the premature beam dumps are related to radiation induced errors in the LHC electronic system, with 70 out of 409 beam dumps in 2012 attributed to those effects García Alía, 2014. The long term goal is

to prevent such effects and in conclusion the loss of beam time. Fig. 1.2 reports the number of beam dumps induced by Single Event Effects (a detailed description will be given in Chapter 2) over the LHC operation years, and an outlook for the operation of the High-Luminosity LHC, a possible prospect of the LHC. The beam dumps in this figure are reported per fb^{-1} ($1 \text{ fb} = 10^{-43} \text{ m}^2$), a quantity to describe the number of interactions between the particles, per unit surface, called the luminosity. The integral of the delivered luminosity over time is the integral luminosity. The performance of a particle collider can be expressed in terms of delivered integral luminosity.

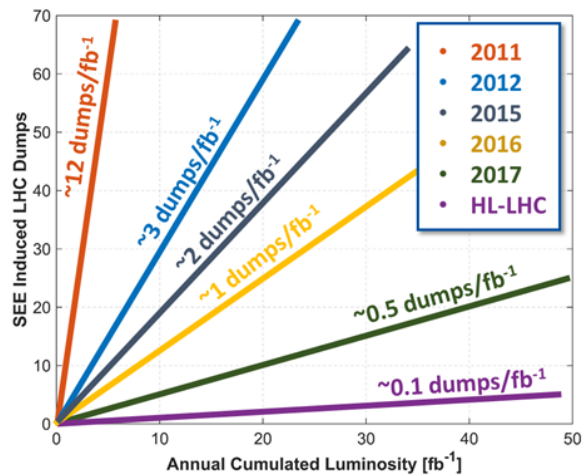


Fig. 1.2.: Beam dumps of the LHC, due to radiation induced failures in electronic devices and systems over the years. It can be seen, that those premature dumps are significantly reduced over the years, due to the efforts from the R2E group at CERN. Figure from internal R2E report.

Fig. 1.2 reports $\sim 12 \text{ dumps}/\text{fb}^{-1}$ attributed to radiation induced defects for the LHC in 2011. In the following operation year, this number already decreased to $\sim 3 \text{ dumps}/\text{fb}^{-1}$. Up until 2017 this number has decreased steadily, with currently only $\sim 0.5 \text{ dumps}/\text{fb}^{-1}$ attributed to radiation defects. The significant improvements in those numbers is due to the achievements of the R2E project at CERN.

With the help of relocation of devices, increasing the amount of shielding protection and the replacement with more robust systems, the numbers of failures were reduced effectively. However, those solutions are only partially feasible and are subjects to limitations, such as connection distances between accelerator and systems, space availability and costs. Long term solutions include preventions, in form of radiation tolerant systems, either in form of radiation hardened components or using commercial components and qualifying them against radiation. The first approach is sometimes not feasible due to an increase in costs, therefore the second one is the standard approach. The most important part is the testing of commercial components, to determine if they are suitable for the required application, and are able to perform within the radiation environment, where they will be implemented. This testing action can be defined as a process of taking measurements to check the quality, performance or reliability of something, before putting it into widespread use or practice. This means that the tests

have to be conducted in a way, that reproduces the practical application. For radiation tests, those tests have to mimic the main characteristics of the application in a much smaller time frame, and in a radiation field that is similar to the environment, they operate in (García Alía, 2014).

Therefore a specific facility, that is able to reproduce common radiation environments to test electronic systems, has been built in 2014 within the framework of the R2E project, at CERN. This new irradiation facility is called CHARM, and enables new options for testing equipment and analyzing the behavior of devices under test. The mixed radiation field present at CHARM is created by the interaction of a 24 GeV/c pulsed proton beam with cylindrical targets, consisting of different materials. With the help of different facility configurations (target material, shielding layers, positions within the irradiation room ...) the radiation environment and received field can be modulated, to mimic the desired conditions. This new facility, in combination with the knowledge gained from experimental and simulation campaigns, is a powerful tool for creating new radiation-tolerant solutions for the reliability of electronic systems, predicting failure rates and minimize flaws. Of major importance for test campaigns within CHARM, is the detailed knowledge of the radiation field present within the facility. As already pointed out before, to test equipment adequate, the practical application and its characteristics regarding the radiation environment have to be reproduced in the most detailed way. Therefore a correct understanding, characterization and calibration of the facility is one of the main goals within the first years of operation, due to the importance for the reliability and reproducibility of the tests performed within. In fact, the detailed knowledge of the radiation environment in specific test locations within the facility is mandatory to guarantee the goodness of the tests results, particularly for those applications, where an exact knowledge of the delivered dose or fluences is fundamental (e.g. electronic component lifetime, material science ...). The necessity of knowing the field quantities in a very precise way will be clear, if one looks at testing campaigns with equipment, that will be implemented in the CERN LHC environment or other applications, where it has to be guaranteed, that they will not be destroyed during their lifetime due to the environment they operate it. Reducing the radiation induced failures, increases the beam time and therefore more results for the physical experiments can be gained. All the devices that are part of the LHC work within severe conditions, and it has to be guaranteed that they survive those. Therefore the testing beforehand is mandatory and has to be done with huge precision. Uncertainties in the calibration within our test facility means, in equal ways, uncertainties in the outcome of the result. If the facility cannot guarantee specific levels of dose and fluence, for which the equipment should be calibrated, it may affect the performance of future machines and the electronic components severe. Additionally, the LHC environment is not the only one for which testing equipment is mandatory beforehand. If one looks at space applications, the necessity of guaranteeing the proper function within some levels is clear. The loss or the unavailability to perform experiments or devices, that have been sent to space, due to radiation induced failures

in electronic devices, leading back to an uncertainty within the testing campaign, have to be avoided at all cost. Therefore the conscientious and detailed calibration of the facility, the correct planning of the testing campaign and the crosschecks with different detectors and simulation, will guarantee performance increase and proper working equipment in the long run, whenever the devices are used in their real applications. This work requires a lot of resources but guarantees big improvements for the long run, and the certainty that one can trust the results that were gained during the testing campaign.

Previous campaigns, conducted with experiments and simulations, have already calibrated the radiation environment of CHARM in a general point of view. Those results can be found in Infantino, 2017; Thornton, 2016 and Mekki et al., 2016. It has been shown, that specific standard test positions within CHARM are affected by a strong radiation gradient, that needs to be evaluated in a qualitative and quantitative way. Due to the significant size of the test area within CHARM, the multiple facility configurations, the complex mixed field within, and the present radiation gradient at some positions, the dosimetry and calibration is challenging. This work will provide a first characterization of the radiation gradient, for the three quantities of interest within the R2E context (Total Ionizing Dose, High Energy Hadrons and 1 MeV neutron equivalent fluence), for four test positions within the irradiation facility. Experimental measurements were conducted with the RadMON system and additionally RPL dosimeter, and coupled with FLUKA Monte Carlo simulations.

This thesis reports the motivation and aim behind the CHARM facility, the ongoing benchmarking campaign to guarantee the reliability of experiments, and the results from the radiation gradient measurement campaign, that has been conducted in 2017, to understand the present radiation field and the consequences therefore better. Additionally, the necessity of knowing the radiation field and the consequences of a non or partially calibrated facility will be highlighted. An accurate knowledge of the radiation field is essential, to meet the strong quality standards that are needed for tests, to guarantee that equipment can endure the radiation environment, to which they are exposed. An uncertainty in the delivered dose or fluence within the testing facility, has fundamental consequences for the outcome of those calibration tests and can lead unforeseen equipment failure, that could have been prevented otherwise. A detailed study and benchmarking of the testing facility is therefore fundamental and necessary, to avoid deficiencies for long-term applications.

In detail, this thesis discusses the following.

- Chapter 2 will describe the basic principles and physical background of the interaction between radiation and electronics, with a focus on the three radiation-induced defects relevant for the R2E framework

- Chapter 3 will describe the detectors, that were used during the conducted radiation gradient campaign, measuring the quantities of interest
- Chapter 4 will describe the irradiation facility CHARM, its radiation field and the challenges within the benchmarking and calibration
- Chapter 5 will describe the Monte Carlo simulation code, that was used for the simulation part of this thesis
- Chapter 6 will describe the experimental setup for the radiation gradient campaign
- Chapter 7 will describe the results of the campaign and the consequences therefore

The unique radiation environment that is present at CHARM, characterized by various particles, from charged and neutral hadrons to electrons, positrons, and photons, ranging from thermal energies up to GeV, poses important challenges in the accurate calibration and dosimetry of the facility. The detailed look into the radiation gradient affecting the field at test positions within CHARM is the first of its kind but necessary to ensure the reliability and reproducibility of the tests, that are conducted within the facility.

Interaction between Radiation and Electronics

2.1 Introduction

Radiation-induced effects in electronic devices can pose serious threats to the reliability of the individual components or the total system. Especially COTS (Commercial Off The Shelf) items, which means not radiation hardened, are affected by radiation-induced failures that can lead to flaws, degradation, and destruction. Those defects can happen in every environment where radiation is present and the probability of error-rates is strongly dependent on the type of radiation, the energy deposition rate and the type of the used material.

The major radiation environments, where electronic components are used, are accelerator, ground, avionics and space ones. Particles passing through a material lose their energy through a variety of interactions and scattering mechanisms. In the framework of this thesis, the focus will be on the two major cumulative contributions of energy transfer from radiation to electronic materials, namely ionization and atomic displacement. Moreover, failure rates due to stochastic effects will be highlighted and taken into account as well.

The interest in radiation effects on atmospheric level applications (ground and avionics) has increased in recent years. Terrestrial ionizing radiation originates largely from particle showers of primary cosmic rays (protons, helium ions, and heavier ions) in the Earth's atmosphere. At sea level, the environment consists of a mixture of neutrons, protons, pions, muons and other particles. An increasing interest in the evaluation and simulation of galactic cosmic rays has developed, particularly regarding the radiation effects on airline crew and passengers, interplanetary missions and onboard electronics. More information can be found in Infantino et al., 2017b and Ziegler, 1996. The radiation effects that can occur can be categorized into so-called "soft fails" and "hard fails". Soft fails can be illustrated for example as spontaneous bit-flips or glitches, whereas hard fails usually lead to the replacement of whole components. The microelectronics industry has achieved tremendous progress over the last forty years with the evolution of product performances and, at the same time, a drastic reduction of the production cost per element. This happened due to the availability of constantly miniaturizing the elementary components of circuits, namely the MOS-FET (metal-oxide-semiconductor field effect transistor) devices. This scaling however

encountered physical and technological limitations due to gate oxide (SiO_2) leakage currents, a large increase of parasitic short channel effects and the mobility reduction due to highly doped silicon substrates. Additionally, due to those scaling effects, the sensitivity of integrated circuits to radiation from space or the terrestrial environment has evolved and at this point, natural radiation is inducing one of the highest failure rates of all reliability concerns for devices and circuits for nanoelectronics. The sensitivity is directly proportional to device dimensions and therefore a reduction of supply voltage and node capacitance, which results in a decrease of the critical charge (minimum amount of charge required to induce the flipping of the logic state, see section 2.2.3) and the sensitive area (the minimum collection area inside which a particle can deposit enough charge to induce the change). More information can be found in Autran and Munteanu, 2015.

For the accelerator point of view Brugger, 2012 states that especially control systems in the CERN LHC underground systems are vulnerable to radiation-induced damages and can lead to problems with beam operation. A specific project called the R2E (Radiation to Electronics) has been started with the goal to minimize the radiation-induced failures in the LHC and allowing beam operations with a "Mean-Time Between Failures" (MTBF) greater or equal than one week for a beam luminosity of $2 \cdot 10^{34} \text{ cm}^{-2} \text{ s}^{-1}$. As García Alía, 2014 states, in 2012 over 70 out of 409 beam dumps of the LHC accelerator were attributed to radiation-induced errors, with a total downtime of 300 hours. The goal is to reduce this number to zero and guarantee the availability of the machine, a stable beam and reducing beam dumps and average fault times. The mitigation measures in this context include relocating of commercial equipment, installation of additional shielding or the development of radiation tolerant hardware. Furthermore, space applications are prone to radiation-induced failures due to the nature of the environment they operate in. Trapped protons and electrons in the Earth's radiation belts and cosmic rays are challenging conditions for the operation of electronics. Radiation-induced defects can lead to sudden device and system failures, which reduces the lifetime of a space-based system significantly. Additionally, solar particle events have to take into consideration and may affect the reliability furthermore. Different approaches to minimize those errors have already been implemented or are still undergoing, for example, a suitable risk assessment of the radiation environment and uncertainties involved or the use of radiation hard design. More information can be found in Garcia Alia et al., 2017, Hoque et al., 2017 and Fleetwood et al., 2000. In different environments, many particles and physical mechanism contribute to serious degradation effects of the device operation, and a categorization is mandatory. The following chapter will introduce the main radiation effects occurring in a mixed field, the quantities of interest and their physical background.

2.2 Radiation induced defects in a mixed field

Many radiation environments are made of mixed particle types and energies, therefore referred as *mixed radiation fields* or *mixed fields*. The composition and characteristics of the field depend on the distance and angle of the source or interaction point, as well as (if present) shielding material or layers.

Electronic components exposed to such a mixed field will experience three different types of radiation-induced effects: displacement damages (**DD**), damages due to the Total Ionising Dose (**TID**), and Single Event Effects (**SEE**). The abbreviations DD, TID, and SEE will be used throughout this thesis to refer to the different groups of defects. The first two effects are of cumulative nature, meaning that due to the steady accumulation of defects as a result of penetrating particles, a measurable effect, that can ultimately lead to device failure, can be caused. SEE are stochastic defects, caused by direct or indirect ionization of a single particle, able to deposit sufficient energy through those processes in the material.

The TID effects are quantified through the physical property of the accumulated dose and non-ionizing DD through the accumulated 1-MeV neutron equivalent fluence. SEE and their probability to occur can be characterized as a function of accumulated High Energy Hadron HEH fluence, whereas we define high energy hadrons as the sum of hadrons above 20 MeV. Those three representative quantities for the major radiation-induced damages are important in the whole R2E context and are key features for qualification and quantification of measurements campaigns.

As García Alía, 2014 points out, there are several important differences between cumulative effects (DD and TID) and the stochastic one (SEE), which will be highlighted shortly.

- DD and TID damages are typically an issue for areas with significant high radiation levels, for example, the LHC tunnel environment, with levels above 10^{10} 1-MeV neutron equivalent fluence per $cm^{-2}y^{-1}$ and $1 Gy y^{-1}$. SEE on the other hand can also be a concern for areas with significantly lower levels.
- Cumulative errors in electronic components can be mitigated through a replacement and rotation protocol, whereas for SEEs this is not an option due to the stochastic nature.
- The failure risk of cumulative effects will not increase with an increased number of components, as long as the maximum dose and 1 MeV Neutron equivalent levels are below a certain limit. For SEEs, however, the Mean Time between failures will be inversely proportional to the total number of devices used.

- The TID sensitivity tends to decrease with the technology scaling owing to the smaller oxides and therefore lower trapped charge levels, whereas the SEE cross section typically increases with technology scaling. This behavior is due to reduced capacitances and voltages used in transistors in order to reduce the access speed and size of the pieces.
- TID and DD are proportional quantities that have relatively linear dependencies for values like a shift in the threshold voltage drift for RadFETs or for the forward voltage of p-i-n diodes ¹, whereas the correlation between the SEE rate and HEH fluxes is less straight-forward.

The properties and physical effects of the quantities itself will be explained in the following pages. Additionally, the used detectors for each quantity and their working principle will be described in Chapter 3.

2.2.1 Total Ionizing Dose (TID)

As already stated, the Total Ionizing Dose (TID) or dose is a cumulative effect based on the interaction of the incoming particle and the medium. To be more precise, the TID is related to the ionization caused by the radiation field particles and the generated charge in the oxides of electronic components due to them. The foundation of this is the Coulomb effect, which states that charged particles continuously interact with the electrons present in the medium, that they pass. The TID is described with the total dose (deposited energy per unit mass) and typically expressed in units of Gray (Gy, 1 Gy = 1 J/kg), which means the absorption of one Joule radiation energy within one kilogram of mater due to electronic interaction.²

$$D = \frac{dE}{dm} \quad (2.1)$$

The historical unit, and sometimes still used in the space environment, is *rad*. The two units are simply related by 1 Gy = 100 rad. Sometimes the definition of the dose rate is of interest as well, which is defined as average energy absorbed per unit mass and time, for example, Gy per second.

The dose is proportional to the Linear Energy Transfer (LET). The LET of a particle in a certain material is defined as its energy loss per unit length and density.

$$LET = \frac{1}{\rho} \cdot \frac{dE_{dep}}{dx} \quad (2.2)$$

¹The functionality, mode of operation and properties of the specific detectors for each quantity will be explained in detail in Chapter 3

²The electron interaction is important here since nuclear interaction can also lead to absorbed interaction, which is the case for the Displacement Damages

ρ is the density of the material and $\frac{dE_{dep}}{dx}$ the deposited energy per unit distance. Generally speaking, the LET decreases with an increase of the particle energy, with the exception of electrons. The LET is usually given in units of $MeV\ cm^{-2}\ mg^{-1}$. More information can be found in Dodd and Massengill, 2003.

For one particle, with the energy E , crossing through a semiconductor of thickness Δx and the area A , the conversion from the dose to the LET is

$$D_1 = \frac{E_1}{m} = \frac{E_1}{\rho \cdot V} = \frac{E_1}{\rho \cdot A \cdot \Delta x} = \frac{1}{A} \cdot LET \quad (2.3)$$

For N incoming particles, the total dose is the dose deposited by one particle, multiplied by the number of impinging particles which leads to

$$D_{tot} = \frac{N \cdot E_1}{A \cdot \rho \cdot \Delta x} = \Phi \cdot \frac{1}{\rho} \frac{E_1}{\Delta x} \quad (2.4)$$

Whereas Φ is the fluence of particles. In general, the flux ϕ is defined as the number of particles per unit surface and time, whereas the fluence Φ corresponds to a time-integrated flux. Therefore the dose is simply reduced to

$$D = \Phi \cdot LET \quad (2.5)$$

If one takes into consideration a source/beam, consisting of different types of particles, the calculation becomes more complex, due to the dependency of the LET from the particle type and energies.

$$D = \int LET(E) \cdot \frac{d\Phi(E)}{dE} \cdot dE \quad (2.6)$$

This equation shows the necessity to calculate the spectra of a mixed field to determine the total dose, for example with Monte Carlo simulation. From the experimental point of view, well benchmarked and calibrated detectors are used that work with electrical parameters that are strictly dependent on the cumulated dose. Two types of dosimeters were used within the framework of this thesis and will be introduced and explained in Chapter 3.

2.2.2 Displacement Damage (DD)

The second cumulative radiation damage mentioned is the displacement damage, a non-ionizing effect, based on the principle of the *Frenkel point defect*. This states that if a particle hits an atom, the later one is displaced from its initial lattice position, leading to a vacancy-interstitial couple. An important effect here is due to an (ionization) process the atom or ion is changing its size which leads to leaving its place in the lattice, and becoming an interstitial by lodging in a nearby location. This effect is

common in metals, semiconductors, and even insulators. As described in Leroy and Rancoita, 2011 due to Silicon substrate being the main component of most electronic devices, an incoming particle should transfer at least 21 eV to induce a Frenkel defect in the Silicon lattice.

The *intrinsic defects*, namely the vacancy and interstitial pair, are produced by particle collisions within the Silicon but are furthermore building-blocks for *extended defects*, expressly a varied range of features in crystals that include grain boundaries and interfaces. A graphical explanation of the Frenkel point defect can be seen in Fig. 2.1.

For collisions hard enough to allow large energy transfers, the recoiled atom can

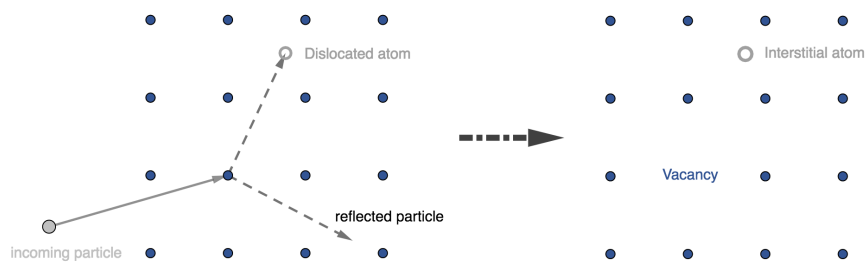


Fig. 2.1.: Graphical visualization of the displacement damage. An incoming particle hits a lattice atom, displacing it. The resulting vacancy and interstitial pair can lead to various degradation effects within the device. Graphics made by M.Krawina with the GeoGebra online tool. [GeoGebra Online Tool]

dislocate other lattice atoms, creating more vacancies and interstitial atoms, whereas regions of high-density vacancy-interstitial defects can form, called clusters or multi vacancies. For Silicon, this effect is already visible for primary energies of more than 1-2 keV.

As Holmes-Siedle and Adams, 2001 states, the motivation to study atomic displacement is both fundamental and practical. The control of the engineering properties of the material relies on a well-ordered crystalline lattice and therefore disturbances in it will degrade the performance of the material. Indeed, the establishment of vacancy-interstitial couples or the merge of former to so-called multi vacancies, act in the same way as dopants since they are a source of carriers in the semiconductor. Additionally, they can act as traps for carriers and increase the number of collisions by a moving charge. A fully detailed overview of different displacement damages can be found in Holmes-Siedle and Adams, 2001.

2.2.3 Single Event Effects (SEE)

As the name already indicates, SEE in microelectronics are caused by the interaction of an highly-energetic single particle with the sensitive regions of a component. Especially in the context of high-energy accelerator radiation fields, SEE are typically caused

by either HEH, intermediate neutrons (0.2 - 20 MeV) or thermal neutrons (energies around 0.025 eV). The standard monitored and calculated quantity to evaluate the SEE rates is the HEH equivalent fluence (the sum of all hadrons above 20 MeV and a weighted contribution of the intermediate energy neutrons). Additionally, the so-called R-factor is a figure of merit for the evaluation of the relative amount of thermal neutrons with respect to the total HEH fluence and is considered as well. A detailed explanation will be given in 4.1.2.

There are different types of SEE that can be classified in hard/destructive (D) and soft/non-destructive (ND) ones. Tab. 2.1 gives a brief overview of a few of them. The Single Event Upset (SEU) will be discussed in detail. (García Alía, 2014)

Tab. 2.1.: Different SEE phenomena that can happen in electronic components or systems. Modified table, original from Bonaldo, 2016.

	Name	SEE	Device	Description
ND	Single Event Upset	SEU	Memories	Reverse of a digital logic bit
ND	Multiple Bit Upset	MBU	Memories	Multi reverse of bits by one particle strike
ND	Single Event Transient	SET	Analog and mixed signal circuits	Voltage transient on a circuit node
ND	Single Event Disturb	SED	Memories	Short corruption of a stored bit
D	Single Event Burnout	SEB	Power MOS-FET	Burn of the MOSFET due to high current
D	Single Event Gate Rapture	SEGR	Power MOS-FET	Damage in the gate dielectric
D	Single Event Snapback	SES	MOSFET, SOI	High current due to activation of a parasitic BJT
D	Single Event Latchup	SEL	CMOS technologies	High current due to activation of parasitic transistors

Single Event Upset (SEU)

A single bit flip induced either by a traversing particle or by a recoiling nucleus emitted from a nuclear reaction is described as Single Event Upset (SEU). SEU are soft errors, which means they do not induce damage to the basic elements of electronic components and it is possible to rewrite them with the right value or triggering it back to its intended state.

To be more precise, an SEU is due to an individual event caused by a heavy ion or proton and the charge deposition resulting from the electron-hole pairs generated along the path of the incoming particle within the sensitive volume. This effect is called

direct ionization. Additionally SEU can also be caused by the interactions (elastic, inelastic scattering or spallation) of the incoming particle, for example, a neutron or ion, with atoms in the device, resulting in particles such as protons, deuterons or α -particles. Those recoil particles are heavier than their original ones with large ionization capabilities. They can create electron-hole pairs along their path as well, and the effects are called *indirect ionization*. (Leroy and Rancoita, 2011) Holmes-Siedle and Adams, 2001 describes that the ionization for both cases induces a current pulse in a p-n junction and the injected current may exceed the critical charge Q_c , the minimum electric charge that causes the change of state in a device. The importance of these effects is increasing due to the trend of smaller device geometries, that results in a decrease of the critical charge and consequently an increase in vulnerability to SEU. The vulnerability of a device to SEU is defined by two parameters:

- **Threshold LET** The minimum LET required to produce an upset and corresponds to a charge deposition comparable with the critical charge
- **Saturation cross-section** σ_{sat} All incident particles are capable of producing an upset, and no increase in the upset rate is seen for an increase of the LET.

By counting the number of SEU and knowing how many particles passed through a device, it is possible to calculate the probability of a given particle to cause an SEU. This probability is defined as the cross section σ and given with

$$\sigma(E) = \frac{N_{SEU}}{\Phi} \quad (2.7)$$

whereas N_{SEU} is the number of SEU and Φ the fluence of incoming particles. The unit is cm^{-2} .

In the R2E context, the majority of the SEU inducing particles are HEH. As Roed et al., 2012 points out, HEH do not carry sufficient stopping power to induce SEU directly through direct ionization, instead, SEU are induced through non-elastic interactions. At sufficiently high energies all hadrons are considered to be equally efficient in inducing SEU due to their similar nuclear interaction cross-section. The energy threshold for charged hadrons and non-elastic interactions is given by the Coulomb barrier, and below this threshold, no interaction will take place, consequently, also no SEU will be induced. Additionally, charged hadrons are limited by their short range at lower energies and for most devices hadrons below 20 MeV will either not make it through the package or they will reach the sensitive area of the devices with energies below the threshold one. Above 20 MeV, the cross section has already reached its maximum. Neutral hadrons, on the other hand, are not affected by the Coulomb barrier and therefore the threshold energy for them strongly depends on the material. For example, the energy required for producing an α particle within Silicon is about 2.7 MeV for the reaction $^{28}\text{Si}(n,\alpha)^{25}\text{Mg}$, whereas for Nitrogen (a potential dopant) this energy is

around 0.2 MeV, for the reaction $^{14}\text{N}(n,\alpha)^{11}\text{B}$. Since the SEU cross section is dependent on the energy, a weighting function has to be applied. For a comparison between FLUKA simulations and the measured SEU response of a device, the total fluence of HEH contributing to the SEU rate is given by

$$\Phi_{HEHeq} = \int_{E_{thres}}^{20MeV} \omega(E) \phi_n(E) dE + \int_{20MeV}^{\infty} \phi_{HEH}(E) dE \quad (2.8)$$

with $\omega(E)$ as the weighting function and E_{thres} the SEU threshold energy for neutrons. This quantity is called the High Energy Hadron equivalent (HEHeq) fluence.

Additionally, to HEH and intermediate neutrons, thermal neutrons can induce SEU through the $^{10}\text{B}(n,\alpha)^7\text{Li}$ capture reaction, for which the cross-section is inversely proportional to the velocity of the neutron. Through experiments, the total fluence of thermal neutrons contributing to the SEU rate is assumed to be

$$\Phi_{Th} = \int_0^{0.5eV} \phi_n(E) dE \quad (2.9)$$

As indicated, the cross-section depends on the energy of the particles and can be expressed as a function of the LET. Ideally, the σ -LET curve is a step function, where an SEU happens only when the incident particle has enough LET to generate charges that are higher than Q_c . Experimentally this curve increases with a finite slope from the threshold LET (LET_{th}) followed by reaching the saturated cross section σ_{sat} . This curve can be fitted with a Weibull curve, defined as

$$\sigma = \sigma_{sat} \cdot \left(1 - e^{-\left(\frac{LET - LET_{th}}{W}\right)^s} \right) \quad (2.10)$$

with W and s being fitting parameters. A typical example of the upset cross section curve can be found in Fig. 2.2.

To quantify the SEU one can define the error rate as

$$error\ rate = \frac{N_{events}}{device\ day} \quad (2.11)$$

but preferably the FIT (Failures-in-Time) rate is used, that describes the error rate or failure of a device per billion of working hours,

$$FIT = number\ of\ errors / (10^9\ hours\ device) \quad (2.12)$$

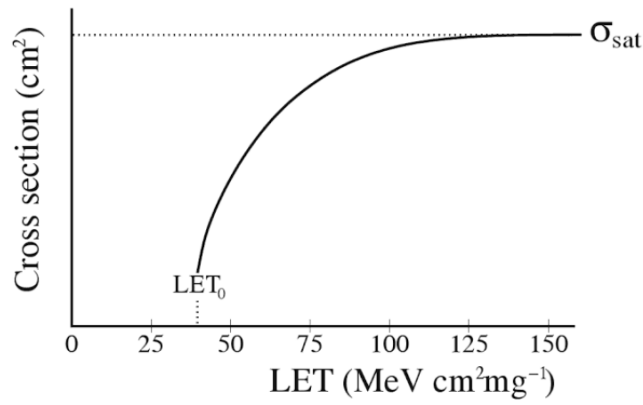


Fig. 2.2.: Example of a typical cross-section curve as a function of the LET. LET_0 is equal to LET_{th} and is defined as the threshold LET. σ_{sat} is the saturation cross-section. (Leroy and Rancoita, 2011)

As an example, a soft error rate of 1 FIT means that the mean time before an error occurs is a billion device hours.

More information can be found in Dodd and Massengill, 2003; Schwank et al., 2008 and Leroy and Rancoita, 2011

Detectors

As has already been explained in Chapter 2, the main quantities of interest within the R2E framework are Total Ionizing Dose, High Energy Hadron, and 1 MeV neutron equivalent fluence: To detect each quantity, a specific detector is used.

Only detectors that were used during the experimental campaign, that will be presented in Chapter 6, will be introduced and explained in this Chapter. The fundamentals of the detectors and baseline effects will be described, as well as their advantages and disadvantages.

A first approach is to differentiate between the RPL dosimeter and the RadMON system, that includes next to a RadFET dosimeter, also detectors for the HEH and 1 MeV neutron equivalent fluence.

3.1 Radio-photo-luminescence dosimeter (RPL)

Radio-photo-luminescence (RPL) dosimeters are passive dosimeters, made of silver-activated phosphate glass, that rely on the production of luminescence centers created by ionizing radiation. The amount of those centers correlate with the total absorbed dose.

Excited atoms of a substance return to their ground state by emitting photons - this process is called luminescence. The excited state can be caused by several reasons, for example, the exposure to photons, chemical reactions or rise in temperature. To differentiate the different kinds of excitations, usually, the cause is used as a prefix to the luminescence: photo-, chemi- or thermo-luminescence. For the RPL the prefix Radio-photo was chosen since the atoms get excited through ionizing radiation. After ultraviolet (UV) light excitation, of around 365nm, the atoms reach their ground state again and with the help of photomultipliers the emitted photons get detected, measured and correlated with the absorbed dose.

As Schulman et al., 1951 states, alterations of ultraviolet-excited luminescence of various compounds exposed to radiation have been described as far back as 1912. Starting around 1920 Przibram and students extensively studied this behavior in Vienna and even introduced the term "radio-photo-luminescence" to describe a material which is originally non-luminescent under visible or ultraviolet light, but after exposing to ionizing radiation.

The dosimeters are usually in form of small, transparent cylinders of a few millimeters length (6 - 8 mm) and around 1 mm in diameter.

Principle

Yamamoto et al., 2011 states that the most common material for RPL dosimeters is silver activated phosphate glass, where the concentration of silver has been chosen by trial and error methods, to reach a good result. The silver atoms are spread uniformly within the phosphate glass, in form of Ag^+ ions. Ionization processes create electrons e^- and holes h^+ within the glass, leading to a variety of reactions. The most common ones are



and



Both Ag^0 and Ag^{2+} are stable luminescence centers at room temperatures and return only to Ag^+ at annealing conditions, for example, a heating process with 400°C for one hour. A graphical interpretation of the formation of the excited silver atoms can be seen in Fig. 3.1.

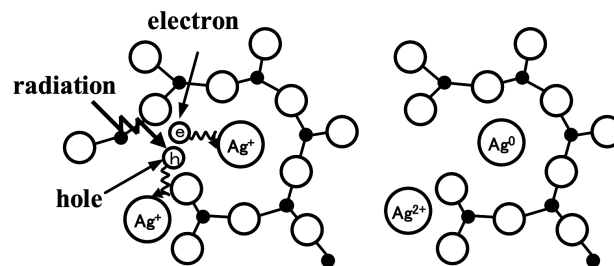


Fig. 3.1.: Graphical representation of the formation of luminescence centers. Due to ionization electron-hole pairs are getting created, that excite the Silver atoms within the the glass. Yamamoto et al., 2011

Electrons diffuse faster than the holes in the glass, therefore the accumulation speed of Ag^0 is higher than for Ag^{2+} . The creation of the luminescence centers is proportional to the absorbed radiation dose and therefore they can be used as dosimeters. At absorbed doses of >30 Gy, color centers are forming and the glass gets a yellow/brown color.

Composition

The majority of the used RPL dosimeters are silver-activated inorganic materials, due to the superiority of silver to other potential activators like cadmium and lanthanides. Studies have been ongoing for the modification and improvement of the metaphosphate glass base. Becker, 1973 states, that the main priorities for the glass base are the following:

- **Low predose** the background luminescence should be as low as possible. All luminescent ions, particularly Mn^{++} and Fe^{++} , have to be avoided.
- **High sensitivity** silver concentration and glass base have a strong influence on the sensitivity of the dosimeters. For instance by replacing $Ba(PO_3)$ and KPO_3 with $LiPO_3$ the sensitivity is increased by a factor of two. The silver content has a big influence as well and can lead to problems, as will be explained in the next subsection
- **Low energy dependence** A minimum energy dependency is desirable. Due to the silver content within the dosimeters, they are sensitive to low energy photons, due to the photo effect. As a result, an overestimation of the dose is happening for low energies.
- **Stability** Phosphate glasses are less stable against humidity and certain chemicals than conventional glasses and therefore the surface may become sticky
- **Fast build-up and slow fading** As will be described in the next subsection, the RPL have two unpleasant effects that may affect the result: a build-up and fading of the readout dose.

Based on the composition, some of those requirements and demands can be matched, others not. Tab. 3.1 gives an overview of a few common RPL dosimeters and their composition

Tab. 3.1.: Composition of some RPL dosimeters and their providers.

Name	Composition [wt%]						Reference
	Ag	Al	Li	P	O	Other	
Toshiba FD-1	3.7	4.6	3.7	33.4	53.7	0.9 B	Becker, 1973
Toshiba FD-5	0.52	6.1	-	33.1	51.3	8.9 Na	Becker, 1973
Toshiba FD-7	0.17	6.1	-	31.5	51.2	11.0 Na	Becker, 1973
Chiyoda TGC	0.72	6.2	-	31.5	48.3	13.3 Na	Nourreddine et al., 2015
Asahi Glass Company	0.17	6.1	-	31.55	51.2	11 Na	Hiramatsu et al., 2017

Side Effects

Schulman et al., 1951 explains that a characteristic behavior can be seen with the RPL dosimeters, shortly after irradiation: an increase in the readout intensity (build-up effect), which is later superimposed by a fading effect. Those two effects are dependent from temperature, the silver concentration in the glass, the glass base composition, and the LET of the radiation.

The build-up effect has been explained by Vogel and Becker, 1965 as following: Ionizing radiation lifts electrons in the conduction band, where they are either directly trapped by positively charged silver atoms through the reaction $Ag^+ + e^- \rightarrow Ag^0$, forming new luminescence centers, or they get trapped within shallow centers, which do not contribute to the radio-photo-luminescence. The electrons of latter reactions can thermally transfer to other Ag^0 atoms and contribute to the luminescence centers. This theory was based on the assumption that only the mentioned reaction from Ag^+ to Ag^0 contribute to those centers. Newer findings by Yokota and Imagawa, 1966 and Dmitryuk et al., 1996 assign this effect to other processes, namely $Ag^+ + h^+ \rightarrow Ag^{++}$ and $Ag^+ + Ag^0 \rightarrow Ag_2^+ + Ag^+ \rightarrow Ag_3^{++}$. Up to the time of this thesis a full explanation of the buildup is not available.

Fig.3.2 shows the RPL intensity as a function of storage time for different dosimeters, with the same constant glass base composition, but varying silver content. More details

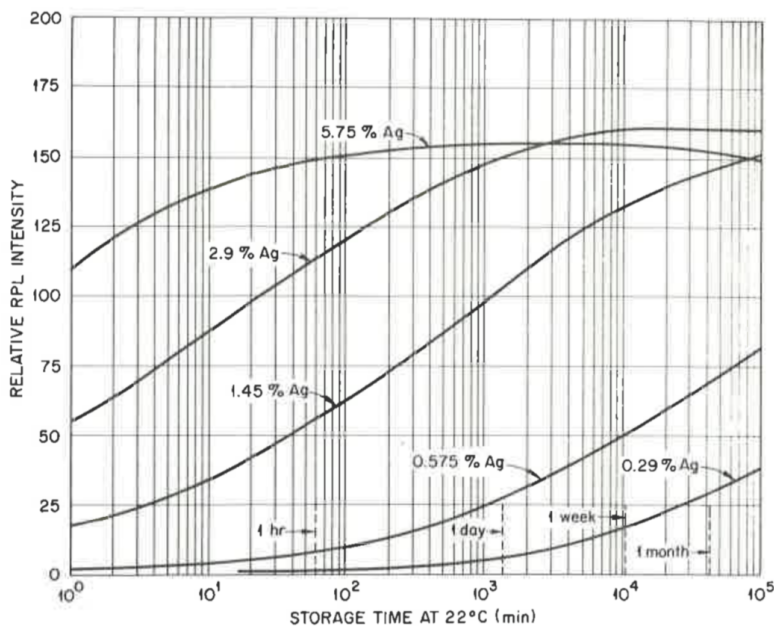


Fig. 3.2.: Comparison of the RPL readout intensity of different dosimeters, consisting of the same glass base but with varying silver content. The buildup effect is visible and increases with rising Silver content. (Becker, 1973)

on the build-up or fading effect can be found in Becker, 1973; Yokota and Imagawa, 1966 or Dmitryuk et al., 1996

Calibration

CERN used to work with the DOS2 type RPL dosimeters, manufactured by Schott in Germany. Past calibration campaigns and experiments to analyze the behavior of the dosimeters were obtained with this kind of glass. Due to a shortage of the dosimeters and the shutdown of the distribution firm, new RPL dosimeters were obtained after the Long Shutdown 1 of the LHC complex. Those new dosimeter were from the Chiyoda Techno Glass Corporation, Type FD-7 and they are used at CERN since 2014. Due to the new glass composition, all calibration campaigns have to be redone with the new glass. The reader is the Dose Ace (FGD-1000) one from the AGC TECHNO GLASS CO. company.

The new RPL dosimeters are calibrated as well in a pure ^{60}Co gamma-field. The response of them in this radiation field is a curve, as can be seen in Fig. 3.3. The available precision with such dosimeters is given with 5%, within the pure gamma-field, for a coverage of $1-\sigma$.

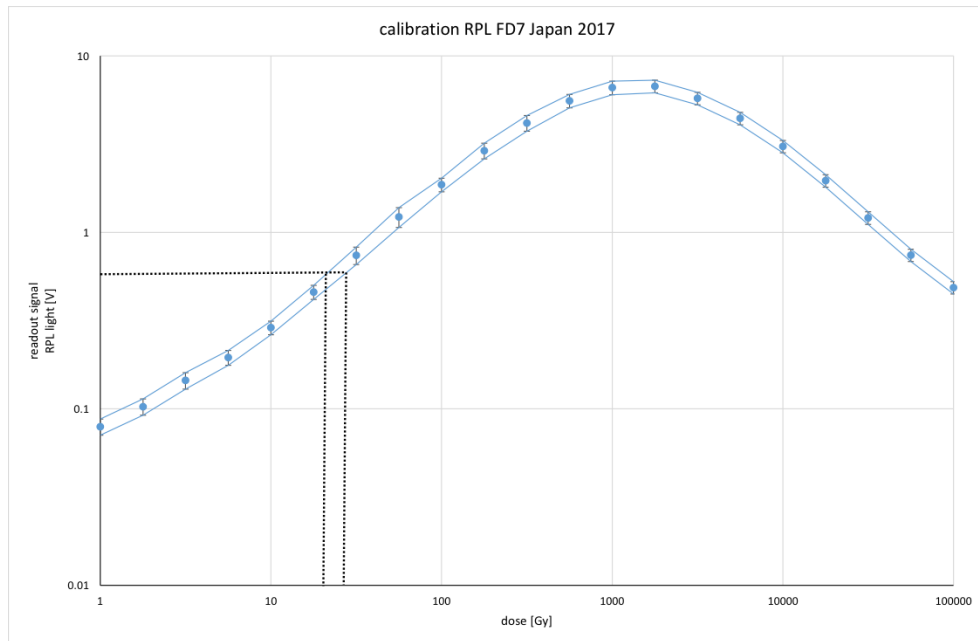


Fig. 3.3.: Readout function of the FD-7 RPL dosimeters calibrated in a ^{60}Co source. Each point is the average of 10 measurements. The errors are a combination of the standard deviation of the 10 measurements and the errors from the RISO irradiation. Total error values are multiplied by a factor of 5 for better visibility. Plot provided by the CERN HSE-RP group.

As Ravotti, 2017 points out, the light output increases almost linearly with the dose up to 100 Gy and then the curve reverses at about 1 kGy due to the increase of the coloration and self-absorption of the glass. This reversed behavior of the calibration curve makes the measurement uncertainties bigger for the kGy range. The dose range covered by RPL dosimeters currently used at CERN is between 1 Gy and 100 kGy

(CERN HSE-RP group, private communication), although one has to consider that these dosimeters overestimate the measured dose for low-energy gammas ($E < 500$ keV).

3.2 RadMON

A system to monitor the radiation levels at the Large Hadron Collider (LHC) at CERN was required, with the focus on all radiation effects important within the R2E context. Especially for this purpose, a system of various detectors called RadMON (RADiation MONitoring) was developed, that is able to detect the TID, HEH and 1 MeV neutron equivalent fluence. This system is placed in critical areas within the tunnel and the alcoves, where electronic equipment is or will be placed. A picture of the full RadMON can be seen in Fig. 3.4. The RadMON was designed specifically with only COT components, therefore a strict process of radiation hardness assurance was necessary. The detectors provide measurements of the TID by means of RadFETs, 1 MeV neutron equivalent fluence by means of p-i-n diodes and the HEH fluence by counting SEU of SRAM memories. According to Spiezia et al., 2014 the batches of p-i-n diodes have been irradiated at the CEA reactor (PROSPERO) up to an 1 MeV neutron fluence of $5 \cdot 10^{24} \text{ cm}^{-2}$. The SRAMs have been irradiated and calibrated with thermal neutrons of 5, 8 and 14 MeV and protons between 30 - 480 MeV to guarantee a full calibration and the working range.

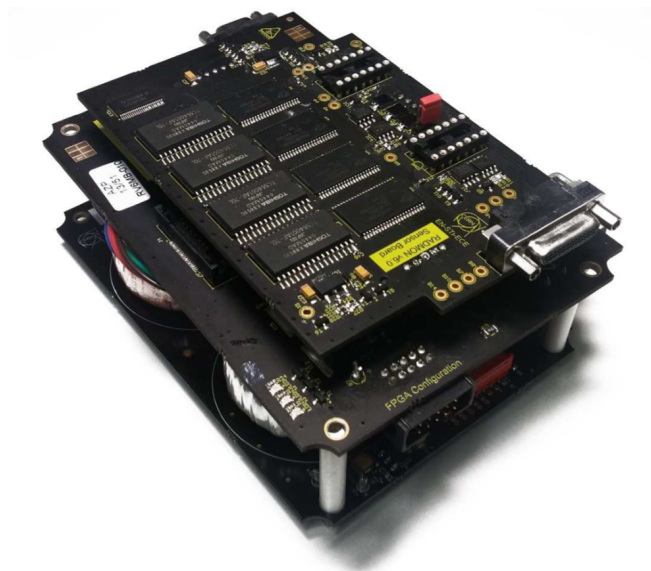


Fig. 3.4.: The fully assembled RadMON v6 system. Secondo, 2017

3.2.1 Overview

The RadMon device is built on four circuit boards for maintenance and flexibility purposes: a) the power board b) the main board c) the sensor board and d) the deported module.

The Powerboard includes, as the name already states, the main DC power supply whereas the MainBoard holds the control, monitoring and bus physical interface components and the Actel ProAsic3 FPGA (field-programmable gate array), an integrated circuit. The actual detectors and their reading circuits are attached to the sensor board. Furthermore, the sensor board can be connected via cable to the Deported Module, which then hosts the TID and DD sensors without any additional circuits required. This is an advantage when the sensors are placed in environments with high radiation levels, that can seriously affect the sensitive main or power boards. The functional structure of the RadMON can be seen in Fig. 3.5.

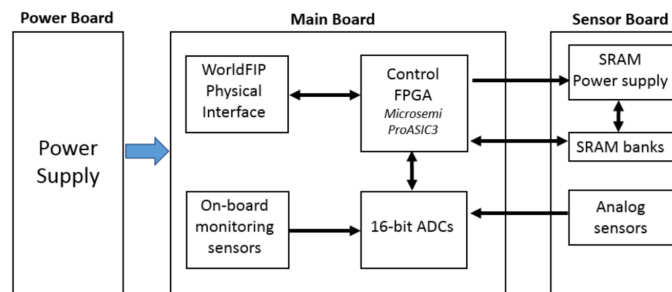


Fig. 3.5.: Functional structure of the RadMON V6. Secondo, 2017

3.2.2 RadFET dosimeters

The Radiation-Sensing Field-Effect Transistor (RadFET) is a small integrating radiation MOS (Metal Oxide Semiconductor) dosimeter that can be used as a stand-alone detector or it can be fully integrated into the RadMON system (See 3.2). Within the CERN context, the NMRC RadFET dosimeters are used, with an oxide thickness of 100 nm. (Spiezia et al., 2014) The advantage of the RadFET, compared to other silicon dosimeters, is that it is compact and can easily be connected to computers. The electrical output, a DC voltage, can be converted electronically and coupled with the accumulated dose. The voltage can furthermore be read remotely and displayed continuously. A benefit of using silicon as dosimeter material, in general, is that most of the electronic devices under test are made of the same material and therefore similar processes will take place in both devices.

RadFET dosimeters are based on the measurement of the threshold voltage, that is created by ionizing radiation penetrating the oxide. Due to ionization processes, charge is created and permanently trapped, causing a change in the threshold voltage, which

is, therefore, a function of the absorbed dose. If RadFETs are used as a stand-alone application, the threshold voltage is measured before and after the application. If they are used within the RadMON system the measurement is done during the operation. Furthermore, the new RadMON version v6 hosts two RadFET dosimeters for TID measurements.

In addition to the name "RadFET", the names "MOS dosimeters", "MosFET" or "Mosimeters" are used as well. A more in-depth look can be found in Holmes-Siedle and Adams, 1986; Holmes-Siedle and Adams, 2001, and Ravotti, 2017.

Principle

From MOSFETs (metal–oxide–semiconductor field-effect transistor) to bipolar ICs (integrated circuit or chip), oxides and insulators are key components of the majority of electronic devices. Ionizing radiation can induce significant charge buildup, leading to device degradation and failure. The ionization effect of interest is the creation of electron-hole pairs, where the net energy for SiO_2 to create such a pair, is relatively small with 18 eV. The energy of the incoming radiation is not crucial though since, compared to the DD, no momentum transfer is involved. Therefore ionization effects that may happen in space applications, by megavolt particles, may often be simulated by much lower energy particles.

Energetic particles can create electron-hole pairs due to these ionization effects. As long as the energies of the electrons and holes generated are higher than the minimum energy required to create such a pair, they can additionally create new pairs on their own. Therefore a single high-energy incident photon, electron or proton can create thousands of those pairs. The generated pairs in the oxide lead to almost all total ionization dose-related defects.

As Schwank et al., 2008 explains in detail, immediately after the creation of electron-hole pairs, most of the electrons will rapidly drift towards the gate, whereas the holes will drift toward the Si/SiO₂ interface. Nevertheless, some electrons will recombine with holes immediately and the fraction of electron-hole pairs, that escape this recombination process is called the electron-hole or charge-yield. Holes, that do not recombine, will transport through the oxide to the Si/SiO₂ interface, where some fraction will be trapped at defects, forming positive oxide-trap charge. Immediately after the formation, they will be neutralized by electrons, tunneling from the silicon or by the thermal emission of electrons from the valence band. As holes 'hop' through the oxide or are trapped close to the Si/SiO₂ interface, hydrogen ions (protons) are likely to be released. They can drift to the Si/SiO₂ interface themselves and form interface traps. Those interface-traps may take up thousands of seconds to saturate and normally do not anneal at room temperature, in contrast to oxide-trap charge.

To qualify these effects on a macroscopic level, trapped charges within the MOS

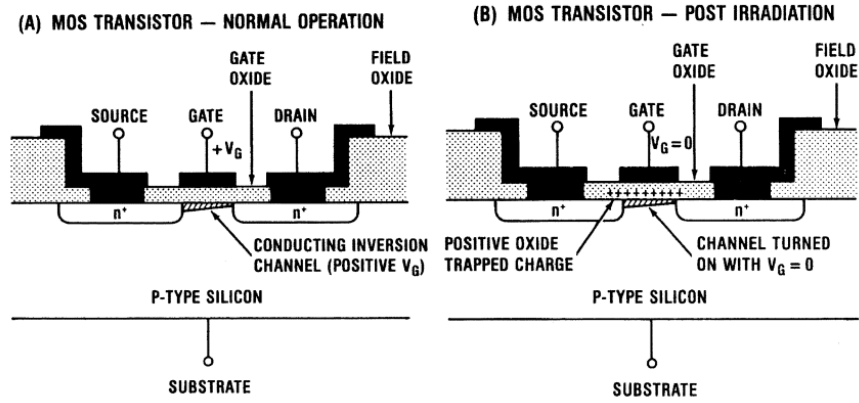


Fig. 3.6.: Schematic function of a n-channel MOSFET illustrating radiation-induced charging of the gate oxide: a) normal operation b) post-irradiation. Figure from Oldham and McLean, 2003

device leads to a shift of the threshold voltage.

Fig. 3.6 shows the basic radiation-induced problem within a MOS transistor. Fig. 3.6 a) shows the normal operation of the MOSFET, where the use of an appropriate gate voltage leads to a formation of a conducting channel between the source and drain and therefore a current flow. After irradiation, the radiation-induced trapped charge has built up in the gate oxide, causing a shift in the threshold voltage (which means a change in the voltage that must be applied to turn the device on). This effect is illustrated in Fig. 3.6 b). If this voltage shift is large enough, the device cannot be turned off, even at zero volts applied. Furthermore, the trapped charge is stored for a very long time, unless special measures are taken to erase it. This shift of the threshold voltage can be defined with

$$V_{th}(t) = V_{th}(0) + \Delta V_{th}(t) \quad (3.3)$$

whereas $V_{th}(0)$ is the threshold voltage before the irradiation and $\Delta V_{th}(t)$ is the voltage shift after the irradiation. $V_{th}(0)$, the initial threshold voltage, depends on the type of the MOS and working condition, such as substrate doping, oxide thickness, and temperature. $\Delta V_{th}(t)$ consists of contributions from oxide-charges and interface-charges.

The sensitivity of MOS devices to radiation-induced effects is used for dosimetric purposes, like it is done with the RadFET dosimeters. More details about Total Ionizing Dose Effects in MOS devices can be found in Oldham and McLean (2003) and Schwank et al. (2008) and Holmes-Siedle and Adams, 2001.

Side Effects

Long-term experiments have been conducted to investigate a possible fading effect for RadFET dosimeters. Holmes-Siedle and Adams, 1986 reports that RadFETs retain much of the radiation-induced charge in deeply-trapped sites. Therefore the threshold voltage shifts do not relax by large percentages over long storage times for those dosimeters. A value of $\sim 10\%$ for 8 years is reported. Spiezia et al., 2014 reports a fading effect for the RadFET with an oxide thickness of 10% after two months, and for RadFETs with an oxide thickness of 400 nm, this increases to 20% . Since the RadFETs are usually read in a much shorter time frame at CERN this fading effect is not considered in the presented data for this thesis.

The removal of the trapped charges restores the original threshold voltage and can be done either by heating the devices to a temperature of 300°C or illuminating the oxide with UV-light.

Furthermore, as all semiconductors, RadFET dosimeters responses are strongly dependent on their ambient temperature. Therefore a stabilization before each irradiation is highly recommended.

Calibration

The NMRC RadFETs with an oxide thickness of 100 nm were calibrated in different ^{60}Co facilities¹ to have a reference response curve for a gamma field, verify the spread among the sample, and evaluate the effects of the dose rate, temperature and gate bias. Since the dosimeters are mainly used in mixed fields, the aim was to get reference response curves for other particles as well, for example, protons², to see if the response changes based on radiation source. Those calibration experiments were done by the CERN EN-SMM-RME department and are reported in Spiezia et al., 2014 .

A good agreement between the 100 nm oxide RadFETs and other detectors, for example, ionization chambers as well as FLUKA results, were found. Fig. 3.2 shows the calibration curves of those RadFETs obtained at a ^{60}Co source at 25 and 40°C and with protons at 230 MeV at a dose rate of 50 Gy/h.

Each curve is the average of three samples, whereas the estimated standard deviation among the samples is 4% for $1-\sigma$ coverage. The RadFETs were tested at a gate biased at 0 V and 5 V. Additionally the tests were performed at different dose rates and annealing times as well. Fig. 3.2 shows that the sensitivity of the RadFET is significantly dependent on the gate bias, and only slightly by the temperature

¹Various calibrations have been conducted at the CERN ^{60}Co facility (activity of 10 TBq) and the ^{60}Co facilities at the Fraunhofer Institute in Germany (activity up to 10000 TBq)

²As proton facility the Paul Scherrer Institute (PSI) was used as source

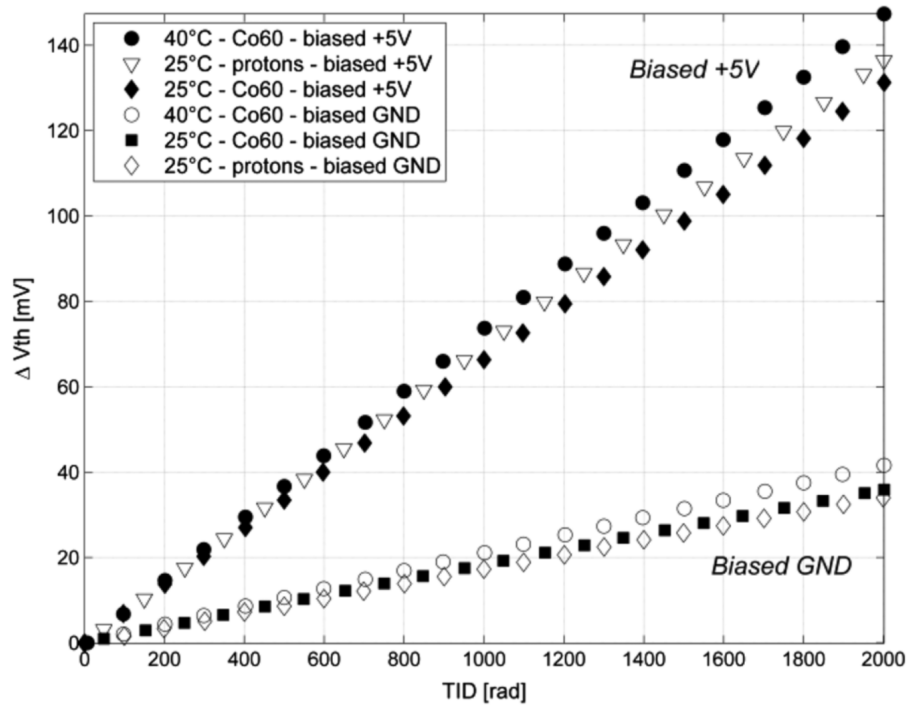


Fig. 3.7.: Average response curves for the 100 nm RadFET for a ^{60}Co and proton source at two gate voltages. (Spiezia et al., 2014)

variations from 25 °C to 40 ° C. Tab. 3.2 sums up the effect of these external effects on the RadFET response. In conclusion, this calibration campaign showed that the percentage difference among the tests at different temperatures and radiation sources is within 20 % for a coverage of $1-\sigma$ for both gate biases. The newest RadFETs have

Tab. 3.2.: Influence of external parameters on the response curve of the 100 nm RadFET. Data from Spiezia et al., 2014

Effect	RadFET 100 nm - 0 V	RadFET 100 nm - 5 V
Temperature		16 %
Dose Rate		5 %
Source		5 %
Fading (5d)	6 %	3 %
Fading (2m)	10 %	4 %
Bias sensitivity	0.02 mV/rad	0.07 mV/rad

been calibrated in three different ^{60}Co facilities up to 10 kGy and with protons at different energies (60 - 230 MeV) (Spiezia et al., 2014). The basic principles of this detector type have already been explained in 3.2.2. The major difference between the passive and integrated ones is, that for the latter the threshold voltages are measured by using a specific circuit within a specific measurement period. The threshold voltage for the passive RadFETs is calculated with one measurement before and one after the irradiation. The new RadMON version hosts two RadFETs for TID measurements.

3.2.3 SRAM Memories

The current RadMON version (v6) additionally hosts two SRAM banks: a 4 x 4 - Mbit Toshiba SRAM TC554001AF7L and 4 x 8 - Mbit Cypress SRAM CY62157EV30. It is possible to control the voltage supply remotely through the field bus and set it to 1.8 V, 2.5 V, 3 V, 3.3 V and 5 V. For the SEU detection algorithm a known pattern is written in the memory area and then continuously compared by the controller with the original one. If a bit error is detected the error counters are updated and the faulty address is written back to the correct pattern.

The previous RadMON version v5 employed a 4 x 4 - Mbit Toshiba SRAM memory bank only. The number of induced SEU is proportional to the incoming fluence of particles at a given energy. The relationship between the number of SEU and the HEH and thermal neutron fluence is given with the following equation, as reported by Kramer et al., 2011,

$$N_{SEU}(V) = \Phi_{HEH} \cdot \sigma_{HEH}(V) + \Phi_{Th} \cdot \sigma_{Th}(V) \quad (3.4)$$

whereas the σ are the cross sections as a function of voltage for HEH and thermal neutrons respectively. By determining those cross sections for the SRAM memories, for the specific particles, and for two different voltages, this equation is solvable. However, it needs two consecutive measurements operating the same RadMON at two voltages. Therefore the newer RadMON version uses an additional SRAM bank, populated with 4 x 8 Mbit Cypress SRAM memories, which has the advantage of being latch-up free, having a larger size and higher HEH-fluence cross section and not being sensitive to thermal neutrons (the cross section for them is two orders of magnitude lower than for the HEH one). The new RadMON design is able to either use one bank or the combination of both of them. This makes it possible to retrieve the HEH and thermal fluence with one single measurement.

The calibration was conducted by the CERN EN-SMM-RME department and is reported in Spiezia et al., 2014: both SRAM memories have been qualified with protons in the 30 - 230 MeV range as well as with thermal neutrons. The uncertainty for using a proton response, in comparison to a real HEH source, that also includes pions, will be smaller than other uncertainty sources, like the simulation of the radiation field, the exact location of the component or the part to part sensitivity spread. The cross-section of both SRAM memories for thermal neutrons and protons were measured with various chips from the same lot, and the average values for the cross sections are reported in Tab. 3.3.

The aim of improving the accuracy in a mixed field, the SRAM memories were also calibrated with neutrons at energies of 14, 8 and 5 MeV, and with 480 MeV protons at the TRIUMP facility, to evaluate the cross sections.

Tab. 3.3.: SEU cross section for thermal neutrons and 230 MeV protons for two SRAM memories. Data reported in Kramer et al., 2011; Spiezia et al., 2014

Source	SEU cross section (\pm Error) [cm^2/bit]	
	Thermal neutrons	Protons 230 MeV
Toshiba TC554001AF-70L 5V	3.1E-15 (0.3)	3E-14 (0.3)
Cypress SRAM CY62157EV30	4.4E-16 (2.2)	3.8E-14 (0.15)

More information regarding the SRAM memories and the calibration campaigns with them, can be found in Spiezia et al., 2014 and Kramer et al., 2011.

3.2.4 P-I-N diodes

A series of three P-I-N silicon diodes are used to quantify the Displacement Damage. More specifically the series of three P-I-N diodes BP134FS from SIEMENS are used in the current RadMON system.

Ravotti et al., 2007 describes the P-I-N diodes as junction devices with a base of high-resistivity n-type silicon. Irradiation produces displacement damages in the silicon base that results in an increase of the diode's forward voltage. The reading current injects a constant current to measure this forward voltage and it is proportional to the particle fluence. The shift in the forward voltage ΔV_F can be expressed by following equation

$$\Delta V_F = c \cdot k \cdot \Phi = c \cdot \Phi_{eq} \quad (3.5)$$

whereas k is the hardness factor, allowing to compare the damage efficiency in silicon of different radiation sources. The general interest is the expected damage for devices due to various particles, energies, and doses, therefore it is common in the R2E context to normalize everything to a 1MeV equivalent neutron fluence, here given by Φ_{eq} , which would result in the deposition of the same nonionizing energy causing equivalent damage. Φ is the total particle fluence and c is an experimental parameter. In reality, the series of the three P-I-N diodes are pre-irradiated at a 1 MeV neutron equivalent fluence of $4E+12$ neutrons cm^{-2} , to bring the sensors to a working point, where a sensitivity of $2.5E-10$ mV $n^{-1} cm^{-2}$ is assured. The diodes are used to have a higher resolution up to $10^{12} cm^{-2}$ and the new RadMON can host additionally an LBSD diode, that can assure a better resolution at low fluence ranges. Moreover, it is possible to use one SIEMENS p-i-n diode for the measurement of high neutron fluences up to $10^{14} cm^{-2}$, with the help of the deported module.

More information can be found in International, 2014 and Spiezia et al., 2014.

CHARM facility

The irradiation facility called CHARM (CERN High Energy Accelerator Mixed Field/Facility) has been built at CERN in the framework of the Radiation to Electronics (R2E) project between 2013 and 2014. The main purpose is to test and qualify electronic devices and systems operating in complex mixed radiation fields, consisting of charged and neutral particles with different kinds of energies, from GeVs to thermal ones, in a radiation environment similar to some representative radiation fields. Those radiation fields include accelerator, ground, atmospheric and space ones.

Before CHARM, electronic components used to be tested in mono-energetic particle beams/sources with only one or few discrete energies, or in particle fields, consisting of a single particle with a broad energy spectrum. The advantage of this new facility is that equipment can be tested in more realistic scenarios, considering those devices are usually subjected to more complex environments, consisting of multitudes of types and energies. The radiation field inside the facility can be modulated and adjusted in various ways to approach the radiation environment needed for the equipment. If one takes additionally the dimensions of the irradiation room into account, the facility is unique in its kind and will be introduced in detail in the following chapter. A full overview of the facility and all its aspects can be found in Thornton, 2016; Mekki et al., 2016 and Bonaldo, 2016.

4.1 Facility description

CHARM is situated in the East Area hall on the Swiss Site of CERN, Meyrin. It receives a 24 GeV/c proton beam from the Proton Synchrotron (PS) accelerator through the beam line T8. The beam and the building are shared with another CERN facility, namely IRRAD, which is located upstream of CHARM. Due to that, IRRAD activities have an impact on the primary proton beam that CHARM receives. The layout of the building that hosts both facilities can be seen in Fig. 4.1

CHARM itself consists of an irradiation area, which is a controlled access area and divided into different zones, and a technical area, shielded by meters of concrete, marble, and iron, to guarantee that users and staff can access and prepare experiments freely.

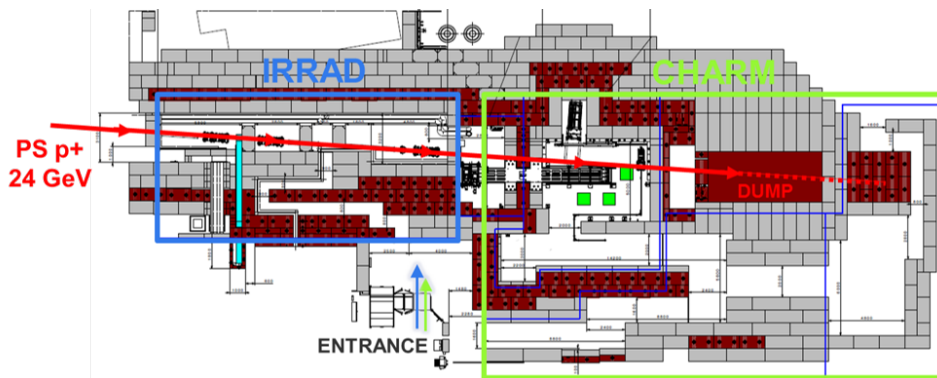


Fig. 4.1.: Facility layout of the building 157. The East Area receives a 24 GeV/c proton beam from the PS accelerator, which travels through the IRRAD facility first, before reaching CHARM (Bonaldo, 2016).

As Bonaldo, 2016 points out, the irradiation area is divided between the actual irradiation room, the patch panel area, and a preparation zone. The latter one is a heavily shielded zone, used to store, prepare and mount/unmount equipment that was irradiated in the irradiation room. The patch panel area is close to the entrance of the irradiation room, where users can connect their equipment to instruments, that are located in another technical room, within the technical area. The technical area is located on a higher floor and locates monitoring devices, space to prepare equipment or do other related work. More details about those areas and a more in-depth of look of the facility as a whole can be found in Bonaldo, 2016 and Thornton, 2016.

4.1.1 Irradiation room

Within the irradiation room, which is approximately 70 m^3 , the secondary mixed field is created by the interaction of the primary proton beam with a cylindrical target of 50 cm length and 8 cm diameter. To change the target material, a so-called target-revolver was implemented, containing actually three different targets consisting of different materials: copper, aluminium or aluminium with holes. The latter one is made from aluminium disks with cuts made through the center, to reduce the density by a factor of 2, whereas the first two ones are from solid metal. By choosing the target material the mixed field can be modulated regarding the field intensity, whereas the copper target results in the highest doses and particle fluences. Due to the movable target revolver, it is furthermore possible to run the facility without the target and test in the 24 GeV proton field.

Additionally, four layers of shielding are installed in the middle of the irradiation room, that can be fully inserted or removed, to modulate the generated mixed field even further. The outer two layers are 20 cm thick concrete slabs, whereas the inner ones are made from 20 cm iron. It is possible to choose a full shielding configuration (CIIC),

a semi-shielding one (CIOO) or a fully open one (OOOO). As a result of the shielding the energy, the flux and the dose rate of the field is reduced for affected test positions and even the particle compositions can be modified. To report the configuration in a short way, the abbreviations cp_OOOO, cp_CIOO and cp_OOOO are used. "cp" indicates the copper target, the following four letters the shielding layers, whereas "O" signalizes open, "C" stands for concrete and "I" for iron. Analogue abbreviations for the aluminium ("al") and aluminium with holes ("alh") target are used.

The irradiation room hosts a number test positions that are updated consistently. At the time of this thesis, there are 13 standard test positions in forms of a rack, 9 tests positions in terms of a Montrac rail transportation system, a high dose rate test table close to the target and two additional ones outside of the irradiation room. Those positions are distributed throughout the room and represent different radiation environments, due to being situated directly in the beam, behind layers of shielding or at various angles and distances from the target. The ones close to the beam are dominated by charged hadrons with energies extending up to GeV range, whereas the field is dominated by neutrons for the positions perpendicular to the beam.

All the test positions, the shielding, and the target can be seen in the Fig. 4.2, which represents the irradiation room.

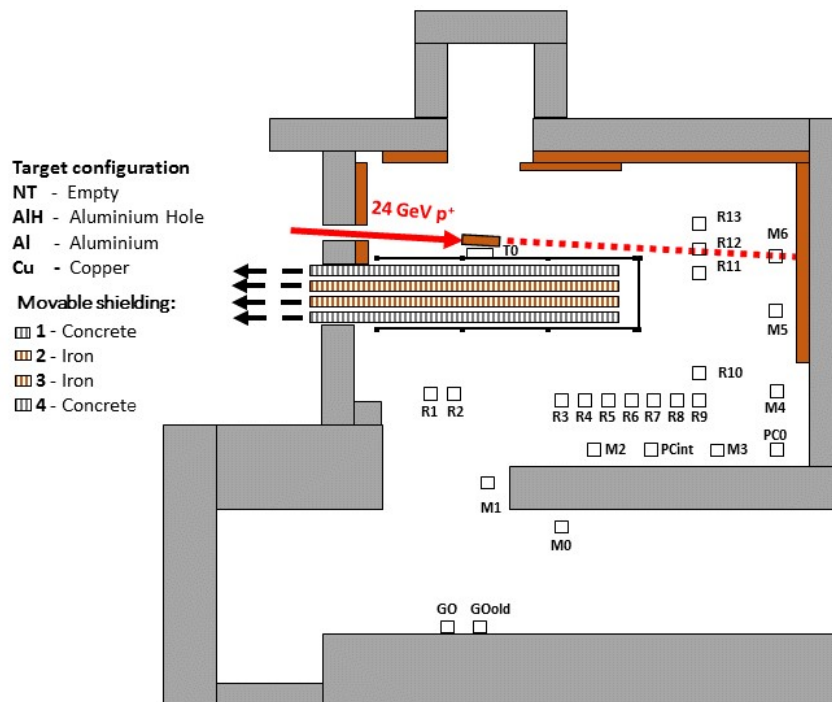


Fig. 4.2.: FLUKA CHARM model that shows the layout of the irradiation room. The target, the shielding, and the most used test positions can be seen.

The beam extracted from the PS can be altered in a few ways regarding beam intensity, spill size and frequency. As Gatignon et al., 2013 and Gatignon et al., 2015 state, the PS beam is, opposite to constant beams, divided into spills or pulses of ~ 400 ms,

ordered in a so-called Super Cycle (SC). A Super Cycle length lasts around 45 seconds, with around 40 spills.

For the beam that CHARM receives, the intensity usually varies from $1E11$ to $5E11$ POT per spill and the spill count goes up to 6 spills per super-cycle, whereas 3 spills are used on average. The number of primary protons interacting with the target (Protons On Target - POT) is an important quantity in CHARM terms and is measured by the secondary emission chamber SEC1 placed upstream the IRRAD facility.

4.1.2 Radiation Field

Due to the many facility configurations, there is a variety of particles with different energies present at the various test locations. To better understand the radiation field and benchmark all the different test configurations, FLUKA Monte Carlo code is used. As will be described in Chapter 5 a detailed model of the facility has been built, including a correct description of the beam and good assumptions of the running parameters and thresholds. An overview of the most important quantities to characterize a radiation field, a description of the field present at CHARM, as well as a comparison with other radiation environments, will be given in this section.

Describing Quantities

The mixed field present at CHARM consists of protons, neutrons, kaons, pions, muons, electrons, positrons and photons, from GeV down to thermal energies, which are resulting products from the interaction of the primary proton beam with the target. To qualify and compare different mixed fields to each other many describing quantities can be considered. The most common ones for the day to day use within the CHARM context will be presented here.

One of the most basic but important parameters is the number of protons on the target, **POT**. The intensity of the mixed field is directly proportional to this quantity and on average CHARM receives $3.3E10$ POT per second, for 3 spills per Super Cycle and $5E11$ protons per spill.

Various types of particles and energies will have a different impact and influence on the operation of electronics and their systems. One key factor for SEE (as explained in 2.2.3), is the particle energy and how the energy is transferred to the sensitive part of the device. To quantify this, the "linear energy transfer" (LET) and its minimum limit to induce SEE is used. The most common particles that cause such reactions, which produce particles with large enough LETs to induce SEE, are hadrons and therefore they are of special interest in the R2E work. A special term for those hadrons with

energies high enough, we use 20 MeV as a lower limit, is "high energy hadrons" (**HEH**). This limit of 20 MeV was chosen since it corresponds to a rough minimum to cause SEEs. Another quantity that is used in the FLUKA context is the High Energy Hadron equivalent **HEHeq** one, which takes the properties of the detector, that measures the HEH fluence, into consideration. Generally speaking the sensitivity for intermediate neutrons is included. A more detailed description of the difference between those two values was already given in the section 3.2.

Thermal neutrons can cause problems for electronics as well due to ionization of products of nuclear capture reactions within the sensitive area. Therefore the knowledge of the thermal neutron fluence is essential for some application and devices. Equivalent to the HEHeq fluence, there is another quantity within FLUKA for the thermal neutron equivalent fluence (Φ_{ThN}) that is regularly used by taking the thermal neutron fluence and folding it with a $1/v$ weighting to duplicate the capture the cross-section of neutrons in borons, due to the high appearance of boron in older electronic components. The products from the nuclear reaction of neutron induced ^{10}B fission can have large enough LETs to induce SEEs.

The ratio of the thermal neutrons to the HEH is called the **R-Factor** and is used to define the contribution of thermal neutrons from the overall HEH fluence.

$$R = \frac{\Phi_{ThN}}{\Phi_{HEH}} \quad (4.1)$$

Within CHARM, a higher R-factor is reached with an increasing angle of scattering, so the lateral positions reach a maximum. The factor can rise further with an inserted shielding. Infantino, 2017 reports an R factor of ~ 4 for the test position R1, without shielding, and up to ~ 28 with the full shielding inserted, for the copper target.

Another parameter to represent the radiation field is the so-called "hardness factor" or more general the hardness of the field. The hardness factors are in fact energies, at which a specific share of the total HEH flux lies above. A strong energy dependence of the cross-section can have a potential impact on the operational error rate of devices. The most used factors are $H_{1\%}$, $H_{10\%}$ and $H_{50\%}$, which define the energies at which one can find 1%, 10% or 50% of the total high energy hadrons above. Equation 4.2 shows the calculation of these factors in a general way.

$$H(E) = \frac{\int_E^\infty \frac{d\Phi(E)}{dE} dE}{\int_0^\infty \frac{d\Phi(E)}{dE} dE} \quad (4.2)$$

$H(E)$ is a factor between 0 and 1, whereas E is the energy and Φ the fluence. A particularly interesting case is $H(E) = 0.5$, where E represents the energy above 50% of the particles can be found. This equation would result in

$$0.5 = \frac{\int_E^\infty \frac{d\Phi(E)}{dE} dE}{\int_0^\infty \frac{d\Phi(E)}{dE} dE} \quad (4.3)$$

Moreover, the normalized reverse integral of the HEH flux as a function of energy can be used to provide a graphical representation of the hardness of a certain spectrum and compare different environments regarding their energy dependency. The knowledge of the hardness factors depends on the knowledge of the particle spectra and within CHARM we reach the highest ones close to the beam.

The R - factor and the H - factors are the most important quantities to compare the field of CHARM with actual radiation environments, where electronic devices and systems are used. Tab. 4.1 shows the most relevant quantities in the R2E context, that have been explained in the last chapters.

Tab. 4.1.: R2E relevant quantities defined to characterize a mixed-field radiation environment. García Alía, 2014

Quantity	Notation	Definition
High Energy Hadron (HEH) flux	Φ_{HEH}	Hadron flux above 20 MeV. Available as a generalized particle in FLUKA under the name HADGT20M
High Energy Hadron Equivalent flux	Φ_{HEHeq}	Hadron flux above 20 MeV plus the intermediate neutron fluence. Available as a generalized particle in FLUKA under the name HEHAD-EQ
Intermediate neutron flux	$\Phi_{n_{int}}$	Weighed neutron contribution in the 0.2 - 20 MeV energy range according to the Toshiba Rad-MON response
Thermal Neutron Equivalent flux	Φ_{th}	Neutron flux weighed by the $^{10}\text{B}(n, \alpha)^7\text{Li}$ cross section normalized to the value at thermal energy (0.025 eV). Available as a generalized particle in FLUKA under the name THNEU-EQ
R factor	R	Ratio between the equivalent thermal neutron flux and the HEH flux
Hardness Factor 1%	$H_{1\%}$	Energy at which 1% of the total HEH flux lie above
Hardness Factor 10%	$H_{10\%}$	Energy at which 10% of the total HEH flux lie above
Hardness Factor 50%	$H_{50\%}$	Energy at which 50% of the total HEH flux lie above

More information can be found in Thornton, 2016 and García Alía, 2014

Radiation Environment within CHARM

As already stated, the mixed field can be modulated through the beam settings, target and shielding configurations, and the selection of the test position within the facility. To underline the influence of those parameters on the resulting field, a few typical configurations, and their radiation field will be presented in this section.

Fig. 4.3 shows the radiation field within the facility for four configurations: copper

target with and without shielding and aluminium target with and without shielding. As can be seen, the shielding effects especially the positions lateral to the beam, where we can see a drop in the dose of a factor of ~ 10 . The material density of the different targets changes the overall intensity of the mixed field, due to the diverse interaction length.

Additionally Tab. 4.2 shows a comparison of the important quantities for the facility

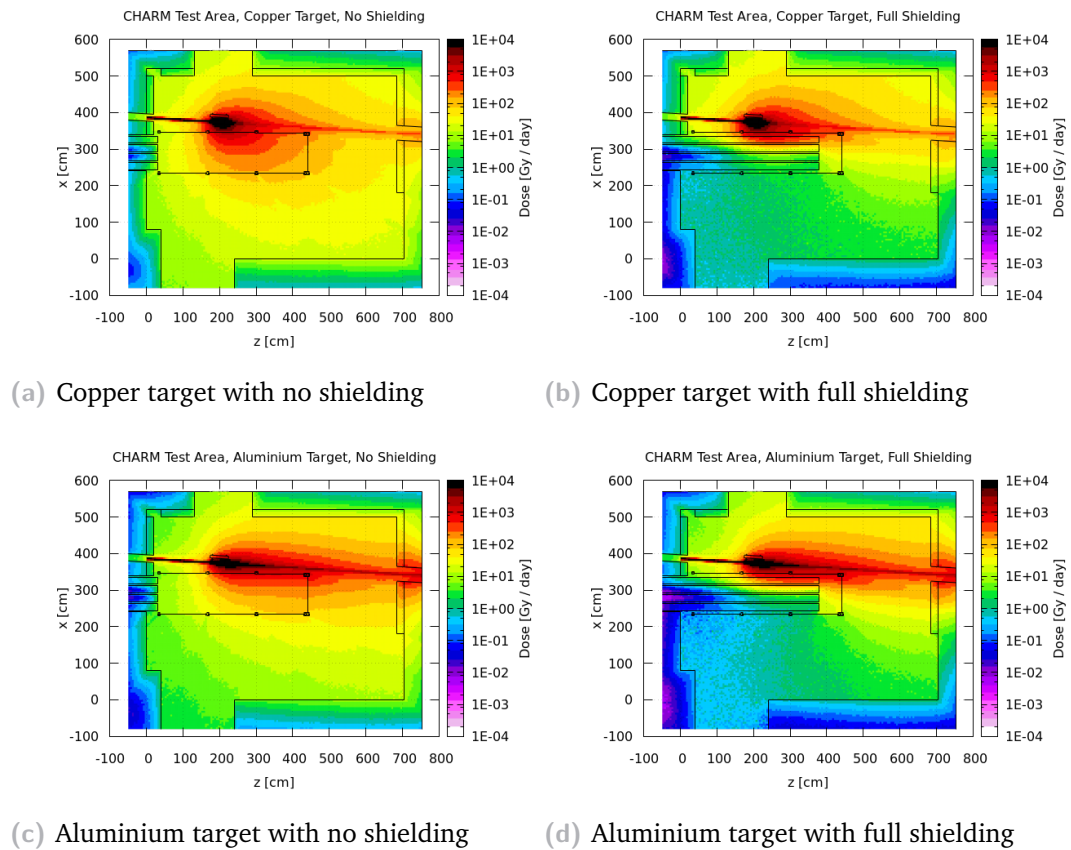


Fig. 4.3.: Comparison of the radiation field within the CHARM facility for four different configurations. The influence of the shielding and target on the resulting mixed field within the facility can be seen. Two target and shielding configurations have been chosen: copper target with full and no shielding at all and the aluminium target, again with full and no shielding at all. FLUKA simulations and plots done by A. Thornton.

for a few selected test positions, lateral and downstream of the beam. Again, the copper target and the aluminium target, with and without shielding have been chosen. An average POT number of $3.3E10$ per second was applied and multiplied with a factor 86.400 to reach a representative value for a day. A full table with all the positions and configurations and their resulting quantities can be found in Infantino, 2017. Furthermore, within the CHARM context the abbreviations cp_OOOO, cp_CIOOO and cp_CIIC are used, to describe the facility settings. The first two letters indicate the target material ("cp" stands for copper, "al" for aluminium and "alh" for aluminium

with holes), and the last four letters indicate the shielding configuration ("O" means open, "C" concrete, and "I" indicates iron).

Tab. 4.2.: A comparison of the average values for specific quantities in typical test positions of the CHARM facility, for different configurations. An average number of $3.3E10$ protons/seconds was used and the values were normalized for one day. Data from FLUKA simulation, done 2017 by A. Infantino. Infantino, 2017

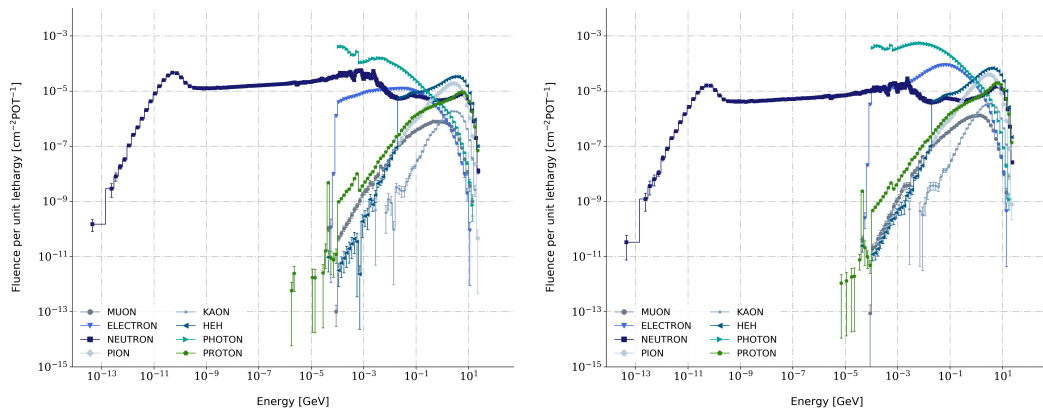
Config.	Dose [Gy/d]	HEH [cm-2]	THneq [cm-2]	R	h50 [GeV]
CuOOOO R1	30	5.67E10	2.03E11	3.58	0.06
CuOOOO R11	147	3.04E11	2.34E11	0.77	1.70
CuOOOO R13	126	2.24E11	2.35E11	1.05	0.70
CuOOOO T0	5630	9.31E12	1.71E11	0.02	0.09
CuCIIC R1	2	3.82E09	1.07E11	28.11	0.06
CuCIIC R11	145	3.24E11	2.31E11	0.71	1.50
CuCIIC R13	130	2.41E11	2.50E11	1.03	0.59
CuCIIC T0	5690	9.37E12	4.48E11	0.05	0.09
AlOOOO R1	12	1.91E10	4.83E10	2.53	0.07
AlOOOO R11	461	5.02E11	8.09E10	0.16	2.56
AlOOOO R13	285	2.85E11	8.21E10	0.29	1.17
AlOOOO T0	2000	2.90E12	3.94E12	0.01	0.10
AlCIIC R1	1	2.02E09	3.55E10	17.57	0.06
AlCIIC R11	468	5.17E11	8.98E10	0.17	2.44
AlCIIC R13	289	2.97E11	9.50E10	0.32	1.09
AlCIIC T0	2020	2.93E12	9.61E10	0.03	0.10

It can be seen that the shielding has a big influence on the dose and the R factor for the lateral positions, whereas R1 was used as a reference point. Indeed, the dose drops for the copper target from ~ 30 Gy to ~ 2 Gy per day, due to the insertion of the full shielding, resulting in a difference of a factor ~ 15 . As pointed out before, the thermal neutron production increases as well and we can see that the R factor rises from ~ 4 to ~ 28 , which gives us a factor of ~ 7 in the thermal neutron production. A comparison of the particle spectra for the same position (R1) but changing shielding material can be found in Fig. 4.4.

The comparison between the copper and the aluminium target shows that, due to the lower density of the latter one, fewer interactions between the primary protons and the target material happen, and therefore a higher dose deposition in the downstream positions, can be seen due to the higher proton share in the resulting field. Indeed, the comparison of the HEH fluence numbers between CuOOOO R11 and AlOOOO R11 show that there are more high energy hadrons in the total spectrum.

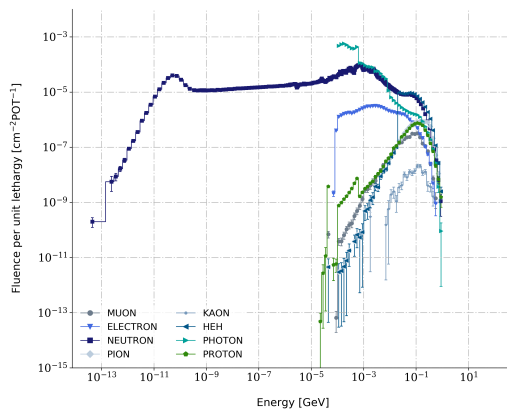
The intensity in the dose for the rest of the facility, especially the lateral positions, will drop due to this target material, as can be seen when one compares the absolute dose values for the position R1 in the Tab. 4.2 for the two target materials or compares the

dose distribution in Fig. 4.3.

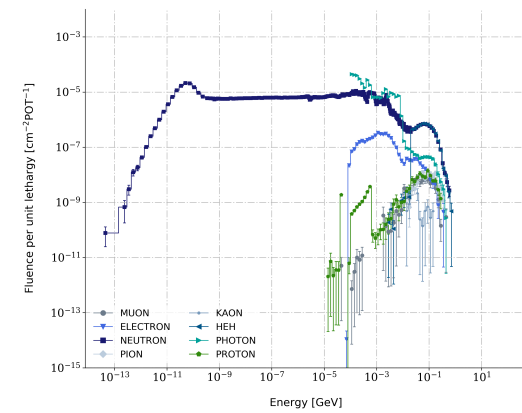


(a) Copper target with no shielding, R11

(b) Al target with no shielding, R11



(c) Copper target with no shielding, R1



(d) Copper target with full shielding, R1

Fig. 4.4.: Particle spectra for different configurations and positions in the facility. The first row compares the spectra for the position R11 with no shielding, for two different target configurations: copper and aluminium. The second row compares the particle spectra for the position R1 with the copper target, for two different shielding configurations: no shielding and full shielding. FLUKA simulations done by A. Infantino, analysis and plots by M. Krawina.

The mixed field present at CHARM is complex and depends on various different factors. A lot of work has already been done in the benchmarking and characterization of the field inside the facility, including the various test configurations and positions. Those results can be found in Thornton, 2016 and Infantino, 2017.

Comparison with other radiation environments

In order to compare the radiation field within CHARM with other typical radiation environments, specific parameters are used. As already described, the HEH fluence, the hardness factors, and the R factor are of main interest when describing a radiation field in the R2E context. Critical radiation environments for electronic components

spread from accelerator conditions, where high fluxes are reached and both heavily shielded as well as lower shielded areas are present, up to space applications, for example, the inner proton radiation belt, with severe HEH fluxes, and to ground applications, where the scaling of electronic components and their high numbers in such systems leads to a higher sensitivity and can negatively impact the reliability of systems. Measurements at those environments have been conducted to understand their particle compositions and conditions. To underline the ability of CHARM to reproduce those environments, a comparison will be given in the following chapter. To test the sensitivity and the tolerance of the electronic equipment used in different radiation environments, it is necessary to expose it to a similar radiation field. To achieve a similar radiation field at CHARM sometimes one has to set priorities to achieve a good match, for example when trying to find a test position with the same exposition to particles energies of the same magnitude as the desired mixed field, there may be a compromise between matching the high energy area of the field and getting correct proportions for the low energy ones. The priorities here are strongly dependent on the device under test and its error rate, as a function of energy.

Tab. 4.3.: A comparison of typical radiation environments and their describing quantities. The environmental values have been retrieved by using the QARM online tool, more information can be found in Brugger et al., 2014

Environment	HEH [$\text{cm}^{-2} \text{y}^{-1}$]	R	H50 [GeV]	H10[GeV]	H1 [GeV]
LHC UJ	2.5E+09	10.5	0.08	0.18	0.36
LHC RR	1.0E+09	7.5	0.18	0.69	2.8
LHC Tunnel	6.0E+11	1.2	0.37	1.8	5.7
350m, Geneva	1.6E+05	0.12	0.08	0.34	1.3
10km, Geneva	1.7E+07	0.08	n/a	0.92	5
20km, Geneva	3.8E+07	0.06	0.5	2.9	13
450km, ISS	7.3E+08	n/a	n/a	0.25	0.53
800km, Proba II	2.7E+09	n/a	0.1	0.28	1.5

Tab. 4.3 shows typical radiation environments and their describing quantities, where electronic equipment is used, starting from accelerator and ground applications, over avionics, until space. Fig. 4.5 shows a graphical comparison between the reverse integral spectra of the CHARM positions and typical radiation environments. It can be seen that CHARM is able to cover the majority of them.

Moreover, CHARM is able to reach a high fluence and doses in a short period of time. Indeed, Tab. 4.4 shows the yearly HEH fluxes for the already pointed out radiation environments, whereas we are able to reach a HEH flux of $\sim 10^{11} \text{ cm}^{-2} \text{ d}^{-1}$ for the position R13 at CHARM. Due to that, it is possible to test the lifetime radiation levels of devices within a short time frame. As already pointed out in the section 4.1.2 it is always possible to reduce the flux with a different facility configuration or with changing the test position, therefore with a given average POT number of $3.3\text{E}+10$

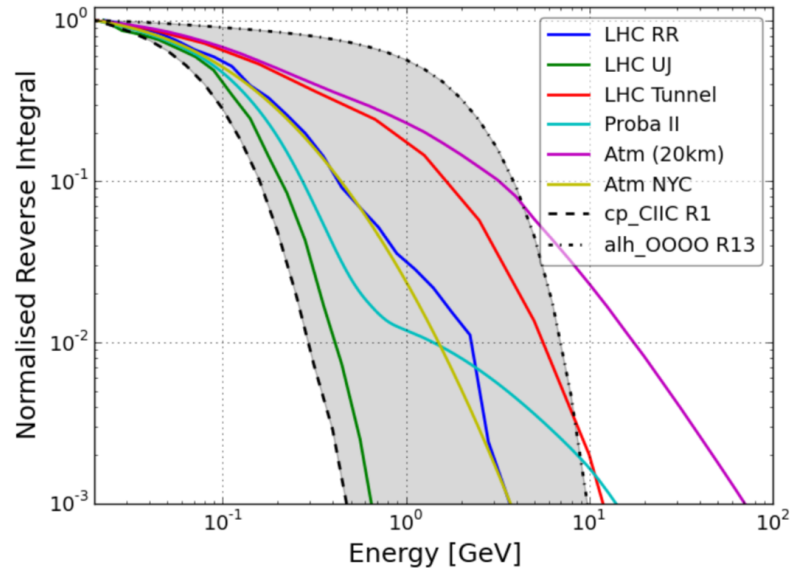


Fig. 4.5.: Comparison between the reversed integral spectra for different test positions at CHARM (in grey) and different radiation environments. The values are normalized to the flux >20 MeV. Thornton, 2016

per second, the HEH flux can be adjusted from a minimum value of $3.5E+7$ HEH/h to a maximum of $9.5E+11$ HEH/h, simply by changing those parameters, as Mekki et al., 2016 has pointed out.

Tab. 4.4.: A comparison of the HEH fluences (> 20 MeV $\text{cm}^{-2} \text{y}^{-1}$) for different radiation environments. Mekki et al., 2016

Spectrum	Ground Level	Avionics	ISS	LHC Machine	LHC detectors
Flux	$1-2 \times 10^5$	2×10^7	10^9	$10^6 - 10^{11}$	$>10^{11}$

The reduction of radiation induced failures of electronics used in the LHC environment is one of the main priorities of the R2E group. The present mixed field nature makes it challenging to perform a correct error rate estimation, due to the different particle types and energies. Therefore the testing of equipment in a similar field, but elevated flux is invaluable for radiation defects impact evaluation and mitigation. The LHC environment can be classified in a first approach in tunnel areas and shielded areas or alcoves. The first one hosts typically radiation-hardened systems, operating COTS, whereas the later one mostly uses COTS. The two shielded areas or alcoves are named UJs and RRs, whereas the UJs are heavily shielded areas close to interaction points and RRs lightly-shielded ones with less intense, harder spectra than their more protected counterparts. (García Alía, 2014)

The HEH fluences, the R-factor and the H-factors for those LHC environments, compared with some typical CHARM positions can be found in Tab. 4.5. Fig. 4.6 shows a graphical comparison between the reversed integral spectra for the LHC environment

Tab. 4.5.: A comparison of the LHC environment and matching test positions and configurations from the CHARM facility. FLUKA data can be found in Infantino, 2017, LHC environment in Brugger et al., 2014. The HEH fluences are given in $\text{cm}^{-2} \text{y}^{-1}$ for the LHC environment, and in $\text{cm}^{-2} \text{d}^{-1}$ for CHARM.

Environment	HEH	R	H50 [GeV]	H10[GeV]	H1 [GeV]
LHC - UJ	2.5E+09	10.5	0.08	0.18	0.36
cp_CIOO R3	3.01+10	5.18	0.08	0.23	0.51
LHC - RR	1.0E+09	7.5	0.18	0.69	2.8
cp_OOOO R9	9.81E10	2.55	0.15	0.63	1.42
cp_OOOO R10	1.21E11	2.01	0.19	0.79	1.75
LHC - Tunnel	6.00E+11	1.2	0.37	1.8	5.7
alh_OOOO R13	2.01E11	0.25	1.23	3.88	7.45
cp_OOOO R11	3.04E11	0.77	1.70	6.69	12.57

and some typical CHARM positions and configurations. Within the LHC tunnel locations especially protons, pions and neutrons with high energies are present, whereas in the shielded areas neutrons dominate the spectra: In the UJs, they makeup to 98 % of the HEH fluence and in the RRs around 70 - 90 %.

The presented data show a good agreement between CHARM and the LHC areas,

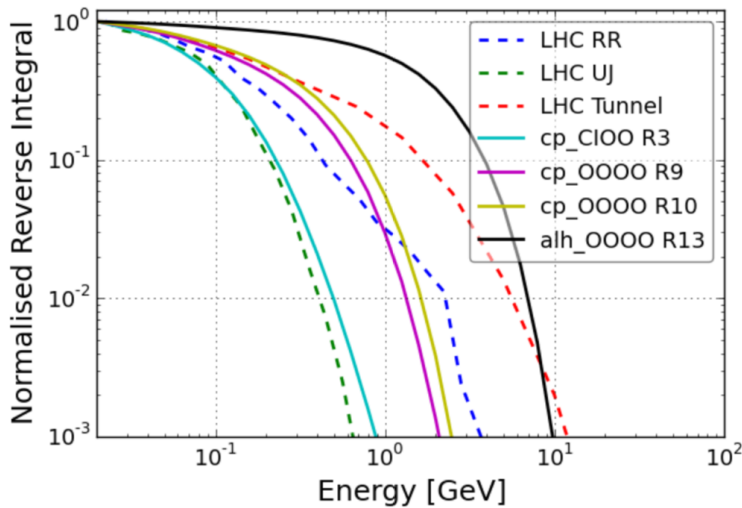


Fig. 4.6.: Comparison between the reversed integral spectra for different LHC environments with typical positions in CHARM. FLUKA simulations and plots made by A.Thornton Thornton, 2016

more details and comparisons with the other environments can be found in Thornton, 2016 and Mekki et al., 2016

4.2 Challenges

The radiation field present at CHARM is complex and can change a lot of its properties throughout the facility. If one sums up the different arrangements possible within CHARM, taking into consideration the target, shielding and positions, more than 150 configurations are possible. A detailed benchmarking from an experimental point of view is sheer impossible to attain, both from manpower and time restrictions.

The challenges both in calibration as well as in the dosimetry of CHARM, are key points for ensuring the reliability and reproducibility of the tests within. Indeed, an accurate characterization of the radiation field is mandatory and can only be achieved with the help of simulation tools. As will be explained in the section 5.2 a model of the facility within FLUKA has been built and simulations have been done throughout the planning and building of the facility to have a preliminary benchmarking. Now, FLUKA is used as a strong help for ongoing campaigns, characterizing and benchmarking the radiation field and test positions.

FLUKA

An important tool and great help in our work has been FLUKA. FLUKA is a fully integrated particle physics Monte Carlo simulation package, including accurate particle transport and interaction with matter. It has been extensively validated and benchmarked in different applications throughout the world and topics, reaching from high energy experimental physics and engineering, shielding, detector and telescope design, cosmic ray studies, dosimetry, medical physics, and radiobiology.

The following chapter will give a brief overview of Monte Carlo simulations, FLUKA in general terms and then focus on the FLUKA CHARM model that has been used in this work.

5.1 Introduction to FLUKA

FLUKA (coming from the German expression **F**luktuierende **K**asskade) is a general purpose Monte Carlo simulation package, which modern physical models implemented that help to calculate particle transport and interaction with matter methods. It is able to simulate with high accuracy interaction and propagation in matter of around 60 particles at different energies, as well as their antiparticles. Furthermore, it is possible to build and work with complex geometries. FLUKA is created and developed mainly by CERN, particularly within the EN/STI-FLU (formerly EN/STI-FDA) department, and is written in the programming language FORTRAN.

It has been developed in the 1960s in the frame of collaborations between many European research institutes, but the base of the FLUKA code that is used today was built in the 90s. Various physical models, algorithms, and techniques are used within FLUKA to describe and simulate the production, transport, and interactions of particles correctly. Most of them can be either found in Ferrari A., 2005 and Böhlen et al., 2014.

Monte Carlo simulation

The base of FLUKA is the Monte Carlo method. Dunn and Kenneth Shultis, 2011 defines Monte Carlo technique as following

"The analysis technique called Monte Carlo is, in essence, a methodology to use **sample means** to estimate **population means**. In essence, Monte Carlo is a highly flexible and powerful form of quadrature, or numerical integration, that can be applied to a very wide range of problems, both direct and inverse"

These techniques or methods are mainly used to calculate multidimensional integrals numerically, where the integrand $f(x)$ may only be known at certain points, is difficult to find an antiderivative or it is simply easier to compute a numerical approximation. Nowadays Monte Carlo is mostly used with the help of modern computer application. Monte Carlo gives us the ability to find answers for a wide range of problems and is a very flexible and powerful form of quadrature or numerical integration for plenty of problems.

A detailed introduction and analysis of Monte Carlo Methods are given by Dunn and Kenneth Shultis, 2011 and only a brief overview will be presented here. Considering the function $z(x)$, that is dependent on a variable x , the expected value can be written as

$$\langle z \rangle = \int_a^b z(x)f(x)dx \quad (5.1)$$

whereas $f(x)$ gives the probability that the variable x has a value within dx . Ideally, the right side of the equation 5.1 can be solved analytically, but in many real-life situations the integrand is too complex to rely on analytical solutions: sometimes the integrand is even unknown. Monte Carlo techniques offer a solution for both cases. The first step of this is to convert the integral in sum, with finite number of steps. Equation 5.2 shows the function $f(x)$, which is known, or can be evaluated, in a finite set of points x_i , fixed or selected, and it is possible to define a **quadrature rule** or **quadrature formula**. The real numbers x_i are called **nodes** and the w_i is called weights or coefficients of the quadrature rule. Quadrature is nothing more than approximating integrals by finite summations.

$$I = \int_a^b f(x)dx \quad (5.2)$$

Considering this, it is possible to approximate the integral from equation 5.2 to a sum of the product of the function at those nodes, and the weights. This can be seen in the equation 5.3.

$$I = \int_a^b f(x)dx \cong \sum_{i=1}^N w_i f(x_i) \quad (5.3)$$

The most common quadrature rules use an interpolating polynomial $P_n(x)$, of grade n , to approximate the function $f(x)$ (interpolatory quadrature rule). When $f(x)$ is a polynomial of grade $\leq n$ the interpolating polynomial corresponds to the integrand function and fitting error is null. Gaussian quadrature rules uses as nodes x_i the

roots of polynomial belongs to a class of orthogonal polynomials, for example Gauss-Legendre or Gauss-Jacobi.

Monte Carlo techniques are used for estimating expected values, that can be expressed as integrals and almost any integral can be interpreted as an expectation. Monte Carlo is applied to estimate the values of those definite integrals. The expected value is called the **population mean** and described in the equation 5.4, whereas the estimate of the population mean is called the **sample mean** and described in the equation 5.8. $f(x)$ is normalized, which helps to reach the sample mean.

$$\langle z \rangle = \frac{\int_a^b z(x)f(x)dx}{\int_a^b f(x)dx} \quad (5.4)$$

$$\langle z \rangle = \int_a^b z(x)f(x)dx \cong \sum_{i=1}^N w_i z(x_i) f(x_i) \quad (5.5)$$

where

$$F(x) = \int_a^b f(x)dx = 1 \quad (5.6)$$

which leads us with given

$$w_i = \frac{1}{N \cdot f(x_i)} \quad (5.7)$$

to

$$\bar{z} = \frac{1}{N} \sum_{i=1}^N z(x_i) \quad (5.8)$$

$f(x)$ is called the **Probability Density Function** (PDF) with the requirements that it is defined on the interval $[a, b]$, is nonnegative on that interval (even though it can be zero for values) and is normalized. $F(x)$ is the **Cumulative Distribution Function** (CDF) and is by definition $F(a) = 0$, $F(b) = 1$ and $F(x)$ is monotone increasing. For the Monte Carlo method, the approach for the numerical quadrature is that the abscissas are chosen randomly according to the PDF $f(x)$. $F(x_i)$ represents the probability that a random sample of the stochastic variable x will assume a value between a and x_i , so $Pro(a \leq x \leq x_i) = F(x_i)$.

Monte Carlo is based on two fundamental statistical results: the law of large numbers and the central limit theorem (CTL). The law of large numbers states that the average of results will converge to the expected value with increasing number of events and can be found in equation 5.9

$$\lim_{N \rightarrow \infty} \bar{z} = \langle z \rangle \quad (5.9)$$

The Central Limit Theorem, on the other hand, states that for a large number of events, the distribution of averages of N independent random variables identically distributed will tend to a normal distribution. Or as Fasso et al., 2009 states "Given any observable A , that can be expressed as the result of a convolution of random processes, the average

value of A can be obtained by sampling many values of A according to the probability distribution of the random processes".

Monte Carlo methods are not limited to single integrals but are in fact superior to many other quadrature schemes for multidimensional integrals. Independent from the number of dimensions m , the precision of Monte Carlo methods are at worst $N^{-1/2}$, with N as the number of histories, therefore Monte Carlo is already superior to other quadrature methods, that have a precision of $N^{-1/m}$, for dimensions greater two. Since the majority of physical problems are only solvable in multidimensional integrals, for example, transport equations for particles, Monte Carlo methods are an excellent approach to work with them. More details about the Monte Carlo method can be found in Dunn and Kenneth Shultis, 2011.

In terms of this thesis, the definition "Monte Carlo simulation" will be used to the fact that we use the Monte Carlo method within a simulation framework. For the majority of the applications, the reality is simulated with a virtual experiment due to the impracticality of doing many measurements or observations in reality. The ability to reproduce the experimental conditions within a FLUKA framework and get valuable results is a big advantage.

FLUKA Input

FLUKA requires an input file, that includes all the necessary information regarding the physical problem, in form of an ASCII file with the extension `.inp`. Due to historical reasons, the structure of this input file is simple and consists of a various number of "commands", that have one or more lines, which are called *cards*.

Typically the input file structure includes following options:

- an **optional** title and comments for documentation purposes
- a **mandatory** definition of the particle source
- a **mandatory** description of the experimental geometry, consisting of solid bodies and surfaces
- a **mandatory** definition and assignment of correct materials to the geometry
- **optional** biasing or problem settings like energy cut-offs, step size, non-default physical effects ...
- a **mandatory** initialization of the random number sequence

- a **mandatory** starting signal and number of requested histories

Each of these cards contains one keyword, six floating point values, that are referred as **WHATs**, and one character string, referred as **SDUM**, although it is not necessary to use all WHATs and the SDUM. If filled out correctly a typical input card should have the format, as can be seen in Fig. 5.1.

```

BEAM      200.      0.2      1.5      1.2      0.7      1.0      PROTON
*...+...1...+...2...+...3...+...4...+...5...+...6...+...7...+...8
BEAM      200.      0.2      1.5      1.2      0.7      1.0PROTON

```

Fig. 5.1.: Example input card for the definition of the particle source. It describes a primary proton beam, with an energy E of 200 MeV, a momentum of Δp of 0.2 GeV/c, a beam divergence of $\Delta\phi$ of 1.5 mrad and an extent of Δx and Δy of 1.2cm and 0.7 cm respectively (Ferrari A., 2005).

After creating a correct input file, with properly defined cards, one can start the FLUKA simulation or "run" it. This can either be done via command line instructions or through the FLUKA GUI that has been created and will be described in the next subsection. Mandatory parameters to start a run are the number of cycles and primary particles, that have to be simulated. If a cluster is available the simulation can run in parallel on different machines to decrease the total CPU time.

flair

A graphical user interface for FLUKA has been released in 2007 and is called **flair** (FLUKA Advanced Interface). The main advantage is the simplicity of the syntax and input, in comparison to the strict format of the input files. It is written in the scripting language Python, the graphical interface is created with Tkinter and it uses gnuplot to create plots directly within itself. Furthermore, it creates its own filetypes with the `.flair` extension and was extended 2010 with a *Geometry Viewer* that makes it not only possible to illustrate the input geometry directly in **flair** but also to create or modify already existing geometry. Fig. 5.2 shows the same input as has already been for the example input in Fig. 5.1 within the **flair** environment, whereas Fig. 5.3 shows the CHARM FLUKA model within the *Geometry Viewer*.

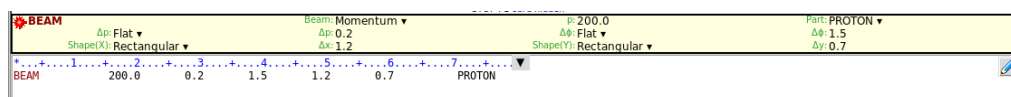


Fig. 5.2.: Example input card for the definition of the particle source. It describes the same primary proton source as Fig. 5.1. The input via **flair** is simultaneously interpreted in the strict structure of the conventional input file and can be seen below.

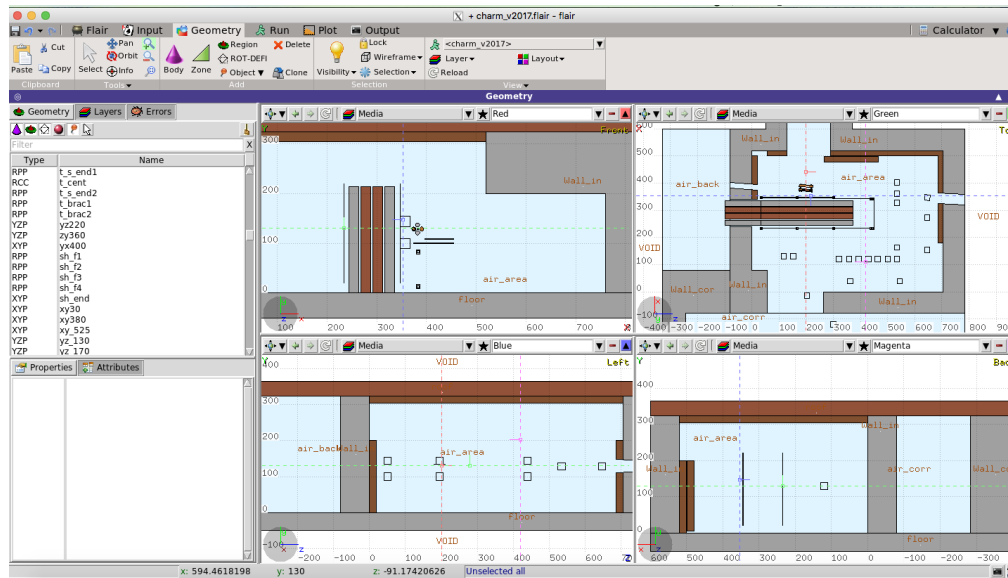


Fig. 5.3.: Visualization of the geometry of the CHARM FLUKA model, as seen in the flair geometry viewer.

5.2 FLUKA model of the CHARM facility

The CHARM facility has been fully modeled within FLUKA within the EN-STI-BMI department, within the R2E project. The first model of the full irradiation room was built by the former employee Adam Thornton. This preliminary version was adapted and modified, especially for the detailed placements of the objects within the room and the used thresholds, by Angelo Infantino and Melanie Krawina. The aim of the CHARM FLUKA model is to support ongoing campaigns, investigate the radiation field present with an accuracy and preciseness that is not attainable with experimental methods and to benchmark the facility.

The current model includes a detailed geometry: the walls, floor and ceiling, the target revolver (including the interchangeable target material), the different shielding layers and the positions of the standard test positions. It was based on the technical drawings and double-checked with measurements made in the facility, to reduce the uncertainties regarding the positioning within the model.

The FLUKA model was first used to perform the radiation field calculations for the CHARM test area and up to this date to make assumptions regarding radiation levels at specific positions with respect to planned experiments or to crosscheck experimental data. Due to the complexity of the mixed field present within the facility, an accurate benchmarking and knowledge of the radiation levels present is necessary for the reliability reproducibility of the tests. Furthermore, due to the **150+** possible test configurations within the facility, a benchmarking and calibration from the experimental point of view is not feasible and FLUKA is a strong tool to do this.

For this specific radiation gradient campaign, additional settings have been chosen to

suit the challenges and the nature of the work in the best way. Based on the already presented input parameters for FLUKA in the subsection 5.1, this section will highlight the used specifications and values for the radiation gradient campaign.

Particle source

The facility receives a 24 GeV/c proton beam from the PS accelerator. There are two possible modes selectable from FLUKA, linked with an if statement: The first one is the blown-up Beam (BUB) which is a state of operation, where the target is fully removed and the proton beam alone is used for experiments. This configuration was not used for the radiation gradient campaign. The second mode is used when the target revolver is inserted in the facility, and the beam hits the target to create the mixed field.

This mode is called *t_beam* in the input file and in Fig. 5.4 it can be seen, that the source is simulated with a flat, Gaussian proton beam, that has a momentum of 24 GeV/c, and a spread of 2.2 cm (FWHM) in both x- and y-direction. Due to simplicity reasons, the facility is built parallel to the origin of the coordinate system within flair, and the beam enters the facility at an angle. In our FLUKA system the y-axis corresponds to the height within the irradiation room, the z-axis is longitudinal to beam and the x-axis is lateral to it.

#if	in_beam			
Define the beam characteristics				
*BEAM	Beam: Momentum	p: 24.0	Part: PROTON	
	Shape(X)	Δ: Flat	Δ: Flat	Δ: 0.0
	Shape(Y)	Gauss	Shape(Y): Gauss	y(FWHM): 12.0
#elif	t_beam			
Define the beam characteristics				
*BEAM	Beam: Momentum	p: 24.0	Part: PROTON	
	Shape(X)	Δ: Flat	Δ: Flat	Δ: 0.0
	Shape(Y)	Gauss	Shape(Y): Gauss	y(FWHM): 2.2
#endif				
Define the beam position				
*BEAMPOS	x:	386.	y:	129.
	cosx:	-.0610485	cosy:	0.0
			z:	0.1
			Type:	POSITIVE

Fig. 5.4.: Input card for the primary source of the CHARM FLUKA model. As can be seen from the input parameters, we simulate the 24 GeV/c proton beam, as we have in real life. Screenshot was taken directly from flair.

Geometry and material assignment

As already explained, the full geometry of the CHARM FLUKA model is extensive and an in-detail look would be dragging. Nevertheless, the full geometry of the facility can be seen in Fig. 5.5, where it is visible that the floor, the walls, and the marble shielding layers are fully simulated. Furthermore, the shielding and its frame, that is surrounding it, can be seen as well. A more detailed look at the target revolver and the table on which it is standing can be seen in Fig. 5.6, furthermore the test positions of interest during this campaign are marked as well. At Fig. 5.6 a) next to the target

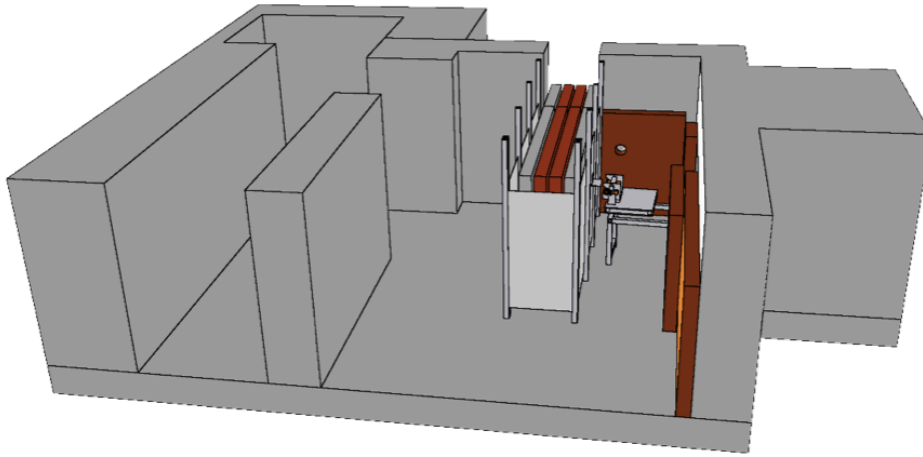
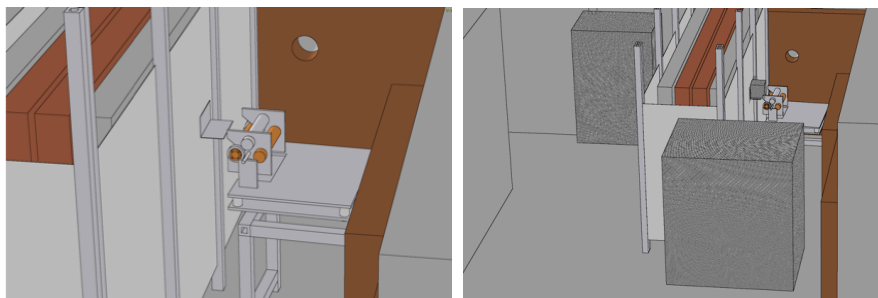


Fig. 5.5.: The full CHARM FLUKA model, that includes the shielding, the target revolver and more details. Screenshot taken directly from *flair*.

the aluminium table is visible, which is our test position T0, that will be described in detail in Chapter 6. Fig. 5.6 b) shows the cartesian meshes that were created over the test positions of interest within FLUKA. More details about those meshes and the *scoring* parameters will be presented in the scoring subsection.

Not only the correct dimensions of the facility and its belongings were considered, but the right material composition as well. This includes the correct marble and concrete composition with the right density, but also the different materials for the target revolver. A special case is the aluminium with holes target, which consists of aluminium disks with spaces of air between them, which is simulated as full aluminium target, but with a reduced density. The goal is to simplify our model as good as possible, to reduce CPU time and in the building of the geometry while maintaining excellent results, that come as close as possible to the real-life applications.



(a) a) The target revolver, with the different materials, on its moveable support is visible, next to the T0 testing position. (b) b) The three cartesian meshes that cover the test positions downstream and lateral to the beam are visible.

Fig. 5.6.: A more detailed look into the geometry of the CHARM FLUKA model. The focus is on the area around the target revolver and the test positions used during the measurement campaign. Screenshots taken directly from *flair*.

Scoring, Transport, and Biasing

FLUKA makes it possible to configure the transport of certain particles and the likelihood of interactions by changing parameters. This is another example where a 'tuning' of the simulations leads to satisfying accuracy while reducing the CPU time and/or complexity of the input, as has already been explained in the previous section. An example of this is the possibility to change the transport thresholds for various particles, like electrons or positrons, that can be set to a specific energy. The two extrema for this case would be to raise the thresholds or even stop the transport completely, which would reduce the CPU vastly, or to reduce the energy to such an extent, that all physical effects are considered, but the CPU times increases to a level, where it becomes a limiting factor to gain an acceptable level of accuracy in terms of statistics. (Thornton, 2016)

Even though the specifications change from application to application, there are a few standard input parameters which resulted in a good agreement in previous simulations and are therefore preferably reused in new simulations. One of them would be the NEWDEFA PHYSICS default card, which enables the transport of electrons and positrons, enables the low energy neutron transport down to thermal energies, sets particle transport thresholds to 10 MeV, except for neutrons (1E-5 eV), lowers multiple scattering threshold for secondary charged particles to 20 MeV and many more.

Additionally, other threshold cards were added during the work of this thesis to modify the particle transport even further. For example, for protons, pions, muons, and kaons the threshold was set to 100 keV. The one for electrons, positrons, and photons was lowered to 100 keV as well with the EMFCUT card, and for an additional run, where the contribution of the electromagnetic components to the total dose was analysed, those values were lowered even more: A threshold of 50 keV for electrons and 10 keV for photons was set. The delta-ray production by muons and charged hadrons was modified via the DELTARAY card and set to 100 keV. Moreover, it is possible to decrease the CPU time even further with setting a biasing card, but this was not used in this campaign.

To estimate the values for different quantities, for example, the deposited dose in the air, charged particle fluence etc., a scoring card has to be set in FLUKA. Based on the type of simulations and the quantity of interest, this will change. Generally speaking is the focus of the CHARM facility to test electronics, for which a number of appropriate estimators are built into FLUKA. Tab. 5.1 shows the most important and used estimators for the CHARM facility.

For the radiation measurement campaign, fine USRBIN cartesian meshes were created, that covered the test positions of interest. The dimensions of one bin were 0.5 x 0.5 x 0.5 cm to guarantee a good resolution but also suitable statistics and low uncertainties. The quantities of interests within those meshes were DOSE, HADGT20M,

Tab. 5.1.: Different estimators that are regularly used within the context of the CHARM facility. Table from Thornton, 2016, a more detailed list and further descriptions can be found in Ferrari A., 2005

Estimator	Physical Meaning
DOSE	Energy deposited per unit mass
HADGT20M	Fluence of hadrons with energies above 20 MeV
SI1MEVNE	Fluence of 1 MeV (Si) equivalent neutrons
NEUTRON	Fluence of neutrons
HEHAD-EQ	Fluence of Hadrons with energies above 20 MeV, including intermediate neutrons
THNEU-EQ	Fluence of thermal-equivalent neutrons

HEHAD-EQ, and SI1MEVNE and all of them were scored in the air. For this explicit campaign, between 40 and 50 million primary particles were simulated, resulting in small statistical uncertainties for all quantities and positions of interest. The statistical uncertainties given by Monte Carlo will be presented in Chapter 7, for all the positions.

5.3 Challenges

FLUKA simulations have been for a preliminary benchmarking of the mixed field all over the facility and various quantities in the standard test positions have been successfully simulated.

In this first assessment, the various test positions were considered as 20 x 20 x 20 cm cubes of air, placed at the center of each rack or position, and an average value for them was calculated. This approach may be sufficient for some of the positions and configurations, but certainly not for all of them. Indeed, a deeper look into the previous results indicated a strong radiation gradient effect, for multiple quantities like dose and fluence, for a few test positions, whereas the downstream positions like R11, R12, and R13 are affected the most. Newly adopted positions, like the table T0, have not been benchmarked into its full extent and due to the short distance to the target and the high dose rate, a gradient effect has to be expected here as well.

The complex field within the facility poses important challenges both in the calibration as well as in the dosimetry of CHARM, which is a key point for ensuring the reliability and reproducibility of the test. The accurate characterization of the existing radiation gradient effect is mandatory to meet the required high-quality standards for the facility operation and a detailed knowledge of the dose field in the various positions in full detail is crucial for the goodness excellency of the test results. This is particularly a major factor for applications where an exact knowledge of the delivered dose or fluence is fundamental, for example in electronic component lifetimes or material science.

The focus of this work is to characterize and analyze this effect. In addition, the results for the dose gradient assessment have been presented at the IRRMA X conference in Chicago 2017 and sent to the Radiation Physics and Chemistry journal for publication (Infantino et al., 2017a). Furthermore, a CERN note, presenting all the results, has been published as well (Krawina and Infantino, 2018).

Experimental Setup

The radiation environment of stray particles present within CHARM is composed by a mix of charged and neutral hadrons, photons, muons, kaons, electrons and positrons of energies ranging from GeVs down to thermal energies. This complex radiation field poses important challenges in the calibration and dosimetry of the facility, which is a key point for ensuring the reliability and reproducibility of the tests.

In the past, benchmarking campaigns have been conducted to analyze the field throughout the facility and for some standard test positions within. Mekki et al., 2016 reports about the first calibration campaign conducted at CHARM, that can be considered as a baseline. Infantino, 2017 gives more details about the spectra and radiation level data for the standard test positions from a FLUKA point of view. Within this work, the standard test positions are simulated as 20 x 20 x 20 cm cubes of air, placed at the center of the real positions. The reported values can therefore only be considered as an average value for the position in question.

Therefore the next step for an accurate benchmarking of the facility is to go from a general understanding of the radiation field within CHARM to an in-detail knowledge of specific areas. The past campaigns have shown, that there are specific test locations within the facility, where an average value is not sufficient enough to characterize the radiation field present in these positions, due to strong radiation gradient present. This detailed knowledge of the field in some test locations affected by a significant gradient is crucial for the goodness of the test results, particularly with regard to all those applications in which the exact knowledge of the delivered dose is fundamental, for example, electronic component lifetime, material science, etc.

The following chapters will describe the radiation gradient campaign, including the experimental setup, and present a detailed assessment of the radiation field at four test positions within the facility.

6.1 Facility and test positions

To understand the radiation gradient within the facility, four particular test positions were chosen, representative for similar ones or due to their unique characteristics. All of them and the layout of the irradiation room can be seen in Fig. 6.1.

T0 is a newly adopted test position for passive testing, in form of an 15.5 x 13.6 x 30.5 x cm aluminium table. It is installed ~10 cm from the target revolver, 90 degrees

from the beam direction. This test location is used for irradiation of materials and components which need to collect high- doses: on average up to 4 kGy/day can be delivered. Due to the short distance from the target revolver, a strong radiation field is expected in this position: an experimental characterization of this field, as well as a detailed study using FLUKA simulation, is therefore mandatory.

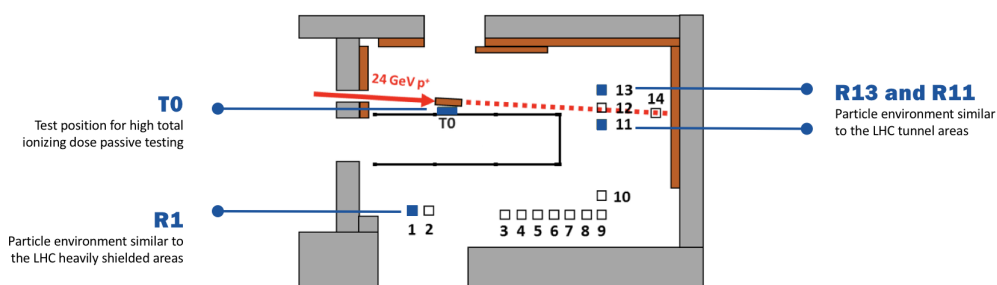


Fig. 6.1.: Layout of the CHARM irradiation room, including the test positions within. The four positions that were of main interest during the radiation gradient campaign are marked in blue.

Test locations 1, 11 and 13 (R1, R11, and R13 in the following) are used for testing electronic equipment and components by means of a rack (60 x 161 x 90 cm) where the boards, the power supply and the signal cables are installed as well and make active testing available. The difference in testing in those three positions is given from the different particle environment available at each location, particularly when the full shielding is completely extracted: in the latter configuration, R1 represents a particle environment similar to the LHC heavily shielded alcoves (UJs and RRs) where the electronics are usually located (Mekki et al., 2016). On the other hand, positions R11 and R13 are representative of the LHC tunnel environment as well as, in terms of SEE rate in a deep-submicron bulk technology, of the atmospheric particle environment at flight altitude (Infantino et al., 2017b). Generally speaking, the spectra for the positions R11 and R13 are harder, compared to the lateral ones.

Due to the downstream placement of positions R13 and R11, a strong gradient effect is to be expected here. If one considers the real dimensions of the racks, R11 is actually in beam¹, so a high dose and HEH fluence is present and a stronger radiation gradient is to be expected, compared with R13. Overall the spectra for both positions are quite similar, even though the shielding configuration has more influence on position R11. R1 was picked representative for the positions lateral to the beam, to confirm the assumption that those positions are not affected by a radiation gradient. Furthermore, the received dose and HEH and 1 MeV neutron equivalent fluence here are strongly dependent on the shielding configuration.

¹Even though the phrase "in-beam" is used, the reader has to consider that this is no longer the collimated beam that CHARM receives from the PS, but the products after the interaction with the target, emitted in a forward direction

6.1.1 Test setup

For the radiation gradient campaign two different test setups were adopted: One for the table position T0 and the other one for the rack positions R11, R13, and R1.

Fig. 6.2 a) shows the experimental setup for T0. 12 RPL (RP1 - RP12) were placed in two different rows along the beam direction, with one row closer to the target and the second one, close to the shielding. Each RPL was placed in a plastic container of 2.5 cm in diameter and 0.8 cm in height. The position of each disk is represented by the RP labels in the plot. In between the two rows of RPL, 6 passive 100 nm RadFETs (RF1 - RF6) were placed, to cover the table even further. Due to the expected high radiation gradient at this position, it was not possible to place both dosimeter types at the same exact position to compare the results to each other. Even a stacking above each other would lead to a different received dose.

Fig. 6.2 b) shows the setup for the rack positions. On the front surface of the rack, a

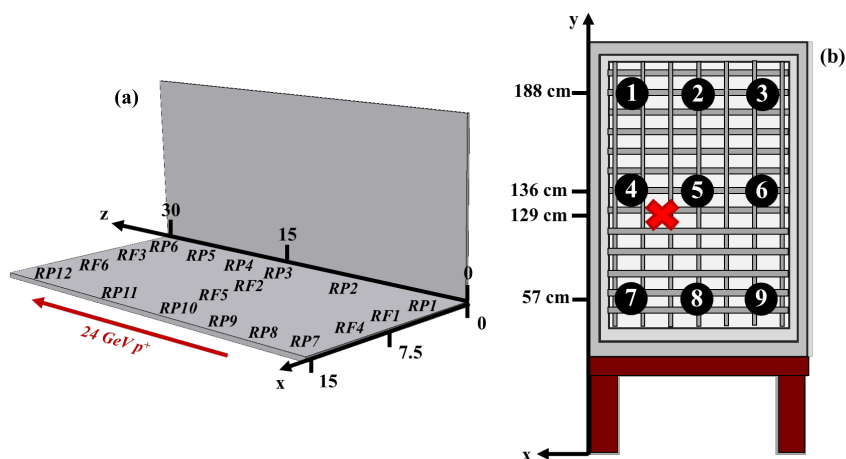


Fig. 6.2.: The two used test setups during the measurement campaign. (a) shows the setup for T0, (b) for R1, R11 and R13. With regard to the R11 irradiation test, the red cross indicates the beam height

metal grid was attached, for enabling the mounting of the detectors on there. A 3 x 3 matrix was set up, and at each point either a RadMON (v6, containing both Toshiba and Cypress SRAM memories) system or alternatively a passive 100 nm RadFET was placed. To be more precise, the RadMON system was placed on the positions 2, 4, 5, 6, 8 and 9 and for the case of R11 and R13, a passive RadFET was placed on the positions 1, 3 and 7. Additionally, an RPL was placed on all the nine positions. For position R1 only the RadMON system was used, with the same positioning on the rack as for the other locations, and nothing mounted on the positions 1,3 and 7.

6.1.2 Test conditions

In order to maximize the field intensity, the irradiation tests were performed running the facility with the copper target an no shielding configuration. An additional set of measurements have been conducted for R1, where the full shielding was introduced. The irradiation time was not longer than six hours for each case, in order to collect a statistically meaningful amount of dose with the different detectors. On average 3 spills per Super Cycle have been extracted from the PS, giving an integrated beam intensity between $2.32\text{E}+14$ and $6.87\text{E}+14$ POT. Tab. 6.1 reports all the parameters for the running of the facility during the campaign.

Tab. 6.1.: Experimental data for the facility for all configurations and positions used during the campaign

Configuration	Time Period	POT
R13 CuOOOO	04/05/2017 15:14 to 04/05/2017 20:53	5.94E14
R1 CuOOOO	09/05/2017 20:08 to 09/05/2017 22:40	2.32E14
R1 CuCIIC	09/05/2017 13:13 to 09/05/2017 19:20	6.87E14
R11 CuOOOO	10/05/2017 11:28 to 10/05/2017 14:00	2.40E14

For the R13 case, the beam was misaligned from its standard central position. This atypical beam condition is hard to quantify and reproducible within FLUKA, therefore the experimental and simulations results cannot be compared with R13. However, it is still possible to analyze the data, experimental and simulation, individually.

The T0 position was irradiated at the same time as R13. Due to the same considerations regarding the misaligned beam and the non-reproducibility of the results, the whole measurement was repeated during the R11 run. All results presented for the T0 position within this thesis are taken from the latter one.

Results

A possible radiation gradient regarding the three main quantities of interest relevant for radiation effects on electronics was analyzed during the campaign: TID, HEH, and 1 MeV neutron equivalent fluence. The results have further been summarized in a manuscript Infantino et al., 2017a and sent for publication, as well as published in a CERN report Krawina and Infantino, 2018.

The following chapter will give a detailed overview of the full benchmark and testing campaign and will present the main achievements of the radiation gradient campaign. The results will be presented in sections, based on the underlying quantity of interest and they will be presented with their uncertainties.

The total uncertainty for the experimental values take into account i) the uncertainty of the SEC1 counter and ii) the uncertainty of the individual dosimeters, taken from the calibration campaign in the ^{60}Co field. The SEC1 is used to count the protons interacting with the target, and an uncertainty of the POT number was considered with 20%, given by the SEC1 for a $1-\sigma$ standard deviation. As already described in Chapter 3, the uncertainty of the RadMON system and its specific components (RadFET, SRAM memories, and p-i-n diodes) are given with 20%. For the RPL dosimeter an uncertainty of 5%, given by the calibration in the ^{60}Co facility. Both uncertainties have a coverage of $1-\sigma$.

The uncertainty of the FLUKA values takes the Monte Carlo statistical uncertainty into consideration. This uncertainty varies between 2% and 30%, based on the position and configuration, and will be presented for each chapter individually. All of the individual uncertainties result in a total uncertainty of the ratio FLUKA/experimental of a quadratic propagation of the i) Monte Carlo statistical uncertainty, ii) calibration uncertainty of the dosimeters and iii) the uncertainty of the SEC1, at a $1-\sigma$ standard deviation and will be presented with that.

7.1 Dose Gradient Assessment

7.1.1 Results T0

Due to the location of T0 close to the target, this position is especially prone to a radiation gradient, since T0 receives the highest total dose and dose rate of all the test positions within the facility. Therefore a strong gradient for the dose spreading over the table is to be expected.

Fig. 7.1 shows a dose contour plot for the surface of the table T0. The gradient can reach a factor of ~ 10 from one extremity (0,0) to the other (30,15), if we consider the whole surface in x- and z-direction. The highest dose is reached at the end of the table, where the particle shower, that gets created from the interaction of the primary beam with the target, has developed the most.

A more detailed look shows, that the variation of the dose along the z-direction (in

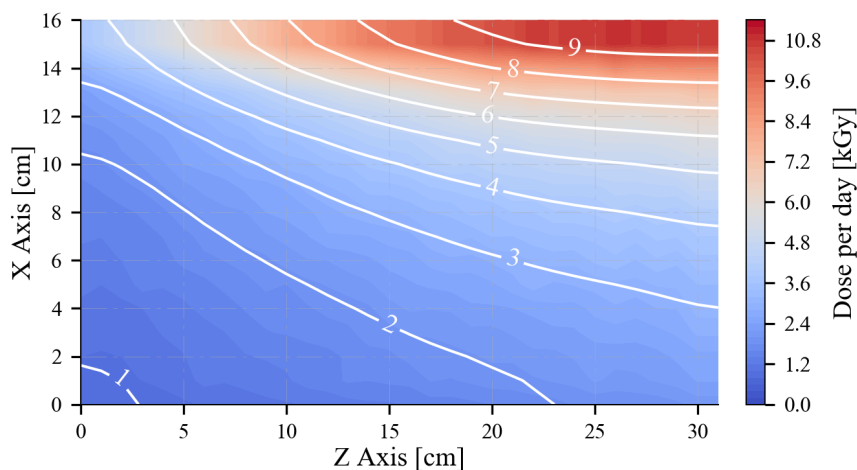


Fig. 7.1.: Dose contour plot for T0 from FLUKA simulation. The integrated dose per day has been calculated considering an average irradiation of 24 hours with 3 spills per Super-Cycle ($1.92\text{E}+15$ POT per day)

beam direction) for three rows in x gives at its maximum a factor of ~ 3 . Analog one can fix the z-coordinate and look at the variation within the x-direction, which gives the order of magnitude of a factor ~ 4 , for the dose gradient. Fig. 7.2 shows the variation for both coordinates for the full table length.

The dose gradient is dependent on the time since the accumulated dose is considered. That means, to compare different irradiation profiles under consideration of the pulsed proton beam from the PS accelerator, it is suitable to report the dose gradient in units of Gy/cm/spill: In terms of FLUKA data this gives a calculated dose gradient along the z-direction of $4.0\text{E}-02$ and $5.0\text{E}-3$ Gy/cm/spill at $x = 0$ and $x = 15$ cm respectively.

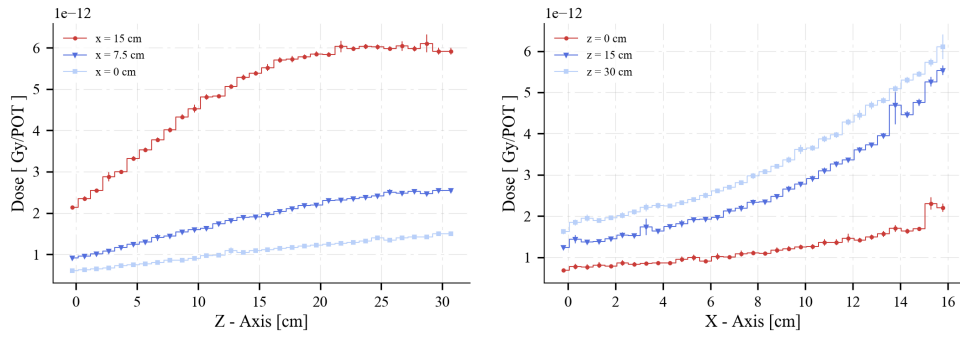


Fig. 7.2.: Dose distribution for the test position T0, both for variation in x- and z-coordinate. The dose is normalized by the number of primary protons interacting with the target (POT).

If one takes into account the conditions of the radiation measurement campaign, with $2.40E+14$ collected POT, a dose gradient of ~ 6 Gy/cm and ~ 30 Gy/cm can be calculated from the FLUKA values and the two rows where the RPL dosimeters were placed, with the stronger effect closer to the target.

Tab. 7.1 shows the comparison between FLUKA results and experimental ones. The uncertainty given by the Monte Carlo simulation is for the whole T0 position no more than 5%, nevertheless, on average it is $\sim 2\%$.

From Tab. 7.1 it is possible to observe how the RPL dosimeter RP1 - RP6 are in a very good agreement with FLUKA simulation, with a weighted average ratio of 0.90 ± 0.08 .

¹ Those RPLs were placed in the row $x = 1.25$ cm, whereas we define the origin at the end of the table, which is closer to the shielding. On the other hand, the RPLs placed at $x = 14$ cm position, namely RP7 - RP12, agree overall with FLUKA within a factor of ~ 2 and result in a weighted average ratio of 1.64 ± 0.14 . As can be seen from Fig. 7.2, a strong dose gradient is present in this area: Small uncertainties in the positioning of the dosimeters can lead to a significant difference in the dose estimation.

Fig. 7.3 shows the dose profile along the z-direction for the FLUKA results, compared with the experimental data: Even if the agreement of the RPL7 - RPL12 is worse than for the RPL1 - RPL6 case, the experimental measurements follow the estimated dose distribution in both cases. As already pointed out, for the area closer to the target, the dose gradient reaches high numbers and the offset between the FLUKA and experimental values can partly be explained with an uncertainty of the positioning. Another cause could be the unknown response of the RPL in a mixed field, especially a possible dose rate dependency or a sensitivity to specific particles or energies. To

¹The weighted average ratio is used to calculate the average value of a particular set of numbers with different levels of relevance. The relevance of each number is called its weight. To be precise, the sum-product by the individual ratios of experimental and simulation data and their weights, given by $(1/\text{uncertainty})^2$ is calculated. This value is then normalized by the sum of the weights.

Tab. 7.1.: Comparison of the FLUKA simulation with the experimental results. A total of $2.40E+14$ POT were collected during the experimental measurement.

Detector	Experimental [Gy]	FLUKA/Exp.
RP1	116 ± 4	1.05 ± 0.22
RP2	171 ± 5	0.82 ± 0.17
RP3	232 ± 7	0.89 ± 0.18
RP4	257 ± 8	0.90 ± 0.18
RP5	303 ± 9	0.92 ± 0.19
RP6	308 ± 9	0.90 ± 0.18
RP7	271 ± 8	1.5 ± 0.3
RP8	308 ± 9	1.8 ± 0.4
RP9	520 ± 16	1.6 ± 0.3
RP10	599 ± 18	1.6 ± 0.3
RP11	665 ± 20	1.6 ± 0.3
RP12	583 ± 18	1.9 ± 0.4
RF1	108 ± 22	1.7 ± 0.5
RF2	190 ± 40	1.7 ± 0.5
RF3	220 ± 40	1.6 ± 0.5
RF4	160 ± 30	1.9 ± 0.5
RF5	260 ± 50	1.6 ± 0.5
RF6	340 ± 70	1.7 ± 0.5

investigate the possible reasons for the offset further, an additional FLUKA simulation was started to analyze the contribution of the electromagnetic share to the total deposited dose and further experimental measurements with the RPL dosimeters in the CERN ^{60}Co facility were conducted. The results for the first one will be presented in the section 7.4, the outcome of the latter one in the section 7.1.5.

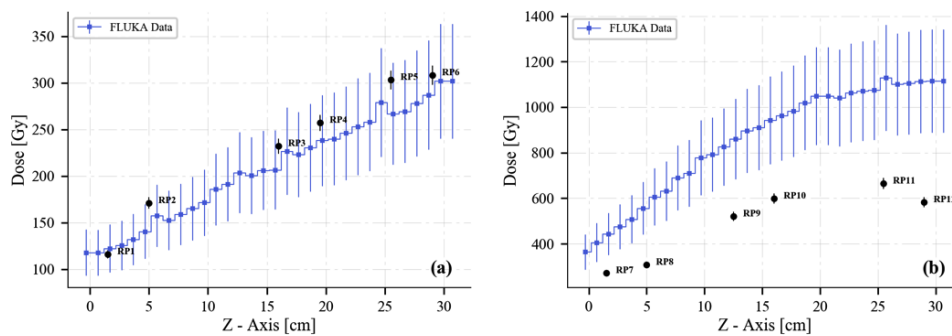


Fig. 7.3.: Comparison between the FLUKA and experimental-evaluated dose distribution along the z-axis (beam direction), at x-coordinates corresponding to the two rows of the RPLs, positioned on T0. a) shows the distribution for $x = 1.25$ cm, b) for the row at $x = 14$ cm. RadFET dosimeters are not reported in the plots since they were placed in another row.

The RadFET sensors agree with the FLUKA data overall within a factor of 2, and the weighted average ratio for the RF1 - RF3, which are located at $x = 5$ cm, give 1.67 ± 0.27 and for RF4 - RF6, located at $x = 10$ cm, this ratio results in 1.71 ± 0.28 . An offset for the two average ratios, as we have seen for the RPL, is not given anymore. The reasons, therefore, are possibly due to the fact that the dosimeters are located close together on the table or that the RadFETs do not have any dependencies that may affect the responses from them.

Even though it is not reported in this work, it is important to underline that the dose gradient is not restricted to the x/z-direction, but a similar gradient is present in the y-direction as well. The result is a 3-D dose gradient, that must be considered for testing at this position.

EM contribution to the total dose

To investigate the offset between the experimental data and the FLUKA data for the row closer to the target, an additional FLUKA simulation was started to investigate the contribution of the electromagnetic contribution to the total deposited dose for the whole table.

The RPL dosimeters are calibrated in a ^{60}Co source, a plain gamma-ray field. The response function of the RPL dosimeters are known for this radiation source, but not for the mixed-field. The assumption was if the particle spectrum is similar to the one within the gamma-ray one, which means a high contribution of the electromagnetic part (which means dose deposited by electrons, positrons or photons), the RPL will react similarly. Furthermore, if a difference between the particle spectra composition between the begin and the end of the test position T0 is visible, this may explain the different response of the dosimeters, regarding the FLUKA results.

For FLUKA the electromagnetic threshold was lowered to 50 keV for electrons and positrons and to 10 keV for photons. The DOSE-EM scoring card was set in FLUKA, which gives the deposited dose from electrons, positrons and photons only, which means electrons, positrons, and photons. The results for the total dose and dose contribution from electromagnetic components plotted along the z-axis can be seen in Fig. 7.4. The actual position of the dosimeters in the radiation campaign were considered as a reference point. From Fig. 7.4 it can be seen that the contribution from the electromagnetic part is constant around $\sim 50\%$, independent from the distance to the target. This leads to the conclusion that a different amount of the electromagnetic contribution to the total dose cannot be the reason that is an existing offset between simulation and experimental results for the two rows at the position T0.

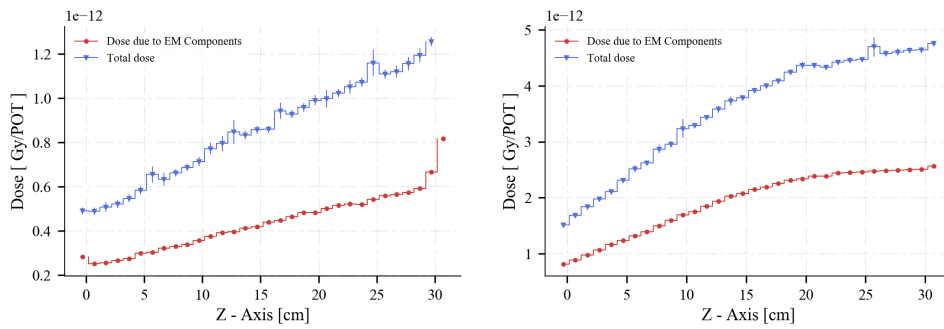


Fig. 7.4.: FLUKA simulation for the dose contribution from the electromagnetic parts to the total dose. The two rows, where the actual RPL dosimeters were placed, were compared and the contribution to the total dose is ~50 % for both of them.

7.1.2 Results R11

The test position R11 is in the downstream direction, at ~2.5 m distance from the target. If one takes the actual dimensions of the rack into consideration, it is visible that R11 is in-beam. Fig. 7.5 shows the dose contour plot at the front surface of the rack, where the detectors were placed. The collimated products from the interaction of the primary proton beam and the target, across the surface of the rack and consequently its full depth, within a small area. Within this 20 x 10 cm space, the dose varies from ~225 Gy to almost ~1200 Gy. FLUKA allows a detailed knowledge of the dose distribution for the whole rack and shows that the part, which is not in beam, displays a quite uniform dose.

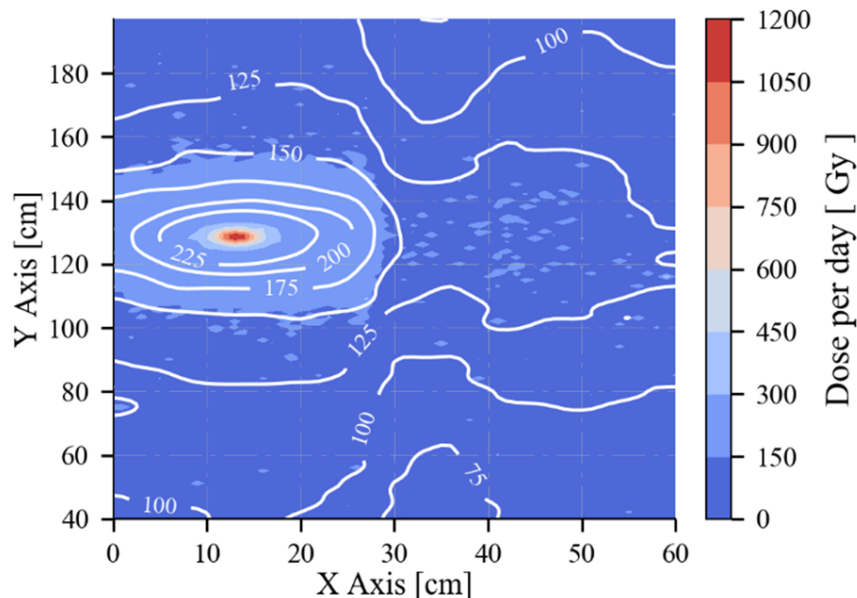


Fig. 7.5.: Dose contour plot for the front face of R11 from FLUKA simulation. The total dose per day has been calculated considering an irradiation of 24 hours with 3 spills per Super-Cycle ($1.92E+15$ POT/day).

Tab. 7.2 reports the results of the experimental measurements in R11, as well as the comparison with the FLUKA simulation. The Monte Carlo statistical uncertainty for the position R11 is not more than 10% for the whole rack, with the average being around 5%. Overall the RPL resulted in a better agreement with the FLUKA simulation, with a weighted average ratio of 1.02 ± 0.07 , while the RadFET resulted in a weighted average ratio of 1.48 ± 0.15 , which is comparable to the results for the T0 position. Regarding the uncertainties in the ratio between FLUKA/experimental values, the same considerations were made as for the position T0. Fig. A.5 shows

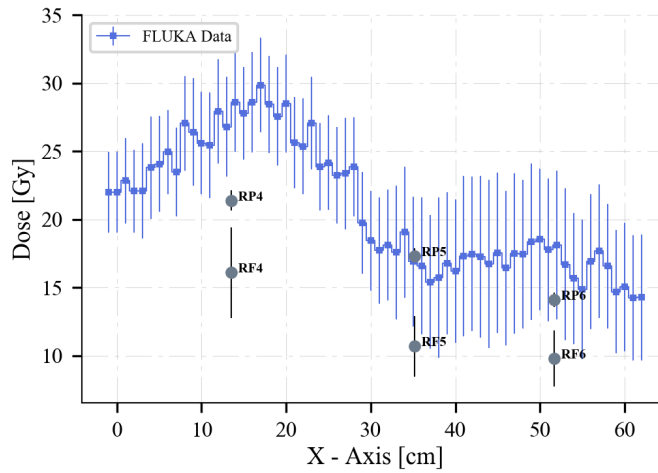
Tab. 7.2.: Absolute dose measured at R11 and comparison with FLUKA simulation. A total of $2.40\text{E}+14$ POT were collected during the experimental measurements. RadFET measurement in Pos. 3 was affected by a readout error, which did not allow to properly evaluate the dose in that position.

Pos.	RPL [Gy]	RadFET [Gy]	FLUKA/RPL	FLUKA/RadFET
1	15.0 ± 0.4	10.6 ± 2.7	0.89 ± 0.18	1.3 ± 0.4
2	14.3 ± 0.3	8.7 ± 2.3	0.80 ± 0.17	1.3 ± 0.4
3	11.0 ± 0.4	n/a	1.15 ± 0.23	n/a
4	21.4 ± 0.9	16 ± 6	1.36 ± 0.28	1.8 ± 0.5
5	17.3 ± 0.6	11 ± 4	1.05 ± 0.21	1.7 ± 0.5
6	14.1 ± 0.5	10 ± 3	1.23 ± 0.25	1.8 ± 0.5
7	14.5 ± 0.5	10 ± 3	1.11 ± 0.25	1.6 ± 0.5
8	10.8 ± 0.3	7.7 ± 2.0	0.91 ± 0.19	1.3 ± 0.4
9	12.0 ± 0.4	8.5 ± 2.7	1.11 ± 0.24	1.6 ± 0.5

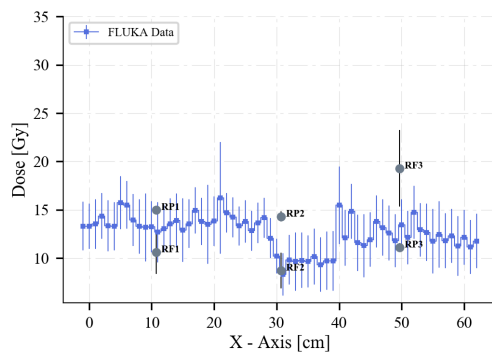
the comparison between experimental and simulations values for the three heights at the rack: top, center, and bottom and for both dosimeter types. Furthermore, R11 allows a direct comparison between the RPL and RadFET measurements, given that the dosimeters were placed at the same position. From the same table a systematic difference between the dosimeter types is observable: Indeed, the ratio RPL/RadFET gives on average 1.47. A similar result was found in the position T0 in a preliminary measurement conducted in 2016 (not reported), where RPL and RadFET dosimeter were stacked together in six different locations for T0: An average ratio RPL/RadFET of 1.27 was found. Finally, a systematic difference of RPL/RadFET of 1.12 was found in experimental measurements conducted at CERN in a pure ^{60}Co field in the past.

Fig. 7.7 gives a detailed overview of the FLUKA dose profile along the x-direction at beam (129 cm) and detector (136 cm) height for the CHARM facility: At the center of the beam spot, the resulting vertical dose difference between beam height and dosimeter height, which are only 7 cm apart, results in a factor ~ 6 . Additionally, at beam height, a horizontal gradient effect for the full rack width can be detected as well, again within a factor of ~ 6 .

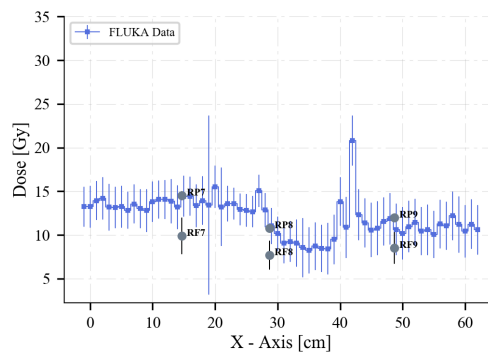
Generally speaking is the horizontal effect for the center part of the rack the most prominent, reaching its maximum at beam height. For the top and bottom part, this horizontal gradient effect is within $\sim 20\%$ and due to the uncertainty of the RadFET



(a) Center of the rack position R11



(b) Top of the rack position R11



(c) Bottom of the rack position R11

Fig. 7.6.: Comparison of the experimental data and FLUKA for the full rack length. The dose has been calculated with the appropriate irradiation time and POT factor of $2.4E+14$. A maximum of the dose can be seen at $x=15$ for the center of the rack, where the beam crosses the rack. A better agreement was achieved with the RPL dosimeters.

detector system not detectable for experimental measurements. Furthermore, there is a vertical gradient effect between the top and bottom of the rack and its center, again with the peak at the position where the beam hits the rack.

EM contribution to the total dose

As already explained in the section 7.1.1, the contribution of electrons, positrons and photons to the total dose has been analyzed for the R11 position as well. As can be seen in Fig. 7.8 for the region $30 \text{ cm} > x > 60 \text{ cm}$ the contribution of this electromagnetic part is around $\sim 50\%$, analogue to the T0 case. After that, the share decreases, due to the fact that this specific area is in beam. At the $x \sim 15 \text{ cm}$ area the beam crosses the rack and therefore a higher HEH flux is to be expected here. For the area $x = 0 \text{ cm}$ the share is back to around $\sim 50\%$. The same pattern was found

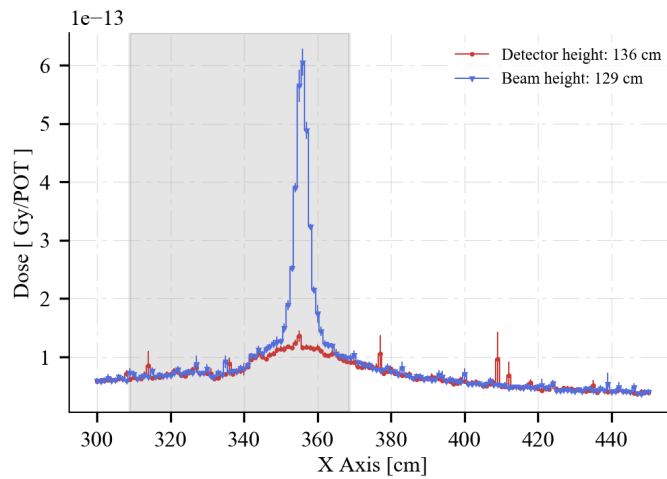


Fig. 7.7.: Dose distribution assessed with FLUKA simulation at the beam and detector height for the CHARM facility. The dose is normalized by the number of primary protons interacting with the target. The grey rectangle represents the rack width of the test position R11 within the facility (see Fig. 6.1).

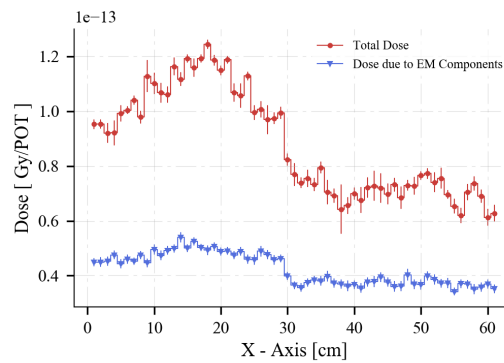


Fig. 7.8.: FLUKA simulation for the dose contribution from the electromagnetic parts to the total dose. This figure shows the center of the rack, where a contribution around $\sim 50\%$ can be seen, with the exception of the $x \sim 15\text{cm}$ region, where the beam is impacting the rack.

for the top and bottom part of the rack, where the electromagnetic share is constant around $\sim 50\%$ for the whole rack width.

In conclusion, the comparison between R11 and T0 results show that independent from the distance to the target (T0 is next to it, R11 a few meters away) the electromagnetic contribution to the total dose is around $\sim 50\%$ for the analyzed positions within the facility.

7.1.3 Results R13

Due to the already explained beam problems during this run, a comparison between FLUKA and experimental data cannot be given. However, a quantitative analysis of the individual cases with the available data will be presented in this section.

Tab. 7.3 reports the absolute values for both dosimeter types as well as for FLUKA. Furthermore, it is again possible to compare the results for both dosimeter types to each other to detect a systematic difference.

FLUKA shows a horizontal gradient effect for all heights, whereas the effect is the strongest for the center of the rack, with a difference of $\sim 40\%$ for the full width. The top and bottom rows show an effect of $\sim 25\%$ and $\sim 36\%$ respectively for the full rack width.

Tab. 7.3.: Absolute dose measured at R13 and comparison between the dosimeters. A total of $5.94E+14$ POT were collected during the experimental measurements. Due to the offset of the beam the comparison with the FLUKA data is not possible.

Pos.	RPL [Gy]	RadFET [Gy]	RPL/RadFET	FLUKA
1	7.27 ± 0.22	7.2 ± 1.4	1.0 ± 0.2	24.6 ± 1.3
2	9.71 ± 0.29	6.7 ± 1.3	1.45 ± 0.29	25.6 ± 0.6
3	10.7 ± 0.3	8.3 ± 1.7	1.29 ± 0.26	30.0 ± 0.7
4	9.9 ± 0.3	6.6 ± 1.3	1.5 ± 0.3	27.7 ± 1.6
5	11.2 ± 0.3	8.2 ± 1.6	1.37 ± 0.28	30.2 ± 0.9
6	14.4 ± 0.4	10.3 ± 2.1	1.40 ± 0.28	38.6 ± 1.0
9	7.57 ± 0.26	6.9 ± 1.4	1.10 ± 0.22	21.8 ± 1.0
8	8.80 ± 0.26	7.0 ± 1.4	1.27 ± 0.26	28.4 ± 2.0
9	10.4 ± 0.3	7.6 ± 1.5	1.37 ± 0.28	29.7 ± 0.7

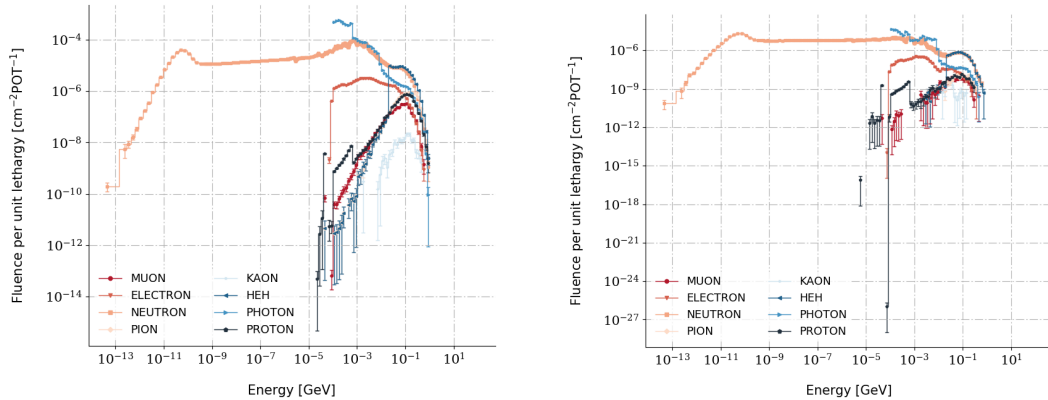
From the experimental point of view, a gradient is visible as well, even though one has to consider the beam misalignment in this case, contrary to the FLUKA results, which took a normal beam setting into account. The RPL dosimeters show a notable horizontal gradient effect for all the three heights on the rack, with values of $\sim 45\%$ for all of them. For the RadFETs only a dose gradient outside of the uncertainty is visible for the center of the rack, with a factor of $\sim 56\%$.

The comparison between the two dosimeter types show a similar result to the already presented one, with an average ratio of RPL/RadFET of 1.30. The difference in the accumulated dose leads to the conclusion that the dosimeters may be sensitive to specific particles and further measurement campaigns are planned, to analyze the behavior for different particles.

7.1.4 Results R1

Position R1 shares the same 3 x 3 matrix setup as position R11 and R13, however only the RadMON system was mounted on a few positions. To be precise, the full system covered the positions 2, 4, 5, 6, 8 and 9. No additional RPL or passive RadFET dosimeters were placed, due to the uncertainty if the minimum readout dose will be reached with them. Furthermore, two measurement campaigns were conducted in this position, due to the strong dependency on the shielding configuration. For the first one, the rack was irradiated with no shielding inserted in the facility, the second

one had full shielding configuration. The shielding has a strong influence on the particle environment at R1, as can be seen in Fig. 7.9, that shows the energy spectra in lethargy form. Lethargy is defined as the differential flux times the geometrical mean of the bin energy and is often used to represent the particle spectra. It is expressed as $\frac{d\phi}{dE} \cdot E$. As can be seen from this figure, the total fluence of all particles is reduced, due to the insertion of the shielding. Generally speaking, this reduction is around a factor of ~ 10 overall.



(a) Particle environment at CHARM for the test location R1 for a copper target with no shielding

(b) Particle environment at CHARM for the test location R1 for a copper target with full shielding

Fig. 7.9.: Comparison of the two particle spectra in lethargy form for the test position R1, for different shielding configurations. The fluence is normalized by the number of primary protons interacting with the copper target (POT)

No shielding

Tab. 7.4 reports the comparison between FLUKA and experimental measurements installed at the test position R1 with no shielding configuration. The Monte Carlo statistical uncertainty given by FLUKA for this position and configuration is no more than 10%, with the average being at 8%. The data shows how in the lateral test location R1, no experimental dose gradient is detectable, with respect to the accuracies and uncertainties of the used RadFET dosimeters. This statement is valid, both for the horizontal as well as the vertical case.

The weighted average ratio between FLUKA and RadFET data gives 0.71 ± 0.09 . Furthermore, it is noticeable that the comparison with FLUKA simulation is overturned compared to R11 and T0.

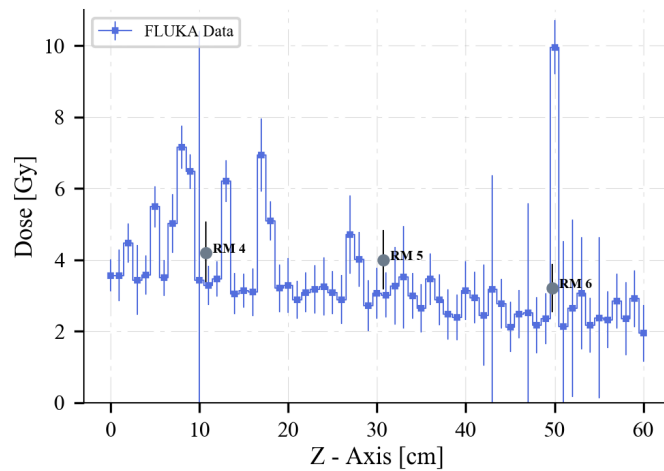
Fig. 7.10 shows the graphical comparison between the experimental data and the FLUKA simulations. As can be seen, no gradient effect is visible for the FLUKA data as well.

Tab. 7.4.: Absolute dose measured in R1 with the configuration Cu_OOOO and comparison with FLUKA simulation. A total of 2.32E+14 POT were collected during the experimental measurements. Only RadFET, installed in RadMON systems, were used for this irradiation test.

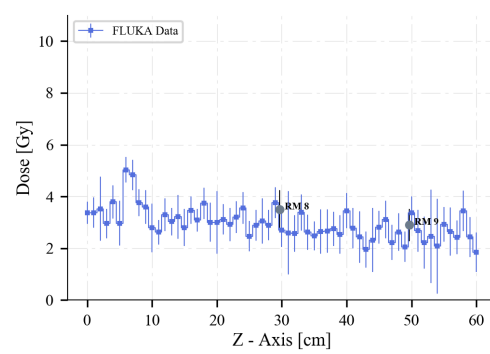
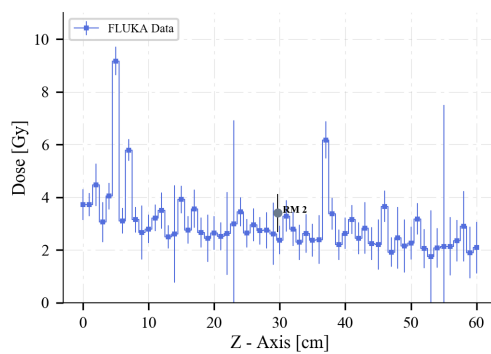
Pos.	RadFET [Gy]	FLUKA/RadFET
2	3.4 ± 0.7	0.68 ± 0.20
4	4.2 ± 0.8	0.76 ± 0.22
5	4.0 ± 0.8	0.73 ± 0.22
6	3.2 ± 0.6	0.70 ± 0.21
8	3.5 ± 0.7	0.74 ± 0.22
9	2.9 ± 0.6	0.68 ± 0.20

The worse agreement and the overturned behavior is probably based on a few reasons. The first one is that during the radiation gradient campaign all FLUKA simulations were scored in the air, within a fine cartesian mesh with a binning size of 1 cm x 1 cm x 1 cm. Scoring within the sensitive volumes of the dosimeters, for instance, the gate oxide of the RadFET sensors would have led to a disproportional increase of the CPU time since the dimensions are several orders of magnitudes lower. Nevertheless, within the air, a possible nuclear interaction between thermal neutrons and Nitrogen can undergo: $^{14}\text{N}(n,p)^{14}\text{C}$ creates a ~600 keV proton, that can deposit energy within an area. This reaction does not take place in the RadFET gate oxide since the thermal neutrons are interacting before reaching the sensitive volume. This effect can lead to an overestimation of the actual absorbed dose for positions, where the thermal neutron flux is high and when scoring in the air. Indeed, as reported by Marzo et al., 2017b, a scoring within the correct sensitive volume can lead to a better agreement. In this campaign, the sensitivity of the RadFET dosimeter and the comparison with FLUKA for the lateral positions at CHARM was analyzed. A ratio of 1.42 ± 0.3 between the FLUKA values, for scoring in air, and the absolute absorbed dose values retrieved by the RadFET dosimeters for R1 with no shielding was achieved. In this campaign, a 20 cm x 20 cm x 20 cm cube of air was chosen as the sensitive volume for R1, and the result has to be considered as an average value for the center of the rack. As a next step, the sensitive area of the RadFETs was modeled within FLUKA and then the dose was scored within: The resulting ratio between FLUKA and experimental data resulted in 1.06 ± 0.24 . As can be seen with those results, a scoring within the correct sensitive region can improve the comparison.

A second reason is that the response function of the RadFET dosimeters is only known for a gamma field and for protons. Dedicated measurements have been conducted and reported by Spiezia et al., 2014. The response of the RadFET in a mixed-field is not known, and first experiments and analysis have been conducted recently. Especially a dedicated study on the sensibility of the RadFET to neutron radiation is currently ongoing and preliminary results can be found in Marzo et al., 2017b and Marzo et al., 2017a.



(a) Center of the rack position R1 with no shielding



(b) Top of the rack position R1 with no shielding (c) Bottom of the rack position R1 with no shielding

Fig. 7.10.: Comparison of the experimental and FLUKA data for the full rack length. The dose has been calculated with the appropriate irradiation time and POT factor of $2.32E14$.

Furthermore, if one compares the FLUKA values from this campaign and the ones reported by Marzo et al., 2017b, a ratio of 0.89 can be obtained. This can be explained due to the fact that there a 20 cm x 20 cm x 20 cm cube of air was considered as scoring volume, whereas in this campaign a 1 cm x 1 cm x 1 cm cube of air was considered. Even though there is a difference between the two values, the comparison is satisfactory. The experimental values retrieved by the RadMON system for this position and configuration, however, show a factor of 2 difference between the two campaigns, that cannot be explained. If one makes the comparison FLUKA (from this campaign)/RadMON (from the previous campaign) the ratio 1.62 is achieved, which is similar to the one Marzo et al., 2017b reported, with FLUKA overestimating the experimental data.

Since only the RadMON system was placed on a few positions on R1 during the radiation gradient campaign, an additional set of measurements was conducted in December 2017 to analyze the possible total accumulated dose discrepancies between the RPL and RadFET dosimeter for the lateral positions inside CHARM. Furthermore,

an attempt was made to get a better understanding of the spread of the accumulated dose within the RPL dosimeters in a mixed field. Therefore 10 RPL dosimeters were placed into one plastic disk, coupled with one RadFET dosimeter and this system was installed at various test positions for different configurations.

For the position R1 with no shielding, a difference in the accumulated dose between the two dosimeter types gives the ratio RPL/RadFET of 0.89 ± 0.18 . As can be seen this ratio is still within the uncertainty of the RadFET sensors, given with 20%, and therefore no systematic difference can be detected. The standard deviation of the 10 RPL dosimeters for this position is given with 4.7%.

Additionally, the same experimental measurement was done at the lateral position R3 (see Fig. 6.1) and an RPL/RadFET ratio of 1.04 ± 0.21 was found. Again, this result is still within the uncertainty of the RadFET detectors, so in conclusion, no different response can be found for both dosimeter types in the lateral positions at CHARM. For the standard deviation along the RPL dosimeters at this position a value of 8.2 % was found.

Full shielding

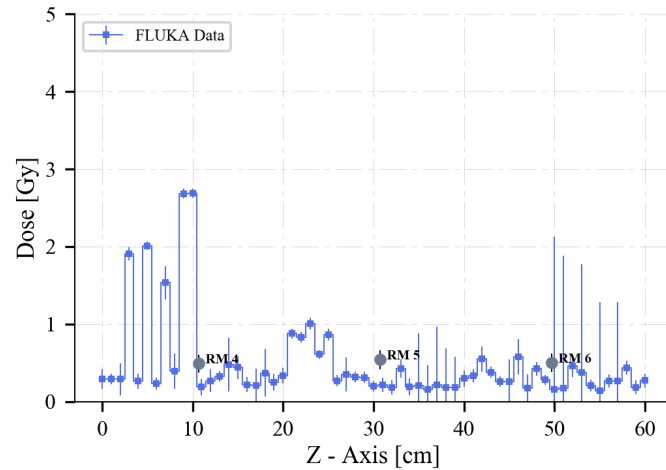
Additionally, the position R1 was irradiated for a few hours with the full shielding configuration during the radiation gradient campaign. Tab 7.5 reports the results of the RadFET dosimeters and the comparison with FLUKA. The Monte Carlo statistical uncertainty given for this position is worse, compared to the other positions, with around $\sim 19\%$ on average, and at the worst being $\sim 31\%$, for the analyzed positions. As can be seen, the comparison gives worse results than the no shielding case, with an average weighted ratio of 0.35 ± 0.05 .

Tab. 7.5.: Absolute dose measured in R1 with the configuration Cu_CIIC and comparison with FLUKA simulation. A total of $6.87E+14$ POT were collected during the experimental measurements. Only RadFET, installed in RadMON systems, were used for this irradiation test.

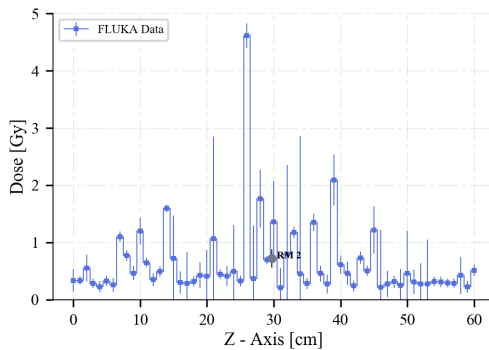
Pos.	RadFET [Gy]	FLUKA/RadFET
2	0.72 ± 0.14	0.29 ± 0.10
4	0.49 ± 0.10	0.38 ± 0.12
5	0.54 ± 0.11	0.40 ± 0.13
6	0.50 ± 0.10	0.32 ± 0.11
8	0.44 ± 0.09	0.43 ± 0.14
9	0.43 ± 0.09	0.40 ± 0.17

Analogous to the no shielding case of R1, no significant experimental dose gradient effect can be seen for the rack, outside of all uncertainties. A graphical comparison between the two data sets can be seen in Fig. 7.11. The visible spikes in the plots

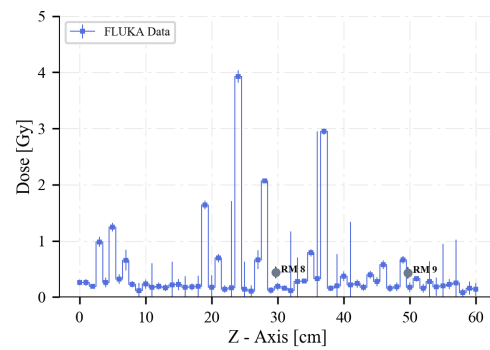
are striking and might be explained from the statistical point of view. Due to the low number of particles that cross the full shielding the simulation may not converge properly in these points. Another effect that might affect this is the very high-resolution with a binning size of 1 cm x 1 cm x 1 cm, which further worsens the convergence of the energy deposition in such volumes. So even though the statistical uncertainty given by FLUKA is satisfactory, with $\sim 19\%$, a bigger scoring volume would probably smoothen out the results.



(a) Center of the rack position R1 with full shielding



(b) Top of the rack position R1 with full shielding



(c) Bottom of the rack position R1 with full shielding

Fig. 7.11.: Comparison of the experimental and FLUKA data for the full rack length. The dose has been calculated with the appropriate irradiation time and POT factor of $6.87E14$.

To the already explained possible reasons for the difference in the values from FLUKA and the RadFET, for the full shielding case, an additional factor plays a role. The worse agreement, compared to the no shielding case, can be explained with the unknown detailed material composition of the geometries within the FLUKA model. For example, the shielding layers made from concrete in real life are simulated with Portland concrete within FLUKA, which is one of the most common concrete types on the market. The exact composition of the used concrete within the facility is not

known, especially the water content has a lot of influence on the particle spectra though.

Furthermore, as already pointed out for the no shielding case, the RadFETs are sensitive to thermal neutrons, according to Marzo et al., 2017a. As can be seen in Fig. 7.12 the shielding configuration changes the particle contribution to the total absorbed dose significantly. A decrease of the charged hadrons for the full shielding case of $\sim 20\%$ is visible, whereas the neutrons contributing to the total dose are almost doubled. The sensitivity of the dosimeter may have an important impact on the final total accumulated dose that they measure.

Finally, an additional set of measurement was conducted for the full shielding case as well, to compare the results of the total accumulated dose for both dosimeter types. For the position R1 an RPL/RadFET ratio of 0.76 ± 0.15 was found, which is slightly out of the uncertainty given by the dosimeters. Furthermore, the difference for the position R3 was checked as well and an RPL/RadFET ratio of 0.86 ± 0.17 was found, which is still within the uncertainty. Based on those results, one can conclude that the differences in the responses of both dosimeter types increases in the mixed field for the downstream positions, which are dominated by HEH and give a harder spectra.

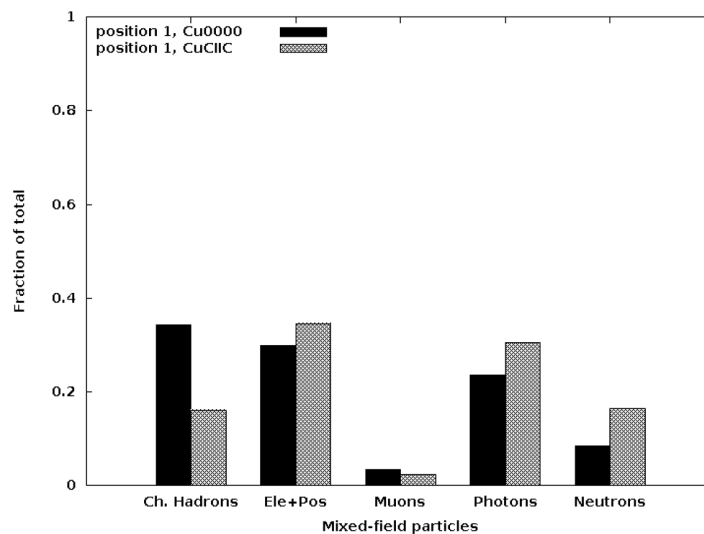


Fig. 7.12.: Comparison of the relative particle contribution to the total absorbed dose for the position R1, with and without shielding. Marzo et al., 2017a

7.1.5 Additional tests at the CERN ^{60}Co calibration facility

There is little knowledge about the response of the RPL dosimeter in a mixed field. Vincke et al., 2007 reports about the use of Alanine and RPL dosimeter at the CERF facility (CERN-EC High Energy Reference field Facility), where the mixed field is generated from the interaction of a 120 GeV/c proton beam and a copper target. Both dosimeter types are calibrated in terms of air kerma by a ^{60}Co or ^{137}Cs source.

The response to other particles than photons and electrons is not well understood, especially in the high-energy range. Furthermore as pointed out by Karacson, 2016 a change of the glass and the provider for the used dosimeters at CERN was done after LS1 in 2014. As can be seen in Tab. 7.6 especially the Silver content decreased with the new dosimeters, which may have an impact on the response function of those dosimeters. For this particular type of glass not much reference was found in the literature, therefore additional tests were conducted at the CERN ⁶⁰Co facility (detailed information can be found at *Database of irradiation facilities at CERN* accessed 11.03.2018) to understand the behavior of these particular RPL dosimeters better.

Tab. 7.6.: Composition and provider of the used RPL dosimeter at CHARM. After LS1 the Schott DOS 2-type ones were replaced with the Chiyoda Techno Glass Corporation FD-7 ones.

Name	Composition [wt%]					
	Ag	Al	Li	P	O	Other
Chiyoda Techno Glass Corporation FD-7	0.17	6.1	-	31.5	51.2	11.0 Na
Schott (DOS 2 type)	3.7	4.6	3.7	33.4	53.7	0.9 B

To main questions of interest were, if the RPL dosimeter show a dose rate dependency if the fading and/or buildup effect is prominent and has to be considered for future campaigns and to get a feeling of the spread within the total absorbed dose for one batch of dosimeters. The reader has to consider that the CERN ⁶⁰Co facility is not a proper calibration campaign, therefore the results cannot be interpreted as a necessary benchmarking of the new RPL types.

Dose rate dependency

For the dose rate dependency testing, 6 disks were chosen that contained 10 RPL each. Those containers were placed at various distances from the source, removing them at different times to obtain a constant total dose for all of them. With no dose rate dependency, the collected total dose should be the same for all the dosimeters, independent from the dose rate.

Before each irradiation, a calibration with an ionization chamber was conducted, whereas 10 individual measurements were performed, each for an irradiation duration of 10 seconds. The average value and standard deviation were calculated and used as calibration value plus the uncertainty for the position. This experimental calibration result was further used to calculate the irradiation time to achieve a total accumulated dose of 100 Gy for the specific position.

After the irradiation, the RPL dosimeters were read and the average absorbed dose of the 10 dosimeters within one disk was compared with the results given by the irradiation chamber for the specific distance. Furthermore, the standard deviation of the 10 individual dosimeters within one disk was calculated, to see if the uncertainty of 5% within a gamma field is comparable with the spread of the results that were obtained. Tab. 7.7 shows the results of this campaign.

Tab. 7.7.: Results from the dose rate dependency campaign at the ^{60}Co facility. The uncertainty of the dose rate is given by the standard deviation of the calibration prior each measurement. The uncertainty for the accumulated dose of the FD-7 RPL are the 5 % assumed for the gamma field. The results of the FD-7 RPL are compared with the ones achieved by the calibration with the Ionization Chamber (IC).

Distance [cm]	Doserate [Gy/h]	avg. dose [Gy]	Std.dev[%]	RPL/IC
20	50.35 ± 1.05	135 ± 7	2.2	1.35
30	28.9 ± 0.4	146 ± 7	4.4	1.46
50	9.73 ± 0.14	140 ± 7	3.3	1.40
60	7.25 ± 0.07	117 ± 6	3.6	1.17
100	2.50 ± 0.03	123 ± 6	2.0	1.23
150	1.10 ± 0.02	122 ± 6	2.7	1.22

It can be seen that for all distances the RPL dosimeters are collecting a higher dose, compared to the ionization chamber. Especially positions close to the source, where a high dose rate is present, are overestimating more. Fig 7.13 shows the achieved results plotted. A visible step function is visible, where the first three results are within the uncertainty of each other, and the latter three. Based on this first measurements it seems that there is a dependency on the dose rate, that has to be investigated further in a suitable calibration campaign.

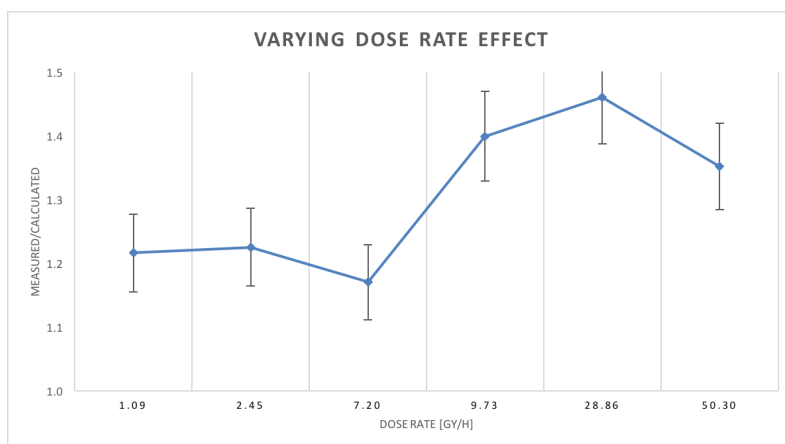


Fig. 7.13.: Plotted ratio between accumulated dose read from the RPL dosimeters and calculated one based on a calibration with the ionization chamber. A clear step within the results can be seen for the region between 7 - 9 Gy/h.

Fading and Buildup effect

For an analysis of the potential fading or buildup effect that may occur within CERN applications, 6 disks containing 10 RPL each, were placed at the same distance from the source, for the same time period. To guarantee an homogeneous field the distance was chosen to be ~ 160 cm. After irradiating the RPL for around ~ 3 days, the readout of the accumulated dose happened in different time steps. The first batch was read after one day, followed by another patch for each week. The average dose of the 10 RPLs within the first disk, that was measured after 1 day, was taken as a reference value for all the other measurements.

Tab. 7.8 reports the results of this campaign. As can be seen all accumulated dose values, for the chosen time period, are within the RPL calibration uncertainty of 5% in a pure gamma field. As already shown in Fig. 3.2, the buildup effect depends strongly on the Silver content present within the glass. The Silver content decreased from the old dosimeters and the new ones (Tab. 7.6) and therefore with lower absolute values, a smaller buildup effect can be seen. As for the fading effect, RPL dosimeters used for this kind of experiments, are usually read out within small time periods of a few weeks. Within this duration, no fading effect was visible according to the presented results. In conclusion, the buildup or fading effect is therefore negligible for the RPL dosimeter used within CERN for the waiting periods up to 49 days between irradiation and measurement.

Tab. 7.8.: Results from the build-up and fading effect measurements for the RPL dosimeters. The average dose is taken from 10 individual RPL measurements, the uncertainty of the accumulated dose is given by the 5% assured for the gamma field. The first read average dose is taken as a reference for the other measurements.

time [d]	avg. dose [Gy]	Std.dev[%]	avg.dose/reference
1	101 ± 5	2.7	1.00
7	99 ± 5	2.7	0.99
14	108 ± 5	4.9	1.07
21	105 ± 5	3.5	1.04
28	103 ± 5	3.2	1.03
49	104 ± 5	3.6	1.04

Additionally, those measurements showed again, that the uncertainty of 5% for $1-\sigma$ is valid for the RPL dosimeters in a gamma field.

The next step for the calibration of the RPL dosimeter would be to invest if there is a sensitivity to other particles and how the response function of those dosimeters would look like in other particle fields, similar to what has already been done for the RadFET dosimeters and a proton source by Spiezia et al., 2014. Indeed, the systematic difference found between the RPL and RadFET dosimeter in the downstream positions, but not for the lateral ones, underlines the assumption that there might be a sensitivity

to specific particles or energy ranges. A proper calibration is, therefore, necessary to obtain satisfactory results for the regular use of those dosimeters in terms of environmental dosimetry for experimental facilities.

7.2 HEH Fluence Gradient Assessment

The High Energy Hadron fluence was measured with the SRAM memories of the RadMON v6 system, that has already been explained in Chapter 3.2. As pointed out in this chapter, the RadMON v5 system was equipped with four 4Mbit SRAM memories from Toshiba, whereas the new v6 version contains additionally four 8Mbit Cypress memories, that are not sensitive to thermal neutrons. The main advantage of the new version is to measure the contribution of the thermal neutrons to the total fluence and the HEH fluence at the same time, with the two different memory banks. Furthermore, it is possible to score for two quantities within FLUKA: The HEH fluence and the HEHeq one, that also takes the contribution of the intermediate neutrons into account, as already explained in the section 2.2.3.

Within this chapter, the results for the HEH fluence for the locations within the facility and a possible gradient effect within the test positions will be highlighted. Furthermore, a comparison between experimental values and two FLUKA quantities, HEH and HEHeq, will be presented.

7.2.1 Results R11

The RadMON systems were mounted only on some of the 9 positions on the rack, namely 2,4,5,6,8 and 9. Furthermore, due to malfunctions, data are not available for all of them. The position R11 is placed downstream of the target and is in-beam, which results in a hard spectrum with a strong contribution of HEH.

The experimental results and the comparison with FLUKA for both quantities can be seen in Tab. 7.9. The statistical uncertainty given by FLUKA is not more than 2 % for both quantities, with the average being around ~ 1.5 %. For the center of the rack, a horizontal gradient effect is visible, both from the experimental and the simulation point of view, that reaches a factor of ~ 7 at beam height. For the top and bottom part, no horizontal gradient for the HEH fluence is detectable. A vertical gradient is present between the center and the top and bottom part of the rack, with the peak at a factor of ~ 3 .

As already seen for the dose, the rack is in-beam and the impact of this beam is clearly visible on the HEH fluence variation for the center of the rack. Fig. 7.14 shows the HEH fluence distribution for three heights on the rack and the comparison with the experimental data. Furthermore, for the center, the influence of the beam is clearly visible with a peak in the fluence, in the region where the rack is in-beam. For the simulation data the HEH fluence was plotted, since a better agreement was achieved.

The comparison between the FLUKA HEH and the experimental data are overall within the uncertainty and show a good agreement, with the exception of the RM4

Tab. 7.9.: High Energy Hadron fluence measured in R11 and comparison with FLUKA simulation. A total of $2.40E+14$ POT were collected during the experimental measurements. The experimental results were collected with the RadMON system.

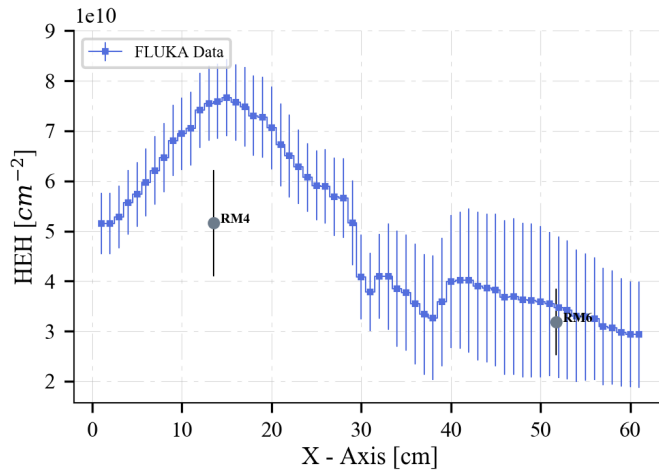
Pos.	RadMON [$10^{10}/(\text{cm}^2)$]	FLUKA HEH/RadMON	FLUKA HEHeq/RadMON
2	2.5 ± 0.5	0.85 ± 0.17	0.93 ± 0.19
4	5.16 ± 0.10	1.5 ± 0.3	1.5 ± 0.3
5	n/a	n/a	n/a
6	3.2 ± 0.6	1.0 ± 0.2	1.1 ± 0.2
8	2.5 ± 0.5	0.72 ± 0.14	0.80 ± 0.16
9	1.7 ± 0.3	1.4 ± 0.3	1.6 ± 0.3

value. This offset between the two data sets for this particular position has already been seen for the dose gradient assessment and is probably linked with the beam center at this position. For the HEH values, a weighted average ratio of 0.95 ± 0.09 between experimental and simulation data was achieved. The comparison with HEHeq gives a weighted average ratio of 1.03 ± 0.10 . Moreover, it is visible that the two quantities for this position give both satisfactory and similar results for the comparison with the experimental data, but this behavior changes for positions that are dominated by neutrons, for example, R1.

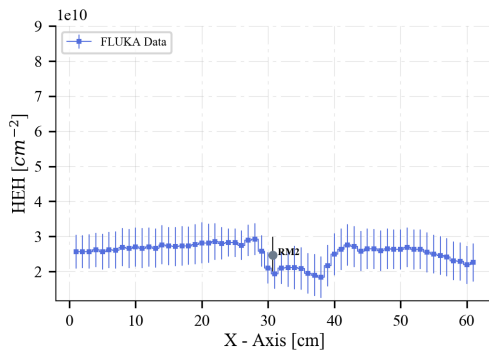
Additionally, from Fig. 7.14 it is visible that a decrease of the fluence for all the heights on the rack is noticeable for the area $30 \text{ cm} < x < 40 \text{ cm}$. This reduction can be explained if one considers the geometry of the facility: the shielding present in the irradiation room has a shielding grid surrounding it, including some poles. One of those poles causes a shadow effect on the position R11, even when the shielding is not inserted. With the full shielding configuration, this shadowing effect increases and a vertical gradient effect for the full rack width has to be considered for the position R11.

Fig. 7.15 shows the influence and shadow produced by the shielding throughout the facility. Even though the decrease of the fluence is most prominent for the lateral positions, also the region where the test position R11 is located, is affected to some extent.

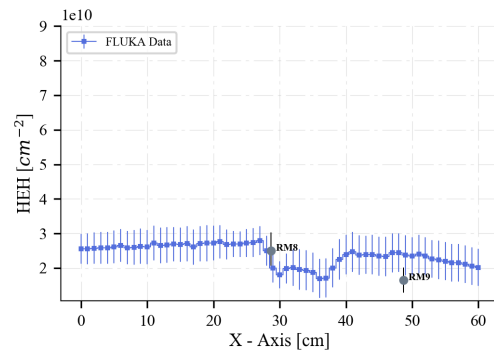
Additionally, Fig. 7.16 shows again the HEH fluence distribution along for the full rack width at two heights, that are only 7 cm apart. It is clearly visible, that at beam height the HEH fluence reaches a peak and the vertical gradient effect goes up to a factor of ~ 7 for a very small area. In reality, this means that this position should be avoided since this hard radiation condition leads to an inhomogeneous radiation field that effects components and system. Furthermore, a destruction of the equipment may be possible.



(a) Center of the rack position R11

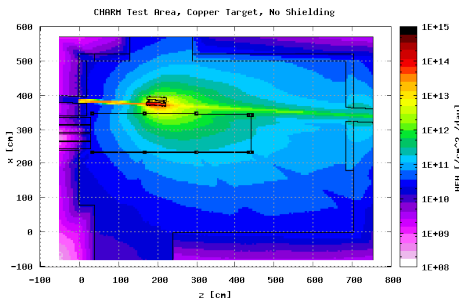


(b) Top of the rack position R11

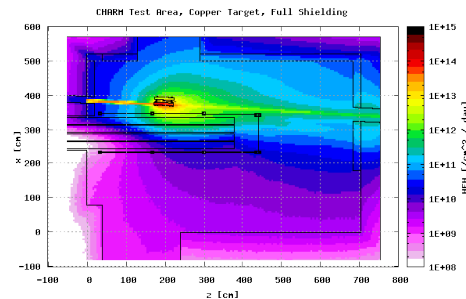


(c) Bottom of the rack position R11

Fig. 7.14.: FLUKA simulation for the HEH fluence for the rack position R11 and comparison with the experimental values. A total of $2.40E+14$ POT were collected during this run.



(a) HEH distribution in the CHARM facility for copper target and no shielding.



(b) HEH distribution in the CHARM facility for copper target and full shielding.

Fig. 7.15.: Differences for the HEH field for the CHARM facility based on the shielding configuration made from FLUKA simulations. A visible shadow, due to the insertion of the full shielding, can be seen downstream and lateral of the target. The influence of the lateral position is the strongest, where a drop of a factor ~ 10 for the HEH fluence can be seen. But also downstream positions are affected, as can be seen at the height of the shielding layers.

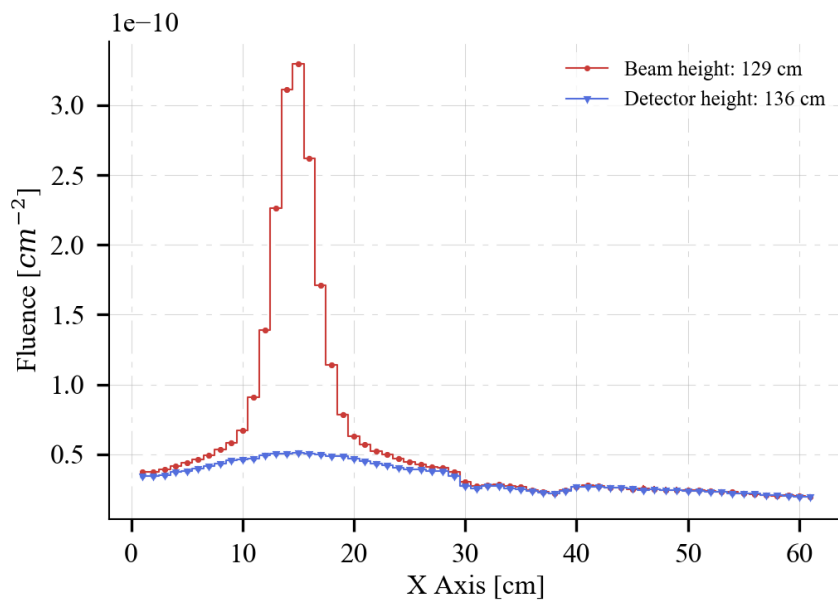


Fig. 7.16.: High Energy Hadron fluence distribution for the full rack length at beam height and detector height for the position R11. The maximum of the gradient effect reaches a factor of ~ 7 for the beam height. This result is comparable to the one for the dose, which concludes that the dose at this position is mainly produced by High Energy Hadrons.

7.2.2 Results R13

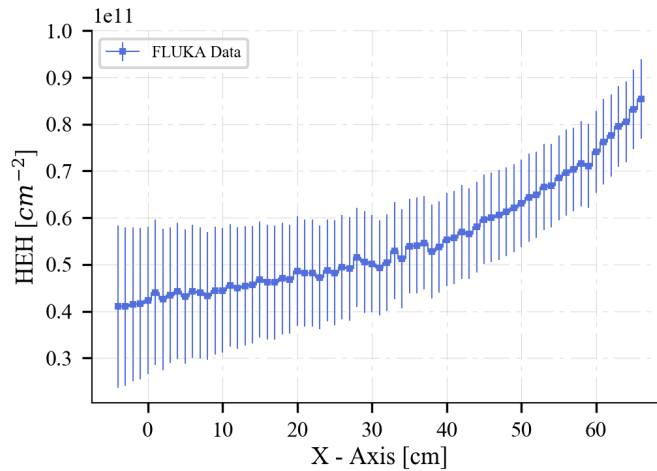
The direct comparison between FLUKA and experimental values is not possible to the already explained problems with the beam alignment. The individual results can be found in Tab. 7.10. The Monte Carlo statistical uncertainty is satisfactory with no more than 2% for the full rack and on average $\sim 1.5\%$ for both quantities. FLUKA results show that for the center of the rack an increase in the fluence for the ongoing x-direction can be found. The resulting horizontal gradient effect reaches a factor of ~ 1.5 for the full rack width and can be explained by the beam that passes the rack at this position. The top and bottom parts of the rack are not affected by this horizontal gradient effect. The HEH fluence distribution given by FLUKA can be seen in the Fig. 7.17.

Additionally, the experimental values confirm this pattern and only for the center of the rack a horizontal gradient effect can be seen, with a factor of ~ 1.8 for full rack width.

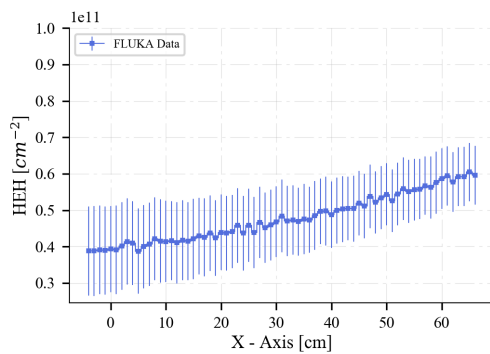
Tab. 7.10.: High Energy Hadron fluence measured in R13 and with FLUKA simulation. A total of $5.94\text{E}+14$ POT were collected during the experimental measurements. The experimental results were collected with the RadMON system.

Pos.	RadMON [$10^{10}/(\text{cm}^2)$]	HEH[$10^{10}/(\text{cm}^2)$]	HEHeq[$10^{10}/(\text{cm}^2)$]
2	1.6 ± 0.3	4.73 ± 0.07	5.35 ± 0.07
4	1.8 ± 0.4	4.33 ± 0.07	4.92 ± 0.07
5	1.9 ± 0.4	5.46 ± 0.08	6.07 ± 0.08
6	3.3 ± 0.7	6.85 ± 0.09	7.47 ± 0.09
8	1.7 ± 0.3	4.46 ± 0.07	5.08 ± 0.07
9	1.4 ± 0.3	5.23 ± 0.07	5.89 ± 0.07

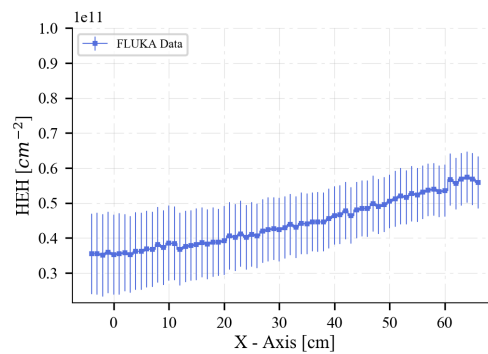
The comparison of the HEH and HEHeq values show again that they are similar for the R13 position, due to the small contribution of the intermediate neutrons here. The weighted average ratio for the both values cannot be given due to the beam misalignment.



(a) Center of the rack position R13



(b) Top of the rack position R13



(c) Bottom of the rack position R13

Fig. 7.17.: FLUKA simulation for the HEH fluence for the rack position R13. A total of $6.87E+14$ POT were collected during this run.

7.2.3 Results R1

Due to the strong influence of the shielding configuration on this position, two measurement campaigns were run. Furthermore, a comparison between the two FLUKA quantities, HEH and HEHeq, will be given for the results of this campaign and a comparison with results of past campaigns will be presented.

No shielding

As has already been seen for the dose gradient assessment, with respect to the uncertainty, neither a horizontal nor vertical gradient effect for the HEH fluence can be seen for the test position R1 with no shielding. Tab. 7.11 reports the results from the experimental measurements and the comparison with the HEH and HEHeq values. The statistical Monte Carlo uncertainty is given with $\sim 2.5\%$ on average, both for HEH and HEHeq values. As can be seen, a clear difference between the two FLUKA qualities

is visible for this position, due to the higher neutron contribution to the total particle spectra. The weighted average ratio between HEH values and the experimental ones is given with 0.90 ± 0.08 , whereas the HEHeq one gives 1.57 ± 0.13 . One has to point out that during this campaign the RadMON v6 system was used, and the Cypress SRAM memories bank was selected to measure the HEH fluence.

Tab. 7.11.: High Energy Hadron fluence measured in R1 with no shielding and comparison with FLUKA simulation. A total of $2.32E+14$ POT were collected during the experimental measurements. The experimental results were collected with the RadMON system.

Pos.	RadMON [$10^9/(\text{cm}^2)$]	FLUKA HEH/RadMON	FLUKA HEHeq/RadMON
2	5.85 ± 1.17	0.92 ± 0.19	1.6 ± 0.3
4	6.6 ± 1.3	1.1 ± 0.2	1.9 ± 0.4
5	6.5 ± 1.3	0.93 ± 0.19	1.6 ± 0.3
6	6.8 ± 1.4	0.78 ± 0.16	1.4 ± 0.3
8	7.5 ± 1.5	0.77 ± 0.15	1.3 ± 0.3
9	4.0 ± 0.8	1.3 ± 0.2	2.2 ± 0.4

Even though the HEH FLUKA values agree better with the experimental values for this campaign, the comparison between experimental and simulation data from past campaigns shows for the RadMON v5 version a better agreement was achieved with the HEHeq values. Bonaldo, 2016 reports an experimental k HEH value² for the position R1 with no shielding of $3.03E-5$, whereas Infantino, 2017 reports a k HEH value of $1.98E-5$ and k HEHeq value of $3.41E-5$. The difference in the experimental values over time cannot be explained and is most probably linked to wrong measurement. To investigate this issue further, additional experimental measurements at the position R1 are planned, to get gain more data. The FLUKA/RadMON ratios for that example result in 0.65 and 1.13 for the HEH and HEHeq values, in that order. In fact, the HEHeq take the response function of the Toshiba memories into consideration within FLUKA, which explains the better agreement with the old RadMON version. The new RadMON version, on the other hand, measures the HEH fluence generally with the Cypress memories and therefore the included weighting function of the Toshiba memories for the HEHeq quantity is unpurposed. Based on the used SRAM memories, the resulting Weibull function and the behavior of intermediate neutrons will change. To evaluate the impact of the SRAM feature size on the intermediate energy neutron response, Fig. 7.18 shows the normalized cross section for the Atmel memory with those measure for a Toshiba ($0.4 \mu\text{m}$ feature size, reference TC554001AF-70L) and Cypress memory (90 nm feature size, reference CY62157EV). The latter two are used in the current RadMON system. It can be seen that the responses are qualitatively very similar but visibly differ among the different components. Alía et al., 2017

²To compare the quantities of interest, they are usually normalized by the POT numbers. Those normalized quantities get the additional prefix "k", to underline the normalization per POT.

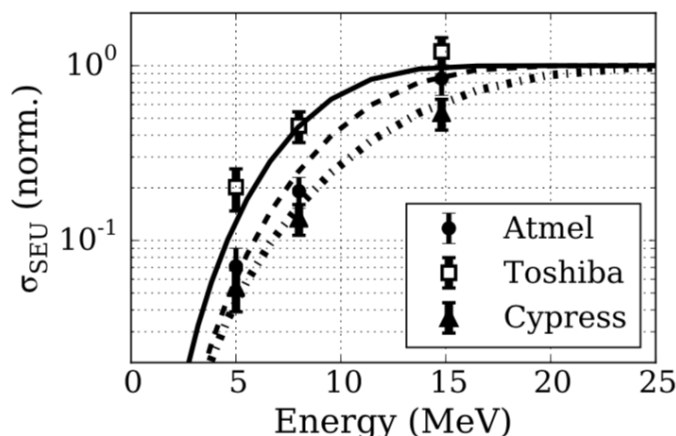


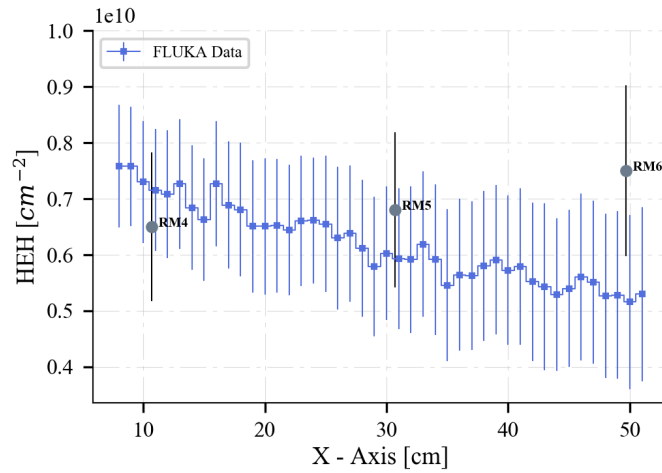
Fig. 7.18.: Normalized neutron cross-section data from the PTB Neutron Reference Fields (PIAF) together with the fitted Weibull response function for the Atmel, Cypress, and Toshiba memories. (Alfía et al., 2017)

In conclusion, different SRAM memories show different responses to the intermediate energy neutrons, that contribute the HEH fluence. The response of the Toshiba SRAM memories was considered for the HEHeq scoring quantity within FLUKA and resulted in good agreement with the experimental values for past campaigns, where the old RadMON version (v5) was used. The new RadMON version (v6) measures the HEH fluence with the Cypress memories, and better agreements with the HEH values were found during this measurement campaign. It is important to consider the responses of the used detectors for future campaigns and for the comparison with FLUKA.

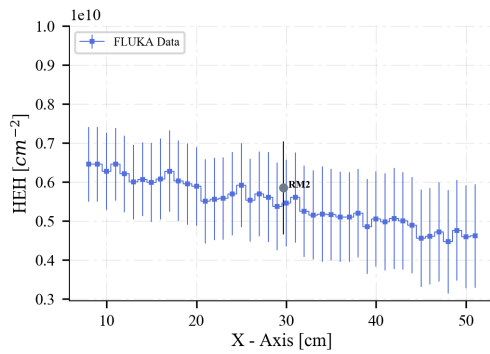
Finally, Fig. 7.19 shows the comparison between experimental and simulation values for the three heights on the rack. Since a better agreement with the HEH values was achieved, those were chosen to be plotted as FLUKA values.

Full shielding

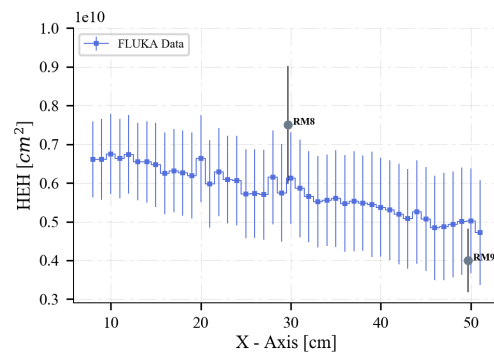
Tab. 7.12 reports the results for the full shielding configuration. The statistical uncertainty for the FLUKA data is below 15 % for both quantities, with the average being around 10%. Additionally, no horizontal or vertical gradient can be seen, neither experimentally nor from FLUKA. Furthermore, the agreement between the FLUKA HEH values and the experimental ones are highly satisfactory with a weighted average ratio of 1.10 ± 0.10 . The HEHeq values, on the other hand, show a bigger disagreement. The weighted average ratio for this case is 1.66 ± 0.15 . This shows again that the new Cypress memories used in the RadMON system are less sensitive to intermediate neutrons than the Toshiba ones and a better agreement with FLUKA is achieved if one compares it with the HEH values. Due to the lateral position and the full shielding



(a) Center of the rack position R1, no shielding



(b) Top of the rack position R1, no shielding



(c) Bottom of the rack position R1, no shielding

Fig. 7.19.: FLUKA simulation for the HEH fluence for the rack position R1 with no shielding and comparison with the experimental values. A total of $2.32E+14$ POT were collected.

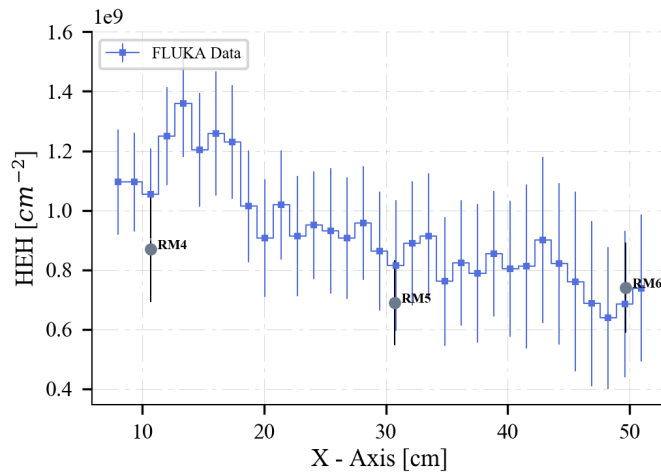
configuration, the highest thermal and intermediate neutron fluence is present in this configuration and therefore the biggest discrepancy for the two FLUKA quantities is visible. Indeed, as has already been shown, for the downstream positions like R11 the values are almost identical.

A comparison with the experimental values reported in prior test campaigns shows higher values. As reported in Bonaldo, 2016 a k HEH fluence of $1.58E-6$ was found in a campaign conducted in 2016, where the Toshiba memories were used as detectors. During this campaign, an experimental value of $1.00E-6$ was found for the center of the rack, measured with the Cypress memories. The difference shows again the possible impact of the intermediate neutrons on the detectors, with a higher sensitivity given by the Toshiba ones. Additionally, Infantino, 2017 reports a k HEH value of $1.34E-6$ and a k HEHeq value of $1.97E-6$ for this position. Again, it can be seen that a better agreement with the HEH values, given by FLUKA, can be achieved.

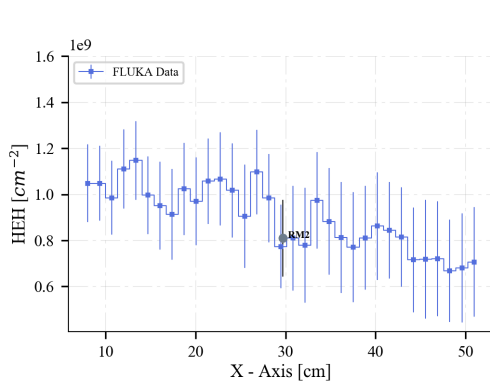
Tab. 7.12.: High Energy Hadron fluence measured in R1 with full shielding and comparison with FLUKA simulation. A total of 6.87E+14 POT were collected during the experimental measurements. The experimental results were collected with the RadMON system.

Pos.	RadMON [$10^8/(\text{cm}^2)$]	FLUKA HEH/RadMON	FLUKA HEHeq/RadMON
2	8.1 ± 1.6	0.95 ± 0.22	1.9 ± 0.4
4	8.7 ± 1.8	1.3 ± 0.3	1.8 ± 0.4
5	6.9 ± 1.4	1.2 ± 0.3	1.8 ± 0.4
6	7.4 ± 1.5	0.9 ± 0.2	1.3 ± 0.3
8	7.5 ± 1.5	1.1 ± 0.3	1.6 ± 0.3
9	3.6 ± 0.7	1.6 ± 0.4	2.0 ± 0.5

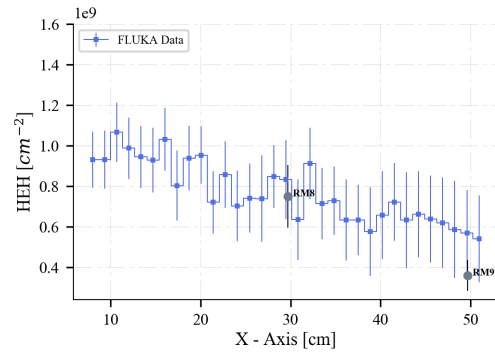
Fig. 7.20 shows the comparison between FLUKA and experimental values for the three heights on the rack. Due to the better agreement with the FLUKA HEH values, those were chosen as representative FLUKA results.



(a) Center of the rack position R1, full shielding



(b) Top of the rack position R1, full shielding



(c) Bottom of the rack position R1, full shielding

Fig. 7.20.: FLUKA simulation for the HEH fluence for the rack position R1 with full shielding and comparison with the experimental values. A total of $6.87\text{E}+14$ POT were collected.

7.3 1 MeV Neutron Equivalent Fluence Assessment

The 1 MeV neutron equivalent fluence is another important quantity in the R2E context to quantify displacement damage. As mentioned in Chapter 3, it is measured by means of p-i-n diodes, which are implemented in the RadMON system. The following chapter will present the results of the 1 MeV neutron equivalent fluence gradient for the test positions in question at CHARM.

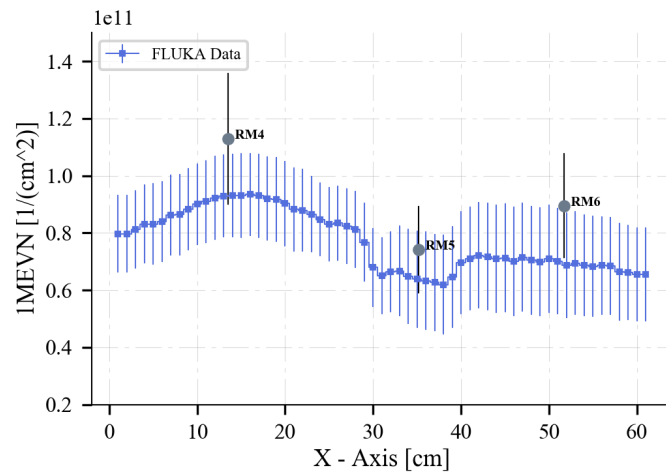
7.3.1 R11

Tab. 7.13 reports the experimental and simulation data for the 1 MeV neutron equivalent fluence on the rack position R11. The statistical uncertainty given by FLUKA is on average around 1% for this position. As can be seen from the experimental values, there is a minor horizontal gradient visible, that is outside of the uncertainty, given by the RadMON system for the center of the rack. The FLUKA data shows that due to the shadow effect of the shielding grid, the right part of the rack receive a lower fluence. Furthermore, due to the in-beam position of R11 a small region on the left part of the rack receives a higher fluence. The combination of those two effects leads to this minor horizontal gradient effect for the full rack width. The top and bottom parts of the rack are only affected by the shadow effect. Fig. 7.21 shows the

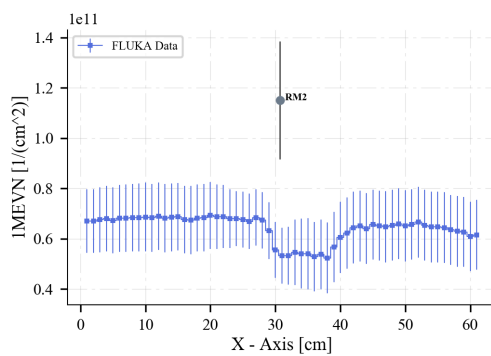
Tab. 7.13.: 1MeV neutron equivalent fluence measured in R11 and comparison with FLUKA simulation. A total of 2.40E+14 POT were collected during the experimental measurements. The experimental results were collected with the RadMON system.

Pos.	RadMON [10^{10} neutrons/(cm ²)]	FLUKA/RadMON
2	11.5 ± 2.3	0.48 ± 0.10
4	11.3 ± 2.3	0.83 ± 0.17
5	7.42 ± 1.48	0.83 ± 0.17
6	8.95 ± 1.79	0.77 ± 0.15
8	4.39 ± 0.88	1.18 ± 0.23
9	3.53 ± 0.71	1.8 ± 0.3

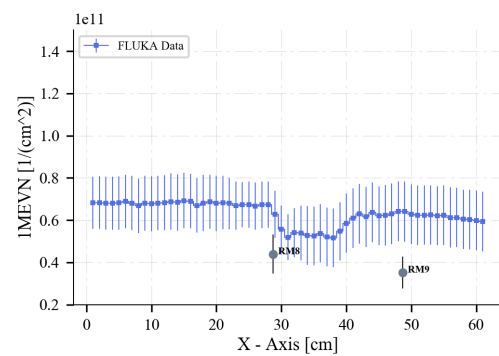
comparison between FLUKA and and experimental data for the three heights on the rack. The shadow effect due to the shielding grid is visible in the area $30 \text{ cm} < x < 40 \text{ cm}$. Overall the agreement between experimental and simulation values is satisfactory, with a weighted average ratio FLUKA/RadMON of 0.72 ± 0.06 . Furthermore it can be seen that the agreement is better for the center of the rack, compared to the top and bottom parts.



(a) Center of the rack position R11



(b) Top of the rack position R11



(c) Bottom of the rack position R11

Fig. 7.21.: FLUKA simulation for the 1MeV Neutron fluence for the rack position R11 and comparison with the experimental values. A total number of 2.32E+14 POT were collected.

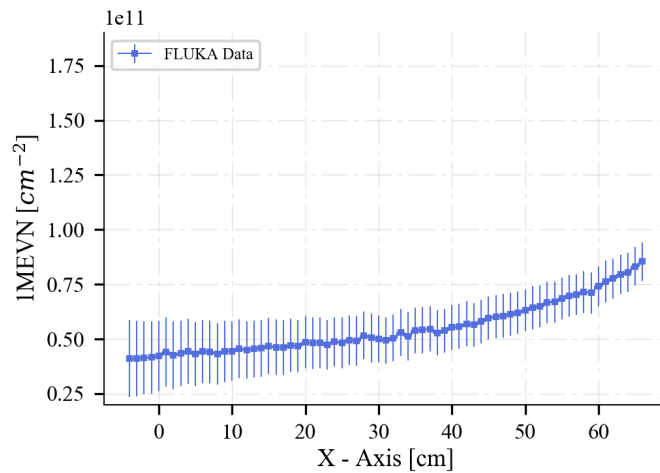
7.3.2 R13

Due to the beam misalignment, a direct comparison between simulation and experimental data is not possible. However, the two datasets will be analyzed separately. Tab. 7.14 reports the experimental and FLUKA values individually. The simulation data shows a gradient effect of a factor ~ 1.5 for the center of the rack, with an increasing value for an ongoing x. This is explicable due to the beam passing on this side of the rack. The top and bottom parts do not show a gradient outside of the uncertainty. Furthermore, it is visible that the 1 MeV neutron equivalent fluence is stronger in absolute terms for the top and center heights on the rack. The vertical gradient effect between the three heights is within a factor of ~ 3 . The experimental data shows a horizontal gradient for the bottom row of a factor of ~ 2 and another one for the center. One has to consider though that those values cannot be interpreted as the norm for the facility, due to the beam offset.

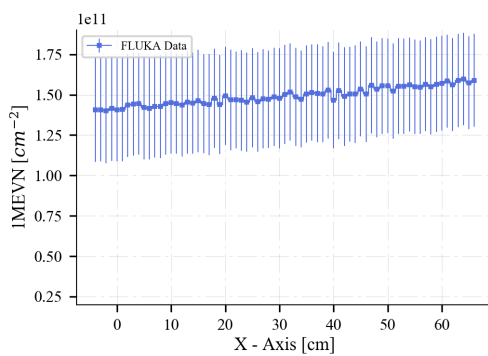
Tab. 7.14.: 1MeV neutron equivalent fluence measured in R13 and comparison with FLUKA simulation. A total of 6.87E+14 POT were collected during the experimental measurements. The experimental results were collected with the RadMON system.

Pos.	RadMON [$10^{10}/(\text{cm}^2)$]	FLUKA [$10^{10}/(\text{cm}^2)$]
2	8.2 ± 1.6	15 ± 3
4	6.6 ± 1.3	4.3 ± 0.8
5	9.9 ± 2.0	5.5 ± 1.1
6	6.3 ± 1.2	6.9 ± 1.3
8	7.3 ± 1.5	14 ± 3
9	3.6 ± 0.7	15 ± 3

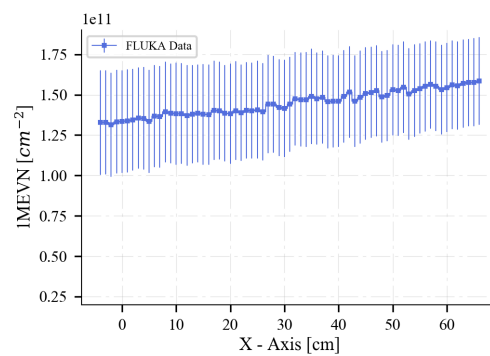
Fig. 7.22 shows the FLUKA data plotted for the three heights of the rack. It is clearly visible that there is a vertical gradient between the center and the top and bottom part. Furthermore the horizontal gradient effect for the center of the rack is visible as well.



(a) Center of the rack position R13



(b) Top of the rack position R13



(c) Bottom of the rack position R13

Fig. 7.22.: FLUKA simulation for the 1MeV Neutron fluence for the rack position R13 and comparison with the experimental values. Our comparison is a bit off since problems with the beam alignment were present. A total number of $5.94\text{E}+14$ POT were collected.

7.3.3 R1

As already seen before for the dose and the HEH fluence, this position was irradiated twice with two different shielding configurations. The results for both cases will be presented within this section.

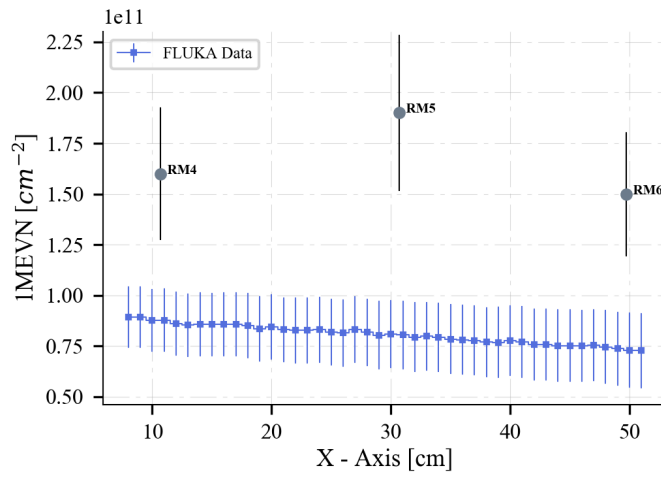
No Shielding

Tab. 7.15 reports the experimental data and the comparison with FLUKA. As can be seen from there, the comparison FLUKA/RadFET shows a weighted average ratio of 0.46 ± 0.04 , which is worse than the other two quantities at this position (namely dose and HEH fluence). Furthermore, the comparison with the downstream position R11 shows that a better agreement was achieved there. As already seen for the

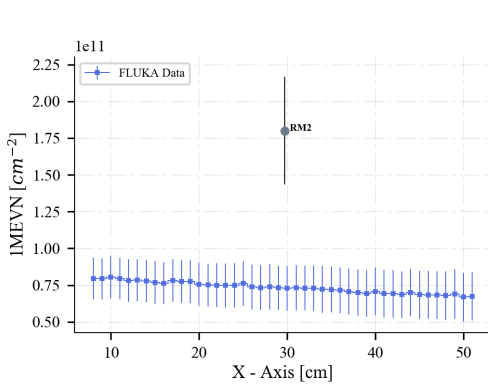
Tab. 7.15.: 1MeV neutron equivalent fluence measured in R1 with no shielding and comparison with FLUKA simulation. A total of 2.40E+14 POT were collected during the experimental measurements. The experimental results were collected with the RadMON system.

Pos.	RadFET [$10^{11}/(\text{cm}^2)$]	FLUKA/RadFET
2	1.8 ± 0.4	0.41 ± 0.08
4	1.6 ± 0.3	0.56 ± 0.11
5	1.9 ± 0.4	0.43 ± 0.09
6	1.5 ± 0.3	0.49 ± 0.10
8	1.8 ± 0.4	0.42 ± 0.08
9	1.3 ± 0.3	0.55 ± 0.11

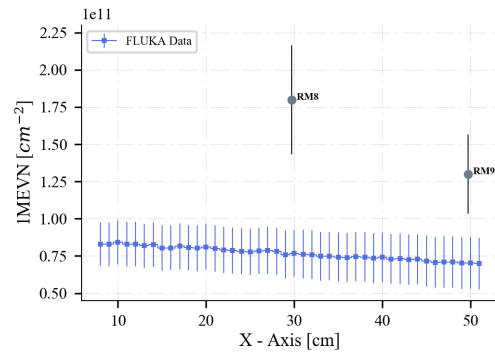
other two quantities, R1 does not show a significant horizontal or vertical gradient effect throughout the rack, for the 1 MeV neutron equivalent fluence. The graphical comparison between the FLUKA and experimental values can be seen in Fig. 7.23.



(a) Center of the rack position R1, no shielding



(b) Top of the rack position R1, no shielding



(c) Bottom of the rack position R1, no shielding

Fig. 7.23.: FLUKA simulation for the 1MeV Neutron fluence for the rack position R1 with no shielding and comparison with the experimental values.

Full shielding

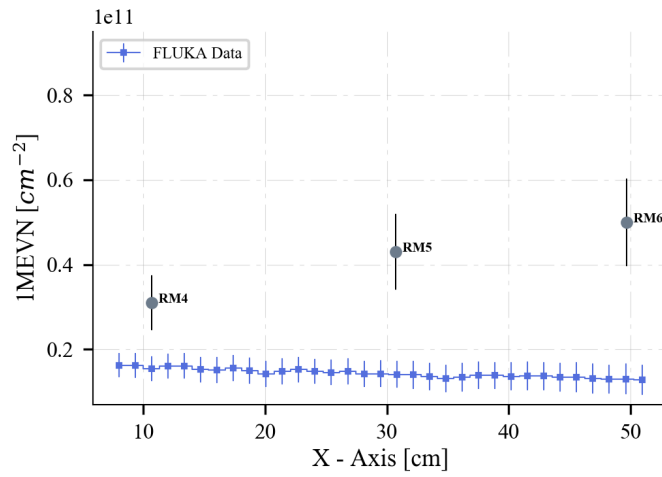
Tab. 7.16 reports the comparison between experimental and simulation data for the rack position R1, with the full shielding configuration. It is visible, that the agreement between the two data sets is worse, compared to the no shielding configuration. In fact, the weighted average ratio of FLUKA/RadMON results in 0.32 ± 0.03 . Additionally, due to problems with the detectors, no experimental data for the bottom part of the rack is available. From the presented data it can be seen that there is no horizontal gradient effect for the three heights of the rack from the FLUKA point of view. However, the detector on the top part of the rack measures a significant higher fluence, than for the center.

Tab. 7.16.: 1MeV neutron equivalent fluence measured in R1 with full shielding and comparison with FLUKA simulation. A total of $2.40E+14$ POT were collected during the experimental measurements. The experimental results were collected with the RadMON system.

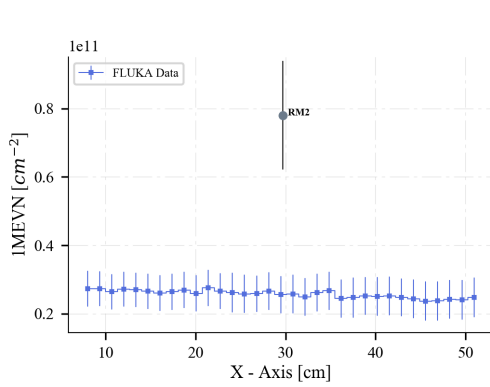
Pos.	RadFET [$10^{10}/(\text{cm}^2)$]	FLUKA/RadMON
2	7.8 ± 1.6	0.33 ± 0.07
4	3.1 ± 0.6	0.50 ± 0.10
5	4.3 ± 0.9	0.33 ± 0.07
6	5.0 ± 1.0	0.26 ± 0.05
8	n/a	n/a
9	n/a	n/a

The strong disagreement between experimental and simulation data may be linked to the already explained problems for the lateral positions, namely: different particle spectra, unknown composition of the shielding and sensitivity of the detectors to specific particles. Furthermore the discrepancy may be explained with a calibration issue. Indeed, as pointed out by Ravotti et al., 2007 a pre-irradiation of the p-i-n diodes is necessary to obtain good results.

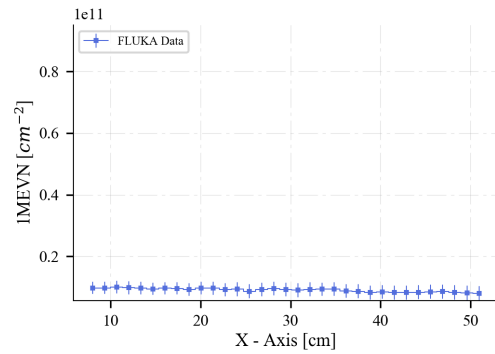
Fig. 7.24 shows the comparison between experimental and simulation data. As has already been seen for the no shielding case, the FLUKA data underestimated the experimental data for all three cases.



(a) Center of the rack position R1, full shielding



(b) Top of the rack position R1, full shielding



(c) Bottom of the rack position R1, full shielding

Fig. 7.24.: FLUKA simulation for the 1MeV Neutron fluence for the rack position R1 with full shielding and comparison with the experimental values.

Conclusion and Outlook

The CERN High energy Accelerator Mixed field/facility, CHARM, is conceived to be an irradiation facility for the qualification of large electronic systems and components in a mixed radiation field, representatives of the most common radiation environments like accelerator, ground, avionics and space. The mixed field of neutrons, protons, kaons, pions, muons, electrons, positrons, and photons is generated from the interaction of a 24 GeV/c proton beam with a copper or aluminium target. The complicated field, with its unique conditions, poses important challenges in the accurate calibration and dosimetry of the facility, which is a key point for ensuring the reliability and reproducibility of tests. Furthermore, a knowledge not only of the general radiation environment, but a more detailed understanding of the field in test locations is crucial for the goodness of test results, particularly with regard to applications, where an exact knowledge of the delivered dose or fluence is fundamental (e.g. electronic component lifetime, material science, etc.). As previous campaigns have shown, there is a radiation gradient affecting specific test positions within the facility, that has to be quantified. To analyze this gradient and to guarantee an excellent benchmarking of the facility, an experimental measurement campaign was conducted with different detectors, supported by FLUKA Monte Carlo simulation, with the specifically developed CHARM FLUKA model. This thesis presents the first evaluation of the radiation gradient effect present at CHARM.

An experimental evaluation of the Total Ionizing Dose, High Energy Hadron, and 1 MeV neutron equivalent fluence gradient in a few test locations of the CHARM facility and a comparison of the results with FLUKA simulation was reported. Four different test locations were studied: T0, a high dose rate test location close to the target revolver, R1, R11 and R13, three standard test locations for irradiation tests by means of a rack. The experimental measurements were conducted with the RadMON system, containing RadFET dosimeters, SRAM memories, and p-i-n diodes, to measure all three quantities of interest within the R2E context. Additionally, passive dosimeters in form of RPL were used. Both detector systems were presented during this thesis, including their working principles, advantages, and disadvantages. RadFET and RPL dosimeters are calibrated in a pure ^{60}Co field. For the RadFET dosimeters, the response function for protons is additionally known, whereas no knowledge for the response to other particles, besides the gamma-ray emitter, is known for the RPL case.

Regarding the test location T0, FLUKA simulation allowed a detailed study of the dose field: the simulation shows how, close to the target revolver, the dose field can vary

up to a factor ~ 3 in the beam direction, and overall up to a factor ~ 10 , considering the full table surface. The position was covered with two kinds of dosimeters, to detect a possible dose gradient: RPL and passive RadFET ones. With regard to these experimental measurements, RPL matches the Monte Carlo simulation better, compared to the RadFET sensors. Overall both family of dosimeters give an agreement within a factor 2: considering the strong dose gradient (up to 30 Gy/cm during the measurement campaign) and the limitation of this kind of dosimeters in the mixed field, the agreement with FLUKA is satisfactory. Additionally, it can be seen, that based on the distance to the target, a different agreement for the same kind of dosimeter and FLUKA is visible. Indeed, the RPL close to the target shows a weighted average ratio of 1.64 ± 0.14 for FLUKA/RPL, and the ones further resulted in a weighted average ratio of 0.90 ± 0.08 . Nevertheless, all experimental results follow the dose distribution of the FLUKA ones. To investigate the offset further, additional FLUKA simulations and experimental measurements in the ^{60}Co facility at CERN have been conducted, with the preliminary results, that the used RPL dosimeters show a dose rate dependency but no build up or fading effect.

For the test position R11, a detailed assessment of the radiation field on the surface of the rack has been conducted, showing that the actual dimensions of the rack result in areas of the rack being in-beam. This leads to a strong radiation gradient effect for the analyzed quantities: TID, HEH, and 1 MeV neutron equivalent fluence. Indeed, Monte Carlo simulation shows, how in an area of 20 cm x 10 cm from the beam spot, the dose can vary up to a factor of ~ 6 , and the HEH fluence up to a factor of ~ 7 . For the 1 MeV neutron equivalent fluence, this gradient effect cannot be seen. For the dose assessment, both kinds of dosimeters agree again overall within a factor of 2, with a better match of the RPL ones. A weighted average ratio FLUKA/dosimeter for the RPL was found of 1.02 ± 0.07 , for the RadFET one this results in 1.48 ± 0.15 . The position allows the direct comparison of the dose results of both kind of dosimeters since they were placed in the same position. A systematic difference is visible, giving the ratio RPL/RadFET of 1.47. FLUKA actually allows the assessment of the HEH fluence with two FLUKA-specific quantities: HEH and HEHeq fluence. The latter one takes the response function, especially the sensitivity to thermal neutrons, of the Toshiba SRAM memories into consideration. For the position R11 similar results have been found for the comparison between the experimental values and both FLUKA quantities, with weighted average ratios of 0.95 ± 0.09 for HEH/RadMON and 1.03 ± 0.10 for HEHeq/RadMON. This behavior changes for other position,s that are more affected by thermal and intermediate neutrons.

With regard to the test position R13, a direct comparison between FLUKA and experimental values cannot be given, due to a beam misalignment and therefore no representative conditions during the measurement period. However, the individual comparison of the results show, that R13 is affected by a horizontal gradient effect as well, but not from a vertical one, for all three quantities.

Finally, for the test position R1 two configurations were chosen: no shielding and full

shielding. Due to the lateral position of R1, the shielding configuration affects the spectra and received quantities strongly. For both cases no vertical or gradient effect was found, for all the positions and analyzed quantities on the rack.

Regarding the no shielding case: For the dose assessment, a weighted average ratio FLUKA/RadFET of 0.71 ± 0.09 was achieved. If one takes into consideration, that the FLUKA results were scored within air, the small FLUKA binning size for this campaign and the unknown response of the dosimeters in a mixed field, the offset and overturned behavior, compared to the downstream position R11, may be explained. Indeed, other campaigns have shown that a better agreement was achieved, if the actual sensitive areas of the dosimeters are build within FLUKA and the dose is scored within. A comparison between the accumulated absolute dose values for RPL and RadFET shows no difference, outside the uncertainties. This good agreement is contrary to the systematic difference that has been found for the downstream position R11. For the HEH fluence assessment, a weighted average ratio of FLUKA/HEH of 0.90 ± 0.08 and FLUKA/HEHeq 1.57 ± 0.13 was found. A better agreement with the HEH values can be seen for those lateral positions, since the current RadMON version (v6) uses Cypress SRAM memories to detect SEU caused by HEH, whereas the older version (v5) used Toshiba memories. In the past a better agreement with the HEHeq quantity was achieved. The agreement between simulation and experimental data for the the 1 MeV neutron equivalent fluence gives a weighted average ratio of 0.46 ± 0.04 . The discrepancy should be investigated further, but may be explained with calibration issues.

For the full shielding case the FLUKA/RadFET comparison results in an average weighted ratio of 0.35 ± 0.05 . Again, the already discussed problems play an important role here. Furthermore, no systematic difference in the absorbed dose for both dosimeters has been found, analogue to the no shielding case. For the HEH fluence, a similar result to the no shielding one was found as well with a weighted average ratio of FLUKA/HEH with 1.10 ± 0.10 and FLUKA/HEHeq 1.66 ± 0.15 . Again, the HEH values result in a better agreement with the experimental ones. For the 1 MeV neutron equivalent fluence a weighted average FLUKA/RadMON ratio of 0.32 ± 0.03 was found.

In conclusion, the presented work has shown that a detailed knowledge of the radiation field in test locations affected by gradient is crucial for ensuring the reliability and reproducibility of the test. Small uncertainties in the positioning of devices under test can lead to significant differences in the accumulated dose and fluences, possibly compromising the goodness of the tests itself. This is especially fundamental for lifetime tests of equipment or systems, regularly performed at the facility, that are exposed to radiation environments. An uncertainty in the delivered dose or fluences during the testing phase directly affects the performance of the devices and can lead to failure during their real-life applications, that could have been avoided with a correct testing. This results in the necessity of the detailed knowledge of the radiation field present within the facility, to avoid device failure in the long-term.

FLUKA allows the knowledge of the radiation field with a level of detail, which is impracticable and unachievable with experimental measurements alone and is, therefore, a strong help and support for the dosimetry of the facility. The newly found results have further shown, that some test positions inside the facility are further impractical or even not suitable for testing bulky equipment there. The radiation gradient is too strong, to guarantee a homogeneous field, that is needed to guarantee the same amount of the received quantities over the real dimensions of the device. Testing campaigns in the past, for example with SMA (Shape Memory Alloy) devices, that will be used for vacuum sealing for future accelerator projects at CERN, at the test position T0 have shown that the results were contradictory, with different outcome for the various samples. The newly gained knowledge, retrieved through the work of this thesis, could explain this behavior due to the strong radiation gradient present at this test position and therefore significant differences in the delivered quantities for the different samples. This thesis has shown that T0 suffers from a strong radiation gradient, due to the short distance to the target, that makes a collection of high dose and fluence levels in a short time frame possible on the one hand, but on the other hand the radiation field is too inhomogeneous and the gradient too prominent, to be neglected. Therefore the testing of bulky equipment or different samples spread among this position is not possible. R11 is in beam, which means that certain areas of the rack receive high levels of dose and fluences, whereas others do not. Especially the center of the rack endures this effect and should be avoided, to guarantee a homogeneous distribution of the radiation quantities. Additionally, the in beam position can lead to device destruction, if not considered. To avoid those effects, the testing of (bulky) equipment would be preferred in positions, that do not suffer from an inhomogeneous field (e.g. R1, R13 ...). For each experiment, the advantages and disadvantages of placing systems and devices at specific positions within the facility have to be considered and agreed on.

Outlook

The validated approach of simulation and measurement benchmarking will be used in future campaigns to investigate other positions within the facility: Especially the repetition of the campaign for R13, and the extension for the position R10 is planned. Those two positions are the most preferred ones in the facility for the testing campaigns, therefore a detailed knowledge of the radiation field and possible gradients, that have to be considered, are mandatory. Additionally, new campaigns and experiments are in planning, to better understand the response of the used experimental detectors within the complicated radiation conditions, that are present within CHARM. A knowledge of the response functions for specific particles, especially protons and neutrons, for the detectors is necessary for good dosimetric results. Especially the testing of the RPL

dosimeters in a proton field would be of interest, to investigate the different behaviors of the two used dosimeters for the downstream positions of the facility further. The responses for the lateral positions are comparable, but a systematic difference of $\sim 40\%$ for the positions R11 and T0 can be found. Until further campaigns have been conducted, those results have to be considered, while looking at the experimental data. Additionally, the comparison with FLUKA is always suggested.

Regarding the FLUKA simulation: Very good agreement between FLUKA and the used detectors for the downstream positions lead to the conclusion that FLUKA is a strong help and gives excellent results for the prediction of the analyzed quantities in various test positions. Additionally, the used parameters and thresholds are fine-tuned and useful for our applications. The increasing gap between the FLUKA and experimental values for the lateral positions can be explained with the FLUKA settings, that were used during this campaign. Indeed, as already pointed out during the thesis, for a better agreement and more precise knowledge of the received quantities, the sensitive volume of the detectors (or devices/systems under test) have to be simulated in those positions. Due to discrepancies in the reported experimental values at the lateral positions in the past, new experimental measurements have to be conducted and compared with the improved FLUKA simulations (simulating the sensitive regions) to make further conclusions.

Overall, the already achieved results will be used in future campaigns to exploit new test locations within CHARM and provide a strong knowledge about the irradiation conditions present for ongoing test campaigns. FLUKA is a strong help, especially for the radiation gradient assessment, due to the fact that it can cover a lot of test locations with a detail, that would not be possible with experimental measurements alone. The comparison has shown that FLUKA can predict the achieved results in a satisfactory way, and how the CHARM model can be improved. The detailed calibration of this unique facility is an ongoing process, but a lot has already been achieved and will be of great value for future testing campaigns.

Bibliography

- Alía, Rubén García, Markus Brugger, Salvatore Danzeca, Julien Mekki, and Adam Thornton (2017). „SEE cross section calibration and application to quasi-monoenergetic and spallation facilities“. In: *EPJ Web of Conferences* 153. Ed. by F. Malvagi, F. Malouch, C.M'B. Diop, J. Miss, and J.C. Trama, p. 08015 (cit. on pp. 87, 88).
- Autran, J.L. and D. Munteanu (2015). „Radiation and COTS at ground level“. In: *Microelectronics Reliability* 55.9-10, pp. 2147–2153 (cit. on p. 8).
- Becker, K. (Klaus) (1973). *Solid state dosimetry*. CRC Press, p. 334 (cit. on pp. 19, 20).
- Böhlen, T.T., F. Cerutti, M.P.W. Chin, et al. (2014). „The FLUKA Code: Developments and Challenges for High Energy and Medical Applications“. In: *Nuclear Data Sheets* 120, pp. 211–214 (cit. on p. 45).
- Bonaldo, Stefano; (2016). „CHARM - una nuova facility del CERN per test di elettronica con spettro misto di radiazione ionizzante“. PhD thesis (cit. on pp. 13, 31, 32, 87, 89).
- Brugger, M. (2012). „Radiation Damage to Electronics at the LHC“. In: *Conf.Proc.* C1205201, pp. 3734–3736 (cit. on p. 8).
- Brugger, Markus; Ruben; Garcia-Alia, Salvatore; Danzeca, et al. (2014). „Radiation Effects, Calculation Methods and Radiation Test Challenges in Accelerator Mixed Particle and Energy Environments“. In: *NSREC 2014, Short Course* (cit. on pp. 40, 42).
- CERN (2016). *CERN annual report, 2016* (cit. on pp. 1, 2).
- Database of irradiation facilities at CERN* (accessed 11.03.2018). *Irradiation facilities database* (online). <http://irradiation-facilities.web.cern.ch/> (cit. on p. 77).
- Dmitryuk, A.V., S.E. Paramzina, A.S. Perminov, N.D. Solov'eva, and N.T. Timofeev (1996). „The influence of glass composition on the properties of silver-doped radiophotoluminescent phosphate glasses“. In: *Journal of Non-Crystalline Solids* 202.1-2, pp. 173–177 (cit. on p. 20).
- Dodd, P.E. and L.W. Massengill (2003). „Basic mechanisms and modeling of single-event upset in digital microelectronics“. In: *IEEE Transactions on Nuclear Science* 50.3, pp. 583–602 (cit. on pp. 11, 16).
- Dunn, William; and J.; Kenneth Shultis (2011). *Exploring Monte Carlo Methods* (cit. on pp. 45, 46, 48).
- Fasso, A., A. Ferrari, and P. R. Sala (2009). „Radiation transport calculations and simulations“. In: *Radiation Protection Dosimetry* 137.1-2, pp. 118–133 (cit. on p. 47).

- Ferrari A., Sala P R Fasso A Ranft J (2005). „FLUKA: a multi-particle transport code“. In: *CERN 2005- 10 (2005), INFN/TC\$ _\$05/11, SLAC-R-773* (cit. on pp. 45, 49, 54).
- Fleetwood, Daniel M., Peter S. Winokur, and Paul E. Dodd (2000). „An overview of radiation effects on electronics in the space telecommunications environment“. In: *Microelectronics Reliability* 40.1, pp. 17–26 (cit. on p. 8).
- Garcia Alia, Ruben, Markus Brugger, Eamonn Daly, et al. (2017). „Simplified SEE Sensitivity Screening for COTS Components in Space“. In: *IEEE Transactions on Nuclear Science* 64.2, pp. 882–890 (cit. on p. 8).
- García Alía, Rubén (2014). „Radiation Fields in High Energy Accelerators and their impact on Single Event Effects“. PhD thesis. Universite Montpellier (cit. on pp. 2, 4, 8, 9, 13, 36, 41).
- Gatignon, L., M. Lazzaroni, M. Brugger, et al. (2015). „The East Area Upgrade - Specification and Cost Estimates“. In: (cit. on p. 33).
- Gatignon, Lau, M Brugger, and F Ravotti (2013). „Beam Properties for the East Area Irradiation Facility In The T8 Beam Line“. In: (cit. on p. 33).
- Geogebra Online Tool. Geogebra* (online). <https://www.geogebra.org/classic/geometry> (cit. on p. 12).
- Hiramatsu, K, S Yoshihashi, S Kusaka, et al. (2017). „Gamma-Ray Dose Measurement with Radio-Photoluminescence Glass Dosimeter in Mixed Radiation Field for BNCT“. In: *EPJ Web Conf.* Volume 153, p. 9 (cit. on p. 19).
- Holmes-Siedle, A. G. (Andrew Gordon) and Len. Adams (2001). *Handbook of radiation effects*. Oxford University Press, p. 614 (cit. on pp. 12, 14, 24, 25).
- Holmes-Siedle, Andrew and Leonard Adams (1986). „RADFET: A review of the use of metal-oxide-silicon devices as integrating dosimeters“. In: *International Journal of Radiation Applications and Instrumentation. Part C. Radiation Physics and Chemistry* 28.2, pp. 235–244 (cit. on pp. 24, 26).
- Hoque, Khaza Anuarul, Otmane Ait Mohamed, and Yvon Savaria (2017). „Formal analysis of SEU mitigation for early dependability and performability analysis of FPGA-based space applications“. In: *Journal of Applied Logic* 25, pp. 47–68 (cit. on p. 8).
- Infantino, A.; C.; Cangialosi, M.; Krawina, et al. (2017a). „Radiation gradient assessment at the new CERN CHARM irradiation facility“. In: *Radiation Physics and Chemistry. manuscript submitted for publication* (cit. on pp. 55, 61).
- Infantino, Angelo (2017). *FLUKA Monte Carlo Modelling of the CHARM Facility’s Test Area: Update of the Radiation Field Assessment*. Tech. rep. CERN (cit. on pp. 5, 35, 37–39, 42, 57, 87, 89).
- Infantino, Angelo, Ruben Garcia Alia, and Markus Brugger (2017b). „Monte Carlo Evaluation of Single Event Effects in a Deep-Submicron Bulk Technology: Comparison Between Atmospheric and Accelerator Environment“. In: *IEEE Transactions on Nuclear Science* 64.1, pp. 596–604 (cit. on pp. 7, 58).
- International, ASTM (2014). „Standard practice for chracterizign neutron energy fluence spectra in terms of an equivalent mono-energetic neutron fluence for radiation hardness testing of electronics“. In: *ASTM E722-14* (cit. on p. 30).
- Karacson, Matthias (2016). „Evaluation of the Radiation Environment of the LHCb Experiment“. PhD thesis. Technical University of Vienna (cit. on p. 77).

- Kramer, D, M Brugger, V Klupak, et al. (2011). „LHC RadMon SRAM Detectors Used at Different Voltages to Determine the Thermal Neutron to High Energy Hadron Fluence Ratio“. In: *IEEE Transactions on Nuclear Science* 58.3, pp. 1117–1122 (cit. on pp. 28, 29).
- Krawina, Melanie; and A.; Infantino (2018). *Radiation Gradient Assessment at the CHARM facility (CERN)*. Tech. rep. (cit. on pp. 55, 61).
- Leroy, Claude and Pier-Giorgio Rancoita (2011). *Principles of Radiation Interaction in Matter and Detection*. WORLD SCIENTIFIC (cit. on pp. 12, 14, 16).
- Marzo, M., Rubén García Alía, A. Infantino, M. Brucoli, and S. Danzeca (2017a). „Impact of neutrons on the RadFET dose response when exposed to mixed-fields“. In: *Radiation Physics and Chemistry* (cit. on pp. 72, 76).
- Marzo, Matteo, Stefano Bonaldo, Markus Brugger, et al. (2017b). „RadFET dose response in the CHARM mixed-field: FLUKA MC simulations“. In: *EPJ Nuclear Sci. Technol.* 3 24 (cit. on pp. 72, 73).
- Mekki, J., M. Brugger, R. Alia, et al. (2016). „CHARM: A Mixed Field Facility at CERN for Radiation Tests in Ground, Atmospheric, Space and Accelerator Representative Environments“. In: *IEEE T. Nucl. Sci.*, 63 (4), pp. 2106–2114 (cit. on pp. 5, 31, 41, 42, 57, 58).
- Nourreddine, A, Y O Salem, A Nachab, and C Roy (2015). „Study of a new neutron dosimeter incorporating RPL detectors“. In: *Radiation Measurements* 83, pp. 47–50 (cit. on p. 19).
- Oldham, T.R. and F.B. McLean (2003). „Total ionizing dose effects in MOS oxides and devices“. In: *IEEE Transactions on Nuclear Science* 50.3, pp. 483–499 (cit. on p. 25).
- Ravotti, F. (2017). „Dosimetry Techniques and Radiation Test Facilities for Total Ionizing Dose Testing“. In: *RADECSShort Course* (cit. on pp. 21, 24).
- Ravotti, F., M. Glaser, A. B. Rosenfeld, et al. (2007). „Radiation Monitoring in Mixed Environments at CERN: From the IRRAD6 Facility to the LHC Experiments“. In: *IEEE Transactions on Nuclear Science* 54.4, pp. 1170–1177 (cit. on pp. 30, 98).
- Roeed, Ketil, Markus Brugger, Daniel Kramer, et al. (2012). „Method for Measuring Mixed Field Radiation Levels Relevant for SEEs at the LHC“. In: *IEEE Transactions on Nuclear Science* 59.4, pp. 1040–1047 (cit. on p. 14).
- Schulman, James H., Robert J. Ginther, Clifford C. Klick, Raymond S. Alger, and Robert A. Levy (1951). „Dosimetry of X-Rays and Gamma-Rays by Radiophotoluminescence“. In: *Journal of Applied Physics* 22.12, pp. 1479–1487 (cit. on pp. 17, 20).
- Schwank, James R., Marty R. Shaneyfelt, Daniel M. Fleetwood, et al. (2008). „Radiation Effects in MOS Oxides“. In: *IEEE Transactions on Nuclear Science* 55.4, pp. 1833–1853 (cit. on pp. 16, 24, 25).
- Secondo, Raffaello (2017). „Upgrades of the RadMon V6 and its Integration on a Nanosatellite for the Analysis and the Comparative Study of the CHARM and Low Earth Orbit Environments“. PhD thesis. Universite Montpellier (cit. on pp. 22, 23).
- Spiezia, G., P. Peronnard, A. Masi, et al. (2014). „A New RadMon Version for the LHC and its Injection Lines“. In: *IEEE Trans. Nucl. Sci.* 61 (6), pp. 3424–3431 (cit. on pp. 22, 23, 26–30, 72, 79).
- Thornton, Adam (2016). „CHARM Facility Test Area Radiation Field Description“. In: *CERN-ACC-NOTE- 2016-12345* (cit. on pp. 5, 31, 32, 36, 39, 41, 42, 53, 54).

- Vincke, Helmut, Isabell Brunner, I. Floret, et al. (2007). „Response of alanine and radio-photoluminescence dosimeters to mixed high-energy radiation fields“. In: *Rad. Prot. Dos. 125 (1-4)*, pp. 340–344 (cit. on p. 76).
- Vogel, H. and K Becker (1965). „Zur Theorie der Radiophotolumineszenz in Gläsern 1.“ In: *Nukleonik 7 18* (cit. on p. 20).
- Yamamoto, Takayoshi, Anatoly Rosenfeld, Tomas Kron, Francesco d’Errico, and Marko Moscovitch (2011). „RPL Dosimetry: Principles and Applications“. In: *AIP Conference Proceedings*. Vol. 1345. 1. American Institute of Physics, pp. 217–230 (cit. on p. 18).
- Yokota, R. and H. Imagawa (1966). „Radiophotoluminescent centers in silver-activated phosphate glass“. In: *Journal of the Physical Society of Japan 23.5* (cit. on p. 20).
- Ziegler, J. F. (1996). „Terrestrial cosmic rays“. In: *IBM Journal of Research and Development 40.1*, pp. 19–39 (cit. on p. 7).

List of Figures

1.1	Overview of the CERN complex, including the the chain of the six accelerators, experiments and dimensions. The accelerators and beamlines are marked in grey, the detectors and experiments in blue. Orange symbolizes stand alone projects and facilities. (CERN, 2016).	2
1.2	Beam dumps of the LHC, due to radiation induced failures in electronic devices and systems over the years. It can be seen, that those premature dumps are significantly reduced over the years, due to the efforts from the R2E group at CERN. Figure from internal R2E report.	3
2.1	Graphical visualization of the displacement damage. An incoming particle hits a lattice atom, displacing it. The resulting vacancy and interstitial pair can lead to various degradation effects within the device. Graphics made by M.Krawina with the GeoGebra online tool. [<i>Geogebra Online Tool</i>]	12
2.2	Example of a typical cross-section curve as a function of the LET. LET_0 is equal to LET_{th} and is defined as the threshold LET. σ_{sat} is the saturation cross-section. (Leroy and Rancoita, 2011)	16
3.1	Graphical representation of the formation of luminescence centers. Due to ionization electron-hole pairs are getting created, that excite the Silver atoms within the the glass. Yamamoto et al., 2011	18
3.2	Comparison of the RPL readout intensity of different dosimeters, consisting of the same glass base but with varying silver content. The buildup effect is visible and increases with rising Silver content. (Becker, 1973) .	20
3.3	Readout function of the FD-7 RPL dosimeters calibrated in a ^{60}Co source. Each point is the average of 10 measurements. The errors are a combination of the standard deviation of the 10 measurements and the errors from the RISO irradiation. Total error values are multiplied by a factor of 5 for better visibility. Plot provided by the CERN HSE-RP group.	21
3.4	The fully assembled RadMON v6 system. Secondo, 2017	22
3.5	Functional structure of the RadMON V6. Secondo, 2017	23
3.6	Schematic function of a n-channel MOSFET illustrating radiation-induced charging of the gate oxide: a) normal operation b) post-irradiation. Figure from Oldham and McLean, 2003	25

3.7	Average response curves for the 100 nm RadFET for a ^{60}Co and proton source at two gate voltages. (Spiezia et al., 2014)	27
4.1	Facility layout of the building 157. The East Area receives a 24 GeV/c proton beam from the PS accelerator, which travels through the IRRAD facility first, before reaching CHARM (Bonaldo, 2016).	32
4.2	FLUKA CHARM model that shows the layout of the irradiation room. The target, the shielding, and the most used test positions can be seen.	33
4.3	Comparison of the radiation field within the CHARM facility for four different configurations. The influence of the shielding and target on the resulting mixed field within the facility can be seen. Two target and shielding configurations have been chosen: copper target with full and no shielding at all and the aluminium target, again with full and no shielding at all. FLUKA simulations and plots done by A. Thornton.	37
4.4	Particle spectra for different configurations and positions in the facility. The first row compares the spectra for the position R11 with no shielding, for two different target configurations: copper and aluminium. The second row compares the particle spectra for the position R1 with the copper target, for two different shielding configurations: no shielding and full shielding. FLUKA simulations done by A. Infantino, analysis and plots by M. Krawina.	39
4.5	Comparison between the reversed integral spectra for different test positions at CHARM (in grey) and different radiation environments. The values are normalized to the flux >20 MeV. Thornton, 2016	41
4.6	Comparison between the reversed integral spectra for different LHC environments with typical positions in CHARM. FLUKA simulations and plots made by A.Thornton Thornton, 2016	42
5.1	Example input card for the definition of the particle source. It describes a primary proton beam, with an energy E of 200 MeV, a momentum of Δp of 0.2 GeV/c, a beam divergence of $\Delta\phi$ of 1.5 mrad and an extent of Δx and Δy of 1.2cm and 0.7 cm respectively (Ferrari A., 2005).	49
5.2	Example input card for the definition of the particle source. It describes the same primary proton source as Fig. 5.1. The input via <code>flair</code> is simultaneously interpreted in the strict structure of the conventional input file and can be seen below.	49
5.3	Visualization of the geometry of the CHARM FLUKA model, as seen in the <code>flair</code> geometry viewer.	50
5.4	Input card for the primary source of the CHARM FLUKA model. As can be seen from the input parameters, we simulate the 24 GeV/c proton beam, as we have in real life. Screenshot was taken directly from <code>flair</code>	51

5.5	The full CHARM FLUKA model, that includes the shielding, the target revolver and more details. Screenshot taken directly from flair.	52
5.6	A more detailed look into the geometry of the CHARM FLUKA model. The focus is on the area around the target revolver and the test positions used during the measurement campaign. Screenshots taken directly from flair.	52
6.1	Layout of the CHARM irradiation room, including the test positions within. The four positions that were of main interest during the radiation gradient campaign are marked in blue.	58
6.2	The two used test setups during the measurement campaign. (a) shows the setup for T0, (b) for R1, R11 and R13. With regard to the R11 irradiation test, the red cross indicates the beam height	59
7.1	Dose contour plot for T0 from FLUKA simulation. The integrated dose per day has been calculated considering an average irradiation of 24 hours with 3 spills per Super-Cycle ($1.92E+15$ POT per day)	62
7.2	Dose distribution for the test position T0, both for variation in x- and z-coordinate. The dose is normalized by the number of primary protons interacting with the target (POT).	63
7.3	Comparison between the FLUKA and experimental-evaluated dose distribution along the z-axis (beam direction), at x-coordinates corresponding to the two rows of the RPLs, positioned on T0. a) shows the distribution for $x = 1.25$ cm, b) for the row at $x = 14$ cm. RadFET dosimeters are not reported in the plots since they were placed in another row.	64
7.4	FLUKA simulation for the dose contribution from the electromagnetic parts to the total dose. The two rows, where the actual RPL dosimeters were placed, were compared and the contribution to the total dose is $\sim 50\%$ for both of them.	66
7.5	Dose contour plot for the front face of R11 from FLUKA simulation. The total dose per day has been calculated considering an irradiation of 24 hours with 3 spills per Super-Cycle ($1.92E+15$ POT/day).	66
7.6	Comparison of the experimental data and FLUKA for the full rack length. The dose has been calculated with the appropriate irradiation time and POT factor of $2.4E+14$. A maximum of the dose can be seen at $x=15$ for the center of the rack, where the beam crosses the rack. A better agreement was achieved with the RPL dosimeters.	68
7.7	Dose distribution assessed with FLUKA simulation at the beam and detector height for the CHARM facility. The dose is normalized by the number of primary protons interacting with the target. The grey rectangle represents the rack width of the test position R11 within the facility (see Fig. 6.1).	69

7.8	FLUKA simulation for the dose contribution from the electromagnetic parts to the total dose. This figure shows the center of the rack, where a contribution around $\sim 50\%$ can be seen, with the exception of the $x \sim 15\text{cm}$ region, where the beam is impacting the rack.	69
7.9	Comparison of the two particle spectra in lethargy form for the test position R1, for different shielding configurations. The fluence is normalized by the number of primary protons interacting with the copper target (POT)	71
7.10	Comparison of the experimental and FLUKA data for the full rack length. The dose has been calculated with the appropriate irradiation time and POT factor of $2.32\text{E}14$	73
7.11	Comparison of the experimental and FLUKA data for the full rack length. The dose has been calculated with the appropriate irradiation time and POT factor of $6.87\text{E}14$	75
7.12	Comparison of the relative particle contribution to the total absorbed dose for the position R1, with and without shielding. Marzo et al., 2017a	76
7.13	Plotted ratio between accumulated dose read from the RPL dosimeters and calculated one based on a calibration with the ionization chamber. A clear step within the results can be seen for the region between 7 - 9 Gy/h.	78
7.14	FLUKA simulation for the HEH fluence for the rack position R11 and comparison with the experimental values. A total of $2.40\text{E}+14$ POT were collected during this run.	83
7.15	Differences for the HEH field for the CHARM facility based on the shielding configuration made from FLUKA simulations. A visible shadow, due to the insertion of the full shielding, can be seen downstream and lateral of the target. The influence of the lateral position is the strongest, where a drop of a factor ~ 10 for the HEH fluence can be seen. But also downstream positions are affected, as can be seen at the height of the shielding layers.	83
7.16	High Energy Hadron fluence distribution for the full rack length at beam height and detector height for the position R11. The maximum of the gradient effect reaches a factor of ~ 7 for the beam height. This result is comparable to the one for the dose, which concludes that the dose at this position is mainly produced by High Energy Hadrons.	84
7.17	FLUKA simulation for the HEH fluence for the rack position R13. A total of $6.87\text{E}+14$ POT were collected during this run.	86
7.18	Normalized neutron cross-section data from the PTB Neutron Reference Fields (PIAF) together with the fitted Weibull response function for the Atmel, Cypress, and Toshiba memories. (Alía et al., 2017)	88
7.19	FLUKA simulation for the HEH fluence for the rack position R1 with no shielding and comparison with the experimental values. A total of $2.32\text{E}+14$ POT were collected.	89

7.20	FLUKA simulation for the HEH fluence for the rack position R1 with full shielding and comparison with the experimental values. A total of $6.87E+14$ POT were collected.	91
7.21	FLUKA simulation for the 1MeV Neutron fluence for the rack position R11 and comparison with the experimental values. A total number of $2.32E+14$ POT were collected.	93
7.22	FLUKA simulation for the 1MeV Neutron fluence for the rack position R13 and comparison with the experimental values. Our comparison is a bit off since problems with the beam alignment were present. A total number of $5.94E+14$ POT were collected.	95
7.23	FLUKA simulation for the 1MeV Neutron fluence for the rack position R1 with no shielding and comparison with the experimental values.	97
7.24	FLUKA simulation for the 1MeV Neutron fluence for the rack position R1 with full shielding and comparison with the experimental values.	99
A.1	Picture taken from inside the CHARM irradiation room. In the middle of the room, the shielding cage can be seen. The shielding layers are extracted in this pictures, but are still visible as yellow and orange slacks at the end of the cage. Additionally, the marble shielding, the rail for the Montrac test positions and the marked positions for the standard test positions, as dots on the floor, are visible.	121
A.2	More detailed pictures of the Montrac test position on the rail system inside CHARM. Devices under test are mounted on the cage, that is visible in the background. The first part is the connection wagon, where the cables and connections for the devices are mounted. Regarding the target revolver, four different settings are possible: copper, aluminium, aluminium with holes and air.	121
A.3	More detailed pictures of the shielding layers inside CHARM and the rack setup for one of the standard test positions.	122
A.4	Full setup for the rack position R11. The detectors on the rack can be seen.	123
A.5	Pictures of the actual test setup on the rack position R11. It can be seen that only one RadMON system was mounted on the top, but RPL and passive RadFET dosimeters were attached on the other positions. The center hosted three RadMON systems, and on the bottom two RadMON system were mounted. Additionally, the cables connecting the RadMON systems with the patch panel are visible as well.	124
A.6	Test setup for the test position T0. It can be seen that the dosimeter (RPL and RadFET) are covering the whole table.	124

List of Tables

2.1	Different SEE phenomena that can happen in electronic components or systems. Modified table, original from Bonaldo, 2016.	13
3.1	Composition of some RPL dosimeters and their providers.	19
3.2	Influence of external parameters on the response curve of the 100 nm RadFET. Data from Spiezia et al., 2014	27
3.3	SEU cross section for thermal neutrons and 230 MeV protons for two SRAM memories. Data reported in Kramer et al., 2011; Spiezia et al., 2014	29
4.1	R2E relevant quantities defined to characterize a mixed-field radiation environment. García Alía, 2014	36
4.2	A comparison of the average values for specific quantities in typical test positions of the CHARM facility, for different configurations. An average number of 3.3E10 protons/seconds was used and the values were normalized for one day. Data from FLUKA simulation, done 2017 by A. Infantino. Infantino, 2017	38
4.3	A comparison of typical radiation environments and their describing quantities. The environmental values have been retrieved by using the QARM online tool, more information can be found in Brugger et al., 2014	40
4.4	A comparison of the HEH fluences ($> 20 \text{ MeV cm}^{-2} \text{ y}^{-1}$) for different radiation environments. Mekki et al., 2016	41
4.5	A comparison of the LHC environment and matching test positions and configurations from the CHARM facility. FLUKA data can be found in Infantino, 2017, LHC environment in Brugger et al., 2014. The HEH fluences are given in $\text{cm}^{-2} \text{ y}^{-1}$ for the LHC environment, and in $\text{cm}^{-2} \text{ d}^{-1}$ for CHARM.	42
5.1	Different estimators that are regularly used within the context of the CHARM facility. Table from Thornton, 2016, a more detailed list and further descriptions can be found in Ferrari A., 2005	54
6.1	Experimental data for the facility for all configurations and positions used during the campaign	60

7.1	Comparison of the FLUKA simulation with the experimental results. A total of $2.40E+14$ POT were collected during the experimental measurement.	64
7.2	Absolute dose measured at R11 and comparison with FLUKA simulation. A total of $2.40E+14$ POT were collected during the experimental measurements. RadFET measurement in Pos. 3 was affected by a readout error, which did not allow to properly evaluate the dose in that position.	67
7.3	Absolute dose measured at R13 and comparison between the dosimeters. A total of $5.94E+14$ POT were collected during the experimental measurements. Due to the offset of the beam the comparison with the FLUKA data is not possible.	70
7.4	Absolute dose measured in R1 with the configuration Cu_OOOO and comparison with FLUKA simulation. A total of $2.32E+14$ POT were collected during the experimental measurements. Only RadFET, installed in RadMON systems, were used for this irradiation test.	72
7.5	Absolute dose measured in R1 with the configuration Cu_CIIC and comparison with FLUKA simulation. A total of $6.87E+14$ POT were collected during the experimental measurements. Only RadFET, installed in RadMON systems, were used for this irradiation test.	74
7.6	Composition and provider of the used RPL dosimeter at CHARM. After LS1 the Schott DOS 2-type ones were replaced with the Chiyoda Techno Glass Corporation FD-7 ones.	77
7.7	Results from the dose rate dependency campaign at the ^{60}Co facility. The uncertainty of the dose rate is given by the standard deviation of the calibration prior each measurement. The uncertainty for the accumulated dose of the FD-7 RPL are the 5 % assumed for the gamma field. The results of the FD-7 RPL are compared with the ones achieved by the calibration with the Ionization Chamber (IC).	78
7.8	Results from the build-up and fading effect measurements for the RPL dosimeters. The average dose is taken from 10 individual RPL measurements, the uncertainty of the accumulated dose is given by the 5% assured for the gamma field. The first read average dose is taken as a reference for the other measurements.	79
7.9	High Energy Hadron fluence measured in R11 and comparison with FLUKA simulation. A total of $2.40E+14$ POT were collected during the experimental measurements. The experimental results were collected with the RadMON system.	82
7.10	High Energy Hadron fluence measured in R13 and with FLUKA simulation. A total of $5.94E+14$ POT were collected during the experimental measurements. The experimental results were collected with the RadMON system.	85

7.11	High Energy Hadron fluence measured in R1 with no shielding and comparison with FLUKA simulation. A total of $2.32E+14$ POT were collected during the experimental measurements. The experimental results were collected with the RadMON system.	87
7.12	High Energy Hadron fluence measured in R1 with full shielding and comparison with FLUKA simulation. A total of $6.87E+14$ POT were collected during the experimental measurements. The experimental results were collected with the RadMON system.	90
7.13	1MeV neutron equivalent fluence measured in R11 and comparison with FLUKA simulation. A total of $2.40E+14$ POT were collected during the experimental measurements. The experimental results were collected with the RadMON system.	92
7.14	1MeV neutron equivalent fluence measured in R13 and comparison with FLUKA simulation. A total of $6.87E+14$ POT were collected during the experimental measurements. The experimental results were collected with the RadMON system.	94
7.15	1MeV neutron equivalent fluence measured in R1 with no shielding and comparison with FLUKA simulation. A total of $2.40E+14$ POT were collected during the experimental measurements. The experimental results were collected with the RadMON system.	96
7.16	1MeV neutron equivalent fluence measured in R1 with full shielding and comparison with FLUKA simulation. A total of $2.40E+14$ POT were collected during the experimental measurements. The experimental results were collected with the RadMON system.	98

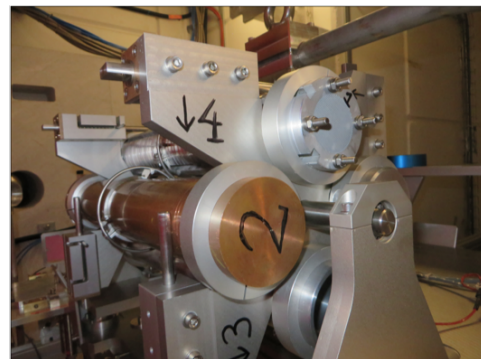
A.1 CHARM irradiation room



Fig. A.1.: Picture taken from inside the CHARM irradiation room. In the middle of the room, the shielding cage can be seen. The shielding layers are extracted in this pictures, but are still visible as yellow and orange slacks at the end of the cage. Additionally, the marble shielding, the rail for the Montrac test positions and the marked positions for the standard test positions, as dots on the floor, are visible.



(a) Montrac test position of CHARM, including the test cage.



(b) Target revolver of CHARM. The different target materials can be seen.

Fig. A.2.: More detailed pictures of the Montrac test position on the rail system inside CHARM. Devices under test are mounted on the cage, that is visible in the background. The first part is the connection wagon, where the cables and connections for the devices are mounted. Regarding the target revolver, four different settings are possible: copper, aluminium, aluminium with holes and air.



(a) Shielding cage and moveable shielding layers of CHARM. One iron layer is extracted right now.



(b) Rack setup at one of the standard test positions. The cables to connect electronic devices are visible as well.

Fig. A.3.: More detailed pictures of the shielding layers inside CHARM and the rack setup for one of the standard test positions.

A.2 CHARM radiation gradient assessment setup

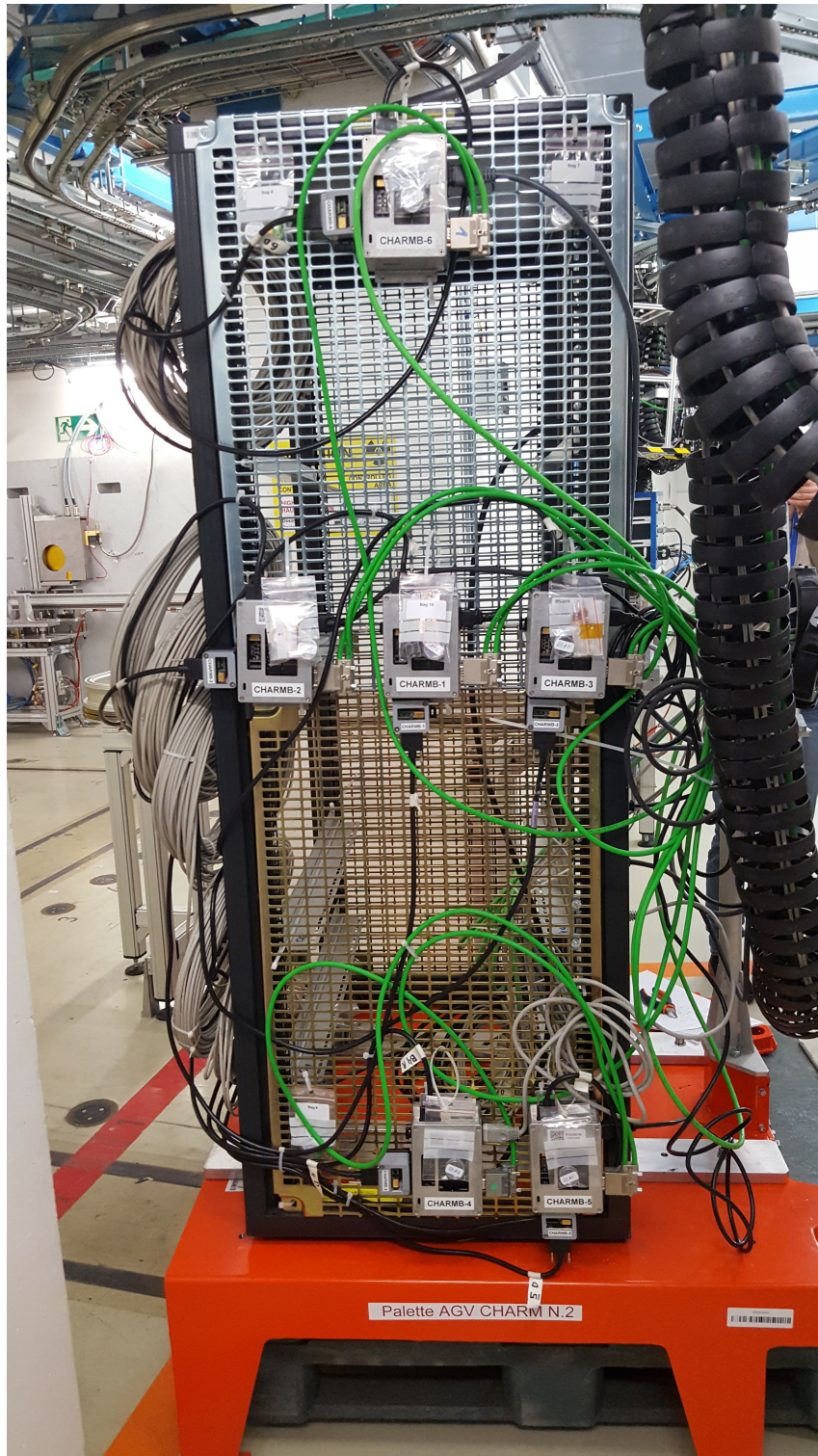


Fig. A.4.: Full setup for the rack position R11. The detectors on the rack can be seen.



(a) Center of the rack position R11



(b) Top of the rack position R11



(c) Bottom of the rack position R11

Fig. A.5.: Pictures of the actual test setup on the rack position R11. It can be seen that only one RadMON system was mounted on the top, but RPL and passive RadFET dosimeters were attached on the other positions. The center hosted three RadMON systems, and on the bottom two RadMON system were mounted. Additionally, the cables connecting the RadMON systems with the patch panel are visible as well.



Fig. A.6.: Test setup for the test position T0. It can be seen that the dosimeter (RPL and RadFET) are covering the whole table.

Colophon

This thesis was typeset with $\text{\LaTeX}2_{\epsilon}$. It uses the *Clean Thesis* style developed by Ricardo Langner. The design of the *Clean Thesis* style is inspired by user guide documents from Apple Inc.

Download the *Clean Thesis* style at <http://cleanthesis.der-ric.de/>.